

This is to certify that the

thesis entitled

PHOTOIONIZATION MASS SPECTROMETRY: IONIZATION AND FRAGMENTATION OF CH₃CN AND CD₃CN

presented by

David M. Rider

has been accepted towards fulfillment of the requirements for

Ph.D. degree in Chemistry

Date February 11, 1980

O-7639



OVERDUE FINES: 25¢ per day per item

RETURNING LIBRARY MATERIALS: Place in book return to remove charge from circulation records

PHOTOIONIZATION MASS SPECTROMETRY: IONIZATION AND FRAGMENTATION OF CH $_3$ CN AND CD $_3$ CN

Ву

David M. Rider

A DISSERTATION

submitted to

Michigan State University

in partial fulfillment of the requirements

for the degree of

DOCTOR OF PHILOSOPHY

Department of Chemistry

ABSTRACT

PHOTOIONIZATION MASS SPECTROMETRY: IONIZATION AND FRAGMENTATION OF CH₂CN and CD₂CN

Ву

David M. Rider

Photoionization mass spectrometry (PIMS) is a powerful technique for investigating ionization processes and fragmentation of molecular ions. Accurate ionization and fragment ion appearance potentials can often be determined and ion fragmentation pathways and mechanisms elucidated. In this dissertation a PIMS investigation of acetonitrile (CH₃CN) and acetonitrile-d₃(CD₃CN) is reported.

Photoionization of acetonitrile with 584\AA (21.2 eV) photons causes extensive fragmentation of the parent ion. The following ions are produced with sufficient intensity to be studied: CH_3CN^+ , CH_2CN^+ , HC_2N^+ , H_2CN^+ , CH_3^+ , and CH_2^+ . Photoionization efficiency (PIE) curves of these ions and their deuterated counterparts from the onset of ionization (~1016 Å, 12.2 eV) to 600 Å (20.7 eV) have been measured.

The parent ion PIE curves (CH₃CN⁺ and CD₃CN⁺) demonstrate that direct ionization and autoionization both contribute to the production of ions in the region studied. Autoionizing Rydberg series converging to the first and second excited electronic states of the parent ions are observed and assigned.

Jahn-Teller interactions in the ground state of the parent ion are indicated by the observation of the threshold for one quantum of excitation of the doubly-degenerate CCN bending mode (v_8). The measured ionization potentials are 12.194 \pm 0.005 eV for CH₃CN and 12.235 \pm 0.005 eV for CD₃CN.

Appearance potentials for the fragment ions listed above are determined, and where a more reliable heat of formation is not available in the literature, one is calculated. At their thresholds ${\rm CH_2CN}^+$ and ${\rm CD_2CN}^+$ are found to be produced exclusively from parent ion states which are populated by autoionization. The experimental appearance potentials and relative intensities of the remaining fragment ions indicate that H-atom migrations in the parent ion are important in the fragmentation mechanisms.



ACKNOWLEDGMENTS

Words are not sufficient to express my thanks and gratitude for help from the many individuals who made the completion of this dissertation possible. First and foremost I thank my wife, Sasha, for her loving care, devotion, and understanding throughout our stay at Michigan State University.

I thank Professor G. E. Leroi for his guidance, encouragement and patience as my advisor and for his perspective on the human aspects of research.

Dr. Edward Darland's contributions were unmeasurable. He was always willing to help solve instrumental problems and was a wonderful teacher and friend. I also want to acknowledge his help in generating several of the computer-drawn figures in this thesis.

Naomi Hack I thank for many stimulating discussions about nonscientific things, for her willingness to listen and her outlook which helped to keep problems in perspective.

Marty Rabb was a tremendous help in solving electronic problems. He was always willing to listen and provided many useful suggestions.

The support of Ron Haas, Scott Sanderson, Steve Veile and Dick Johnson of the electronic shop, and Russ Geyer, Len Eisele, Dick Menke and Deak Watters of the machine shop is gratefully acknowledged.

Rose Manlove I thank for the thankless job of typing the thesis.

Financial support from the Office of Naval Research, the National Science Foundation and the General Electric Co. are gratefully acknowledged.

TABLE OF CONTENTS

			Page	No
LIST OF	TAB	LES	vii	
LIST OF	FIG	ures	viii	
CHAPTER	I.	INTRODUCTION	. 1	
CHAPTER	II.	AN OVERVIEW OF PIMS	4	
A.	The	PIMS Experiment	6	
В.	Pho	toionization Processes	10	
	1.	Direct Ionization	10	
	2.	Autoionization	20	
c.	Fra	gmentation Processes	. 28	
	1.	Small Molecules	. 29	
	2.	Statistical Theory of Mass Spectra	31	
D.		plementary Experimental hniques	39	
	1.	Photoelectron Spectroscopy	40	
	2.	Electron Impact Energy Loss Spectroscopy	. 41	
CHAPTER	III.	EXPERIMENTAL APPARATUS AND PROCEDURES	. 44	
A.	Int	roduction	. 44	
В.	The	Instrument	. 44	
	1.	Light Source	. 44	
	2.	Monochromator	56	
	3.	Ionization Region	58	
	4.	Mass Spectrometer and	E 0	

											1	Page No
	5.	Ion and Photon Transducer	s.	•	•	•	•	•	•	•	•	. 59
	6.	Vacuum System	•	•	•		•	•	•	•	•	. 61
	7.	Data Collection	•	•	•	•	•	•	•	•	•	. 62
c.	Exp	erimental Details	•	•			•		•	•	•	• 59
	1.	Samples	•	•			•		•			• 63
CHAPTER	IV.	RESULTS AND DISCUSSION	•				•		•	•	•	• 66
A.	Pre	vious Studies	•				•					. 66
В.	The	Photoelectron Spectrum	•			•	•		•	•		. 66
c.		Photoionization Mass ctra of CH ₃ CN and CD ₃ CN	•	•	•	•	•	•	•	•	•	. 71
D.	Pare	ent Ion Curves	•	•	•	•	•	•	•	•	•	. 7 5
	1.	General Observations	•	•	•	•	•	•	•	•	•	. 75
	2.	Autoionization Structure: 1040 - 940 A	•	•	•		•	•			•	. 80
	3.	Autoionization: 900 - 800	A								•	. 92
	4.	The Threshold Region: 1000 - 1040 A	•	•	•	•	•	•	•	•	•	. 97
E .	Fra	gment Ion PIE Curves	•	•	•	•	•	•		•	•	.1 13
	1.	CH_2CN^+ , CD_2CN^+	•		•	•	•		•	•	•	.1 16
	2.	CHCN ⁺ , CDCN ⁺	•	•	•	•	•		•	•	•	.121
	3.	CH_2^+ , CD_2^+	•	•	•	•	•					.125
	4.	CH_3^+ , CD_3^+	•	•			•		•			.128
	5.	H_2CN^+, D_2CN^+	•	•			•		•		•	. 134
CHAPTER	v.	CONCLUSIONS AND SUGGESTIO FOR FURTHER WORK	NS •	•	•	•	•	•	•	•	•	.140
APPENDI	X A.	DIGITAL MASS SCANNER	•	•		•	•	•	•	•		.145
TTCM OF	DEET	PENCEC										162

LIST OF TABLES

		Page No.
II-1.	Photoionization Processes	11
IV-1.	Vibrational Modes and Frequencies of CH ₃ CN ⁺ and CD ₃ CN ⁺ Excited in the Pnotoelectron Spectra Compared to the Frequencies of the Neutral	69
IV-2.	CH ₃ CN and CD ₃ CN Photoionization Mass Spectra	73
IV-3.	Rydberg Series Converging to the First Excited State of CH ₃ CN ⁺ and CD ₃ CN ⁺	84
IV-4.	Rydberg Series Converging to the Second Excited State of CH ₃ CN ⁺	96
IV-5.	First Ionization Potentials of CH ₃ CN and CD ₃ CN	107
IV-6.	Heats of Formation of some Neutral Species and some Useful Conversion Factors	117
IV-7.	Calculation of ΔH_{fo} of CH_2CN^+ and CD_2CN^+	122
IV-8.	Summary of Appearance Potentials and Heats of Formation	139

LIST OF FIGURES

		F	age	No
II-1.	Block Diagram of a Photoionization Mass Spectrometer	•	•	7
II-2.	Effect of the Franck-Condon Factor on Direct Ionization Thresholds of Diatomic Molecules	•	•	15
11-3.	Krypton PIE Curve			27
111-1.	The MSU PIMS Instrument			
111-2.	Rare Gas Lamp High Power Switching Circuit	•	•	47
111-3.	Continuum and Hydrogen Pseudo-continuum	•	•	48
111-4.	Channeltron (CEM 4816) Wiring Diagrams for Positive and Negative Ions	•		60
IV-1.	Photoelectron Spectrum of CH ₃ CN	•		67
	21.2 eV Photoionization Mass Spectra of CH ₃ CN and CD ₃ CN			
IV-3.	CH ₃ CN ⁺ and CD ₃ CN ⁺ PIE Curves: 600 - 1040 Å	•	•	7 ó
IV-4.	Total PIE of CH ₃ CN	•	•	78
	CH ₃ CN ⁺ PIE Curve: 940 - 1040 Å			
IV-6.	CD ₃ CN ⁺ PIE Curve: 940 - 1040 Å	•		82
	Transition Energy Diagram for Excitation from the 5a ₁ Orbital			
IV-8.	CH ₃ CN ⁺ and CD ₃ CN ⁺ PIE Curves: 800 - 900 A	,		93
IV-9.	CH ₃ CN ⁺ and CD ₃ CN ⁺ PIE Curves: 1000 - 1040 Å	,		98
IV-10.	The Effects of a Triangular-Slit Function on a Step Function		• •1	01
IV-11.	Integration of a Gaussian Transition Probability		1	04

IV-12.	Fit of the CH ₃ CN ⁺ and CD ₃ CN ⁺ PIE Thresholds
IV-13.	CH ₂ CN ⁺ and CD ₂ CN ⁺ PIE Curves
IV-14.	CHCN ⁺ and CDCN ⁺ PIE Curves
IV-15.	CH ₂ ⁺ and CD ₂ ⁺ PIE Curves
IV-16.	CH ₃ ⁺ and CD ₃ ⁺ PIE Curves
IV-17.	H ₂ CN ⁺ and D ₂ CN ⁺ PIE Curves
A-1.	Block Diagram of Digital Mass Scanner
A-2.	Scanner Computer Interface
A-3.	Scanner Computer Interface
A-4.	Computer Interface Board Layout
A-5.	Main Logic Board Opto-Isolator Line Receivers
A-6.	Main Logic Board Time Base Circuit
A-7.	Main Logic Board Scan Time Multiplier
A-8.	Main Logic Board Twelve-Bit Counter and Multiplexer Circuit
A-9.	Thumb Wheel Circuits
A-10.	Manual Control Circuits and Counter Enable
A-11.	Main Logic Board Layout
Δ-12	Analog Circuit

CHAPTER I

INTRODUCTION

Although acetonitrile (CH₃CN) is a relatively small and simple molecule, the ionization and consequent fragmentation of CH₃CN has not been accurately and completely studied. The recent detection of acetonitrile in the comet Kohoutek¹ and in interstellar space in the region of the constellation

Sagitarius² has rekindled interest in its ion chemistry. Furthermore, acetonitrile has been found in discharge chambers simulating rare-earth conditions, suggesting that an investigation of its ion chemistry might be relevant to an understanding of abiogenic synthesis.^{3,4}

A wide range of molecular species has been discovered in interstellar clouds of gas and dust, and the question of how these molecular species are synthesized remains unanswered.

The temperatures of interstellar gas clouds are generally in the range 4-25° K, and occasionally as high as 100° K.

At these low temperatures most neutral-neutral reactions which could account for the observed molecules proceed at negligible rates due to kinetic reaction barriers. Reactions between ions and molecules often have very low activation barriers, and it has been suggested that many interstellar molecules are synthesized via ion-molecule reactions. Interstellar gas clouds are bathed in a flux of cosmic radiation which can account for the presence of ions in these environments; a quantitative model

ba mo th

> mo ti: fo

> > fu de

V.

fo ac ti

yi ic an

Vj as

tr ic de

Pā ir

tę

based on ionization by cosmic radiation and subsequent ionmolecule reactions has been proposed to account for many of
the observed molecules. Much of this model is based on the
thermochemistry of the species involved in possible ionmolecule reactions, and for the theory to be further tested
there is a need for thermochemical parameters such as heats of
formation, bond dissociation energies, electron and proton
affinities, etc., of the relevant neutrals and ions.

Photoionization mass spectrometry (PIMS) has become a viable experimental method in recent years. The most successful and important application of the technique has been to determine thermochemical parameters of ions. Indeed, PIMS is generally recognized as the best and most accurate technique for such investigations. With the above comments in mind, acetonitrile was selected as a good candidate for a PIMS investigation.

PIMS is primarily a spectroscopic technique in which the yield of ions from a sample gas is measured as a function of ion mass and photon energy. Thus, relative photoionization and fragmentation cross sections are measured, and they provide a wealth of information about the ions. Such quantities as ionization and appearance potentials, vibrational and electronic energy level spacings, and relative rates of various ionization and fragmentation processes can often be directly determined from PIMS experiments. From these, thermochemical parameters, fragmentation mechanisms and a variety of other information can be deduced. PIMS, coupled with a few other techniques, can often fully characterize molecular ionization

and fragmentation processes.

This thesis is a report of the photoionization mass spectrometry of acetonitrile. The objective was to learn as much as possible about the photoionization and fragmentation of this molecule, to derive thermochemical parameters where the data merit such a calculation, and to elucidate fragmentation pathways and mechanisms. The deuterated analog, CD₃CN, was included to help in the analysis of the data and to determine the isotopic dependence of various processes.

Chapter II of this thesis presents a general overview of PIMS. It includes a brief description of the PIMS experiment and contains a discussion of ionization and fragmentation processes which are important in PIMS. The experimental details of the acetonitrile experiments are presented in Chapter III. This chapter also includes a brief description of the MSU PIMS instrument along with a discussion of some of the instrumental problems encountered during the course of the investigation. The data are reported and discussed in Chapter IV, and Chapter V provides a summary with conclusions and suggestions for future experiments.

CHAPTER II

AN OVERVIEW OF PIMS

The experimental objective of PIMS is to measure the yield of ions produced by the absorption of photons by a neutral molecule, as a function of photon energy and ion mass. Although the name PIMS emphasizes mass spectrometry, the more important aspect of the experiment is the variation of the photon energy. The experiments described in this thesis are really vacuum ultraviolet absorption experiments in which the mass spectrometer serves as a very special detector. The mass spectrometer serves as a means for observing photon absorptions that lead to the ejection of an electron from a molecule as well as those absorptions in which sufficient energy is imparted to the ion to cause fragmentation.

A PIMS experiment, like other spectroscopic techniques, is directed toward measuring transition energies, and the results often allow one to infer properties of the initial and final states. Due to the nature of photoionization processes, PIMS often provides the most information about the ground states of the ions; however, features in the spectra often yield information about higher energy states, also. It is the purpose of this chapter to present an overview of PIMS. Section A is a brief description of the general experimental setup and is followed by a discussion of photoionization processes in Section B. Section C is a discussion of fragmentation of

polyatomic ions, and Section D is a very brief description of photoelectron spectroscopy and electron impact energy loss spectroscopy, two techniques which aid the interpretation of PIMS data.

First reports describing mass spectrometric analysis of ions produced by photoionization of gaseous samples were published in 1929¹⁰ and 1932.¹¹ However, early investigators were severely limited by the available vacuum and light source technology, and only fairly recently has PIMS become a viable experimental technique. In recent years it has been demonstrated to be useful for the study of unimolecular reaction kinetics of polyatomic ions, 12,13 the study of kinetics and thermodynamics of ion-molecule reactions, 13,14,15 and the determination of ionization potentials of atoms and molecules and of appearance potentials of fragment ions. 8,9

Even though a wide variety of applications have been found for PIMS, key references are somewhat scattered and incomplete. No comprehensive reviews of PIMS have been published since the one by Reid⁸ in 1971, which is now somewhat dated. Nevertheless, that review, together with references 9,12,14, 16-19, provide a useful introduction to the experimental methodology of PIMS, photoionization and fragmentation processes 9,12,18-22 and applications of the technique. 9,12,14 Since the introduction to PIMS presented here is intentionally brief and is intended to serve only as a framework for the discussion of the acetonitrile data, the reader is urged to consult these references for more detailed information.

A. The PIMS Experiment

A block diagram of a photoionization mass spectrometer is shown in Figure II-1. The apparatus consists of a photon source, photon monochromator, interaction region, ion optics and mass spectrometer, and photon and ion detectors. The output of the photon source is dispersed by the monochromator and the output of the monochromator is passed through the sample gas in the interaction region. The intensity of the transmitted photons is converted to an electrical signal by the photon detector. The ions are extracted at a right angle to the photon beam with an electrostatic potential and are focused onto the entrance of the mass spectrometer with electrostatic ion lenses. The mass spectrometer allows ions of only a single mass-to-charge ratio to impinge on the ion detector, where the ion arrival rate is converted into an electrical signal.

The experiment entails very simply the measurement of the intensity of an ion of selected mass as a function of the photon energy. Since the intensity of the available light sources is not constant as a function of energy, the photon intensity must also be measured so that the ion intensity can be normalized. It would be most desirable to measure the absolute photoionization cross section, but this quantity is difficult to determine because then the absolute photon intensity and the number density of neutral molecules in the photon beam must be known. Instead, a relative quantity, the

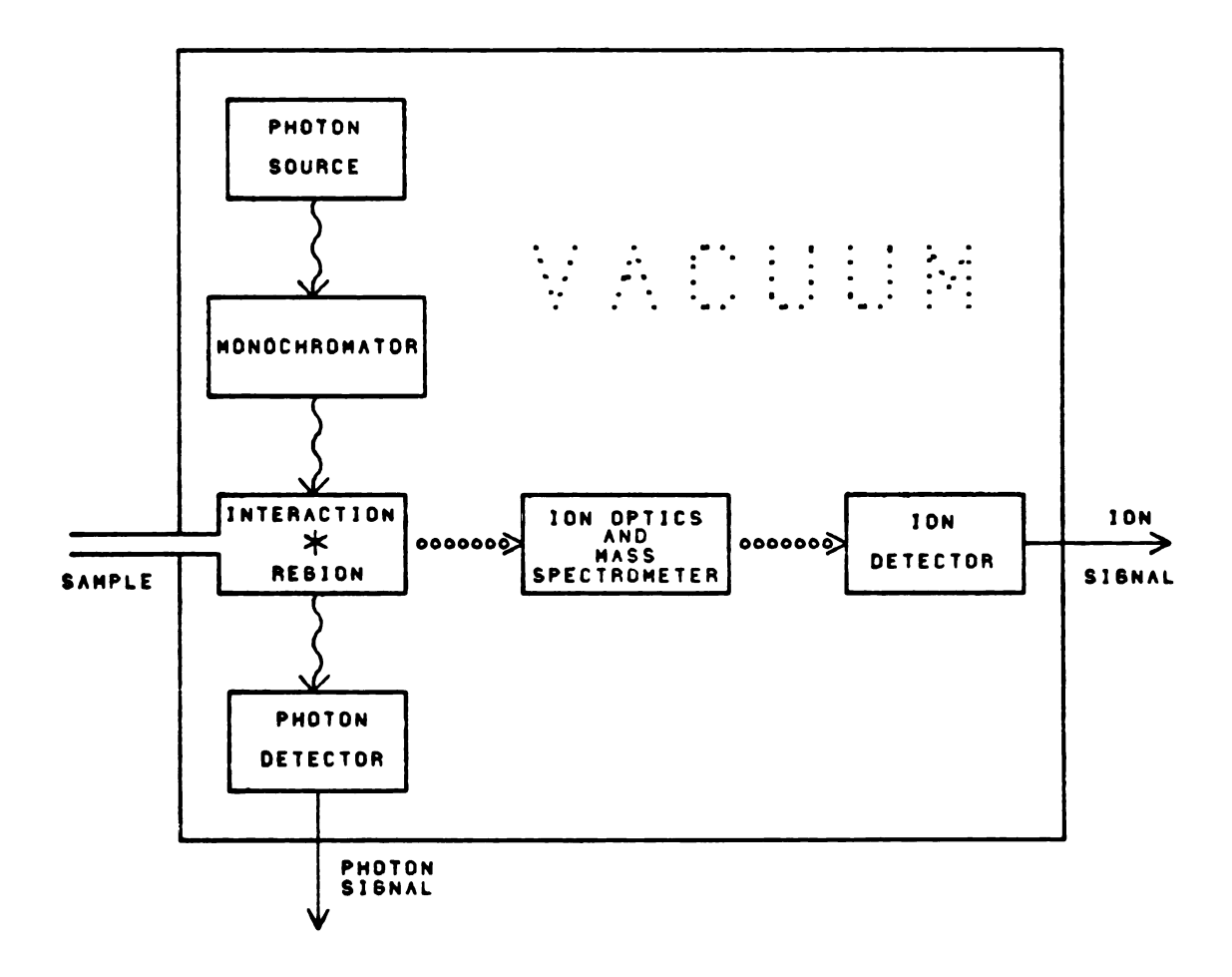


Figure II-1. Block Diagram of a Photoionization Mass Spectrometer.

photoionization efficiency (PIE), defined as:

$$PIE(E) = \frac{ion intensity (E)}{transmitted photon intensity(E)},$$
 (II-1)

is calculated. Although properly the incident photon intensity should be used to calculate the PIE, under typical operating conditions (low sample pressure) the amount of light absorbed by the sample is sufficiently small that the PIE calculated from the above relationship is directly proportional to the partial photoionization cross section of the ion being observed. The plot of the PIE of an ion as a function of photon wavelength or energy is referred to as the PIE curve.

The study of photoionization processes is experimentally difficult due to limitations imposed by experimental technology and the nature of the fundamental photoionization processes. The most severe difficulties arise because of the region of the electromagnetic spectrum in which the transitions of interest lie. The lowest ionization potential of most atoms and molecules is greater than 8 eV., and therefore one is required to work in the vacuum ultraviolet region (VUV) (2000-300 Å). First of all, most substances, including oxygen and nitrogen, absorb strongly in this region and as a result the optical path must be maintained at pressures less than 10^{-5} torr. This in itself is not a severe restriction, but it is complicated by the absence of suitable optical window materials in the VUV. Below the short wavelength cutoff of lithium fluoride (-1050 Å, or 11.8 eV) there are no known

window materials which can be used to isolate the lamp or sample gas from the rest of the instrument. Since most VUV light sources are electrical discharges in a gas, the lack of a suitable window material requires the light sources to be "isolated" from the rest of the apparatus via high speed pumping.

The fact that most substances absorb strongly in the VUV also means that reflectivities are low. The best available optical substrates have reflectivities on the order of 15-30% at 1000 Å, so that every reflection employed to disperse or focus the light throws away a large fraction of the incident light. This problem is further complicated by the lack of intense light sources. The best available light sources in the VUV region have peak intensities of only about 10^8-10^{10} photon \sec^{-1} Å⁻¹. Thus it is imperative that reflecting surfaces be kept to a minimum; normally a single diffraction grating is the sole optical element employed.

Another serious problem stems from the necessity to use low sample pressures in order to avoid scattering of the ions and reactive collisions of the ions with the sample gas; these processes decrease the intensity of the ions and introduce artifacts into the data. Most experiments must be performed with sample pressures of less than 10^{-3} torr.

Low sample pressures coupled with low intensity light sources and the low reflectivity of optical elements result in low ion count rates. In favorable circumstances, ion count rates may be several thousand per second, but they are often

as low as only a few ions per second. Fortunately, the utilization of ion counting techniques and digital computers allows sufficiently long integration times that useable data can often be obtained with such weak signals, but only at the cost of very long experiments. Data runs for a single ion may last as long as several days!

B. Photoionization Processes

When molecules are irradiated with high-energy photons, processes such as photoexcitation, photoionization or some combination of the two may occur simultaneously to produce a multitude of final states. In the following pages of this section, those processes which result in an ion and are therefore important to PIMS are discussed. Section B.1 deals with direct ionization and Section B.2 with autoionization.

Sections B.3 and B.4 provide a discussion of fragmentation of molecular ions resulting from photoexcitation of neutral molecules. These processes are summarized in Table II-1.

1. Direct Ionization

Irradiation of molecules with visible and ultraviolet light may induce transitions of valence electrons to the lowest excited states of the molecule. As the energy of the radiation is increased, transitions to higher excited states of the molecule become energetically possible and eventually an energy is reached at which the excited valence electron is no longer bound by the potential of the nuclei. The final state is then described as the product of a quantized state

Table II-1. Photoionization Processes.

$AB + hv \rightarrow AB^{+} + e^{-}$	Direct ionization
$AB + h_{V} \rightarrow AB^{*} \rightarrow AB^{+} + e^{-}$	Autoionization
$AB + hv \rightarrow A^{+} + B + e^{-}$	Direct dissociation
$AB + h\nu \rightarrow AB^* \rightarrow A^+ + B + e^-$	
$AB + h \rightarrow AB^{+}e \rightarrow A^{+} + B + e^{-}$	Predissociation
	•

of an ion core and a continuum state of a free electron. As the radiation energy is further increased the molecules continue to absorb, leaving the ion in the same final state with the electron carrying away the excess energy as kinetic energy. The absorption is continuous. Further increasing the radiation energy may make transitions to excited states of the ion possible; the free electrons will be produced with a distribution of energies, where the distribution will reflect the difference in energy between that required to reach the final states of the ion and the radiation energy. Transitions to the various final states of an ion will occur simultaneously. This is direct ionization.

Direct ionization is exactly analogous to an ordinary oneelectron transition observed in the visible or ultraviolet region of the spectrum, except for the one important difference that the electron is excited into a continuum state instead of a bound state. The probability of direct photoionization is proportional to the square of the dipole transition moment integral:²²

$$\mathbf{M}^{2} = | \langle \psi_{f} | \hat{\mu} | \psi_{i} \rangle |^{2}$$
 (II-2)

where $\hat{\mu}$ is the dipole moment operator, $\psi_{\hat{i}}$ is the wave function of the initial state of the neutral molecule, and $\psi_{\hat{f}}$ is the wave function of the ion and the photoelectron. From the Born-Oppenheimer approximation and the assumption that the electronic parts of the wave functions change negligibly in the time it takes for a transition to occur, one finds 22,24

that

$$M^{2} = |\langle \psi_{fe} | \hat{\mu} | \psi_{ie} \rangle|^{2} |\langle \psi_{fv} | \psi_{iv} \rangle|^{2}. \qquad (II-3)$$

Here ψ_{fe} and ψ_{ie} are the electronic parts of the final and initial state wave functions respectively, and ψ_{fv} and ψ_{iv} are the vibrational wave functions of the ion and the neutral molecule. The wave function ψ_{fe} describes both the ion and the free electron and may be represented as a linear combination of two Slater determinants -- one for the ion and the other for the free electron. Rotational motion is tacitly neglected since the experimental conditions required in PIMS are generally insufficient to resolve rotational structure in direct ionization, and the integrals of equation (II-3) are to a good approximation independent of rotation. 22

Qualitatively it is found, both theoretically 26 and experimentally, 18 that the electronic part of (II-3), $|<\psi_{\rm fe}|\hat{\mu}|\psi_{\rm ie}>|^2$, rises sharply to a maximum at the ionization threshold and decreases to small values for excitation energies much greater than threshold. In the region accessible to PIMS (20 eV) the decrease is usually less than 50% of the maximum at threshold. Near the ionization threshold -- up to one or two eV above -- the photoionization cross section can usually be taken as a step-function which is constant above threshold. 27,28 However, as pointed out by Rosenstock, 9 there is no guarantee that the range of validity of this assumption is this large.

If one neglects the vibrational part of equation (II-3)

and considers a system in which several electronic states are available, the photoionization cross section or PIE curve would be a series of steps, each step corresponding to the threshold for an ionic state. All ionic states with a threshold energy less than a given photon energy will be populated at a rate proportional to the cross section at that photon energy. In the absence of competing indirect processes this step-like behavior is indeed observed for atoms (see reference 18 for examples).

The vibrational part of equation (II-3) is the well-known Franck-Condon factor. It is simply the overlap between the vibrational wave function of the neutral molecule (ψ_{vi}) and that of the ion (ψ_{vf}). The effect of the Franck-Condon factor on the photoionization cross section is to attenuate the electronic factor and to introduce additional step-like structure to the PIE curves. The threshold for an electronic state of a molecular ion becomes a series of steps, where each step represents a threshold for a different vibrational state. The height of each vibrational step above the previous step is proportional to the Franck-Condon factor for the corresponding transition.

The overall shapes of the electronic thresholds can be quite varied, depending on the differences in the bond lengths between the neutral and the ion. This is shown pictorially for a diatomic molecule in figure II-2. If the electron is removed from a non-bonding orbital the interatomic distance of the neutral and the ion will be nearly the same, and

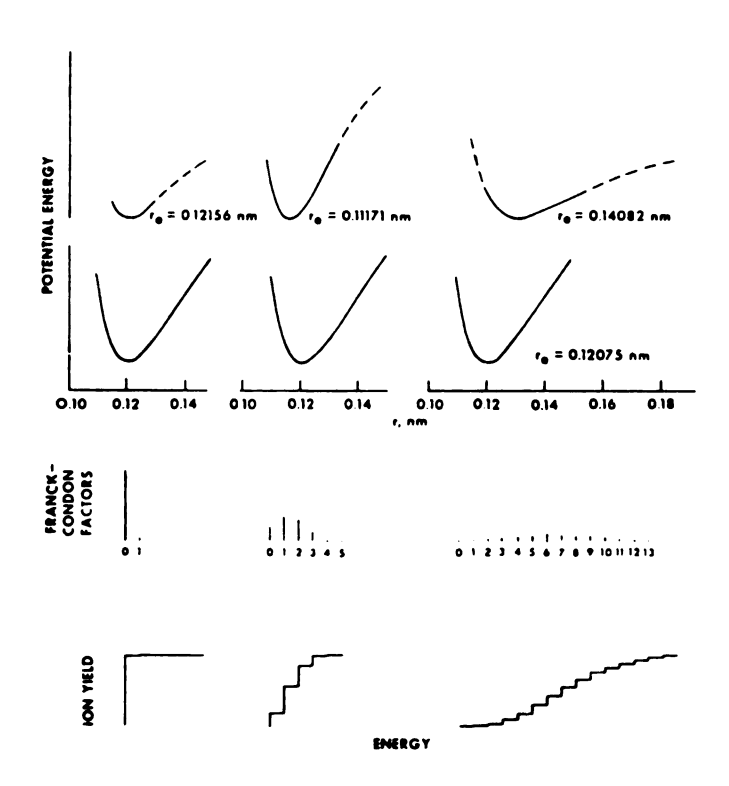


Figure II-2. Effect of the Franck-Condon Factor on Direct Ionization Thresholds of Diatomic Molecules (from Reference 9.)

essentially only the ion vibrational ground state will be accessible from the neutral ground state. The threshold for the electronic state of the ion would be only a single step. If the electron is removed from an orbital which is slightly bonding or antibonding, in which case the internuclear distance in the ion is a little greater or smaller than that of the neutral, additional ion vibrational levels become accessible and a vibrational progression will be observed, with an intense $(0 \leftarrow 0)$ transition and progressively less intense transitions to the higher vibrational levels. The threshold will resemble a staircase with a large first step and progressively shorter steps to higher energy. If the electron is removed from an orbital which is strongly bonding or antibonding the internuclear distance in the ion will be significantly greater or smaller than that of the neutral and the (0 + 0)transition may no longer be accessible. The threshold region will exhibit a long progression of vibrational steps. Franck-Condon factor has the same effect for polyatomic molecules except that many bond lengths may change and the thresholds may be overlapping progressions of steps if more than one vibrational mode of the ion is excited. The structure may be very complicated. In the absence of competing processes this step-like structure is often observed in the threshold region of parent ion PIE curves. The PIE curves for NO, 29 HCCH, 30 and NH₃ are good examples.

Resolved vibrational steps provide useful information about the vibrational structure of the ion, and about the

orbital of the neutral molecule from which the electron is removed. The energy spacings of vibrational steps are a direct measure of the vibrational spacing of the excited vibrational modes of the ion, and from them the excited modes can often be identified. From the assignment of the excited vibrational modes, the heights of the vibrational steps, and the overall shapes of the vibrational progressions, deductions can be made about the bonding characteristics of the orbital from which the electron is removed and the geometry of the ion.

Although individual rotational transitions within a vibronic photoionization transition are not resolved, they do affect the direct ionization cross section curve shape by producing some tailing at the onset of a vibronic step and rounding of the top of the step. This is a result of the spread of threshold energies of the individual rotational transitions. The exact shape of the steps depends on the thermal distribution of populated rotational states of the neutral, the differences in the moment of inertia of the neutral and the ion, and rotational selection rules. 9

The electronic selection rules for direct photoionization are very much simplified compared to those for absorption and emission between two bound states. The most important and most common direct photoionization transitions are one-electron processes, and they are restricted by the usual dipole selection rules. However, the final state of the system is an ion plus a free electron, and the free electron can carry away whatever angular momentum is needed to satisfy

the dipole selection rules. As a result all one-electron direct photoionization dipole transitions are allowed. 21,22

When spin-orbit interactions are small, the spin selection rule $\Delta S=0$ can also always be fulfilled. 21,22 The electron spin of the final state of the system is the sum of the spin of the ion and the spin of the free electron. The free electron can always leave the molecule with the spin it had in the neutral so that $\Delta S=0$. Most neutral molecule ground states are singlets, and since the spin of a free electron is $\pm \frac{1}{2}$, the most common ionic states are doublets. The most common direct photoionization transitions occur from singlet molecular ground states to doublet states of the positive ion. 22

The vibrational part of equation (II-3), the Franck-Condon factor, puts some restrictions on the allowed vibrational transitions within a direct photoionization transition. In order for the Franck-Condon factor to be non-zero, the inte- $(\psi_{f_{i}},\psi_{i})$ must be totally symmetric in the point group to which the molecule belongs. 21,22,24 The vibrationless ground state of a molecule is always totally symmetric and therefore only totally symmetric vibrational modes of the ion can be reached by direct photoionization. The ground vibrationless states of the ion are likewise totally symmetric and the (0 + 0) transition is always allowed. The vibrational wave functions of symmetric vibrational modes are totally symmetric regardless of the vibrational quantum number, so excitation of such modes is allowed with any number of quanta. Antisymmetric modes are antisymmetric for odd and symmetric for even vibrational quantum numbers, and such modes can be

excited in direct photoionization only in units of two quanta.

For polyatomic molecules belonging to point groups for which the normal modes are not just symmetric and antisymmetric, the vibrational selection rules must be determined by the direct product of the symmetry species of the initial and final vibrational levels. This product must contain the totally symmetric representation for the transition to be allowed. One still finds, when the neutral is in the ground vibrational level, that for all point groups the transition to the ground vibrational level of the ion is allowed. Also totally symmetric modes can be excited with any number of quanta and the single excitation of a single non-totally symmetric mode is never allowed. The allowedness of multiple excitations and combinations of non-totally symmetric modes must be determined by using the direct product.

Often one is most interested in measuring the energy of the transition from the ground vibrational state of the neutral to the ground vibrational state of the ion (the adiabatic ionization potential). Although this transition is always allowed by symmetry, there is no guarantee that it will be observed in direct ionization. For a transition to be observed not only must it be allowed by symmetry, but there must also be overlap between the vibrational wave functions of the initial and final states. Photoionization of $\mathrm{NO_2}^{32}$ is a good example of a case where, because of a large geometry change, the ground vibrational state of the lowest electronic state of the ion is not populated by direct ionization.

Autoionization

Autoionization, in contrast to direct ionization, is a two-step process. Molecules have bound, neutral states corresponding to excitation of electrons of lower energy (more tightly bound) than those in the highest occupied orbital.

Many of these excited states lie above the lowest ionization potential of a molecule, and if they are populated by absorption of radiation they may interact with the continuum states lying above the first ionization potential, leading to ejection of an electron. This is autoionization — the absorption of a photon to produce an intermediate, highly-excited discrete state of the neutral which ejects an electron to form an ion.

Since radiation is absorbed in a transition to a discrete state of the neutral, autoionization is a resonant process and ions will be produced only at the energy of the transition. Autoionization will often appear as a sharp, peak-like structure superimposed on the normally featureless direct ionization continuum. However, autoionization exhibits a great variety of asymmetrical line shapes and may appear as a "window resonance" in which there is a decrease or dip in the photoionization cross section, ^{18,33,34} (e.g. see the CO₂PIE. ⁴¹) The lifetimes of autoionizing levels can vary a great deal, ranging from ~10⁻¹⁴ seconds all the way to ~10⁻⁶ seconds; ⁹ for states with short lifetimes, the autoionization structure may be so broadened that it is indistinguishable from the continuum for direct ionization. Autoionization structure on a PIE curve may also be broadened by emission and/or by

predissociation into neutral fragments, in which case it may also be indistinguishable from the continuum.

Autoionization can occur from valence states lying above the lowest ionization potential of a molecule, but generally it originates from Rydberg states that are members of series converging to the second, third and higher ionization potentials of the molecule. The distinction between Rydberg states and valence states is not always clear, but in the molecular orbital framework, molecular Rydberg orbitals can be thought of as being formed from atomic orbitals with larger principal quantum numbers than those used to calculate the valence shell orbitals. 33 Being composed of atomic orbitals of high principal quantum numbers, Rydberg orbitals have a large spatial extent and in a somewhat naive but useful approximation Rydberg states can be considered as a one-electron system in which the electron in the Rydberg orbital is at so large a distance from the remaining ion core that the core appears as a point charge (H-like atom.) 33

The above picture is reinforced by the fact that nearly all transitions to Rydberg states (visible in PIMS experiments as autoionization structure) can be fit to a series described by the Rydberg equation:

$$E_{hv} = IP - \frac{R}{(n-\delta)}. \qquad (II-4)$$

Here \mathbf{E}_{hv} is the energy difference of the transition and IP is the ionization potential of the molecule to which the series converges as n, referred to as the principal quantum number,

runs serially to ∞ . R is the Rydberg constant (13.605 eV), and δ is called the quantum defect, which is essentially a fudge factor which accounts for penetration of the Rydberg orbital into the ion core.

Molecular Rydberg orbitals of the same n but different orbital angular momentum will, in general, not penetrate the ion core to the same extent and will be split into components of differing δ . The general rule for molecules composed of second row atoms is that ns orbitals are highly penetrating and require a δ of about 1, np orbitals are less penetrating and so have values of δ near 0.6, and nd orbitals are nearly nonpenetrating and have δ very close to zero. 33,35

The ion core of a molecule with an electron in a Rydberg state will never appear as a spherical charge distribution to the Rydberg electron, and this dissemmetry of the ion core may cause further splitting of degenerate Rydberg orbitals of a given orbital angular momentum. For example, an np Rydberg orbital for which the ion core has C_{2v} symmetry may be split into A_1 (p_2) , B_1 (p_x) , and B_2 (p_y) components due to a difference in the penetration of the Rydberg electron for different orientations of the Rydberg orbital with respect to the ion core. Such a splitting is indeed observed in the lowest 3p Rydberg state of H_2O . 36,37

For linear molecules, where the component of the orbital angular momentum directed along the molecular axis is quantized, Rydberg orbitals are conveniently labeled with the quantum numbers (nl λ) (e.g. 4p π). Although the meaning of λ

becomes ambiguous, the same terminology is often used for non-linear molecules which are linear when hydrogens are excluded (e.g. CH_3Cl). In this case λ refers to the orientation of the Rydberg orbital to the remaining molecular framework. In other molecules the Rydberg orbitals are labeled with n and the symmetry species of the orbital in the symmetry group of the molecule.

Fano, 38 and Fano and Cooper 34 have presented a theoretical treatment of autoionization in atoms which has been extended to molecules by Berry. 39 Their findings lead to several important conclusions. For atoms only Rydberg states lying above the ground state of the ion can autoionize and therefore be observed by PIMS. These Rydberg states will be members of series converging to excited states of the ion. It is found that the average absorption coefficient of these Rydberg series converges smoothly into the direct ionization continuum. That is, there will be no discontinuity on a PIE at the thresholds for excited states of atomic ions as there would be if direct ionization was the only process contributing to the photoionization cross section. 10,34 However, if the Rydberg series are well resolved, one can determine the convergence limit of a series by fitting the series members to the Rydberg formula (equation II-4) and solving for IP.

For molecules the situation is fundamentally the same:
the average absorption coefficient for Rydberg series converges smoothly into that of the continuum and no discontinuity

will be observed in the absorption cross section at the limit of a series. 10,39 However, in molecules there may be several possible channels for the release of the energy contained in the highly excited Rydberg state other than autoionization. Predissociation into neutrals is often energetically possible at photon energies above the lowest IP of a molecule, and if a sufficient number of Rydberg states decay by this channel not all absorptions will lead to autoionization and a discintinuity may well be observed in the PIE curve at the convergence limit of a series. The threshold for excited states of the ion may be directly observable. 10

An interesting and important conclusion from the work of Berry³⁹ is that there are several possible modes of auto-ionization from molecular Rydberg states. One mode, electronic autoionization, is possible only when the total electronic energy of a Rydberg state is greater than the lowest ionization potential of a molecule. In this case the electron in the Rydberg orbital was promoted from a ground state orbital lower in energy than the highest occupied ground state orbital. Autoionization occurs when the ion core of the Rydberg state relaxes to a lower energy configuration. The perturbation causing the relaxation and the subsequent ejection of the Rydberg electron is electron-electron repulsion.³⁹

A Rydberg state in which the molecule-ion core is vibrationally excited may eject the Rydberg electron by vibrational relaxation of the core. This is called vibrational autoionizations, being caused by a coupling of the oscillating

multipoles of the ion core with those of the Rydberg electron. The electronic energy of a Rydberg state undergoing vibrational autoionization does not necessarily have to be greater than the lowest IP of the molecule; it is only necessary that the sum of the vibrational and electronic energy be greater than the lowest IP. It is interesting to note that vibrational autoionization, which is believed to be the predominant mechanism in small molecules, ^{39,40} constitutes a breakdown of the Born-Oppenheimer approximation.

Autoionization may also be induced by the relaxation of a rotationally excited ion core. Rotational autoionization arises from the coupling of the rotational angular momentum of the ion core with the orbital angular momentum of the Rydberg electron. The role of rotational contributions to autoionization is not well understood due to the paucity of experimental data where rotational structures can be resolved.

All parent ion PIE curves contain contributions from both direct ionization and autoionization. In cases where Rydberg transitions are broadened by very fast autoionizing rates, predissociation into neutrals, or spontaneous emission of photons, autoionization may be indistinguishable from the direct ionization continuum. In fact, it has been recently proposed that direct ionization be theoretically treated as very fast autoionization. The PIE curves of diatomic molecules, where few channels for predissociation may be open, are often dominated by autoionization (e.g. $_{2}$, $_{2}$, $_{2}$, $_{3}$, $_{44}$).

However, for larger polyatomic molecules, where several channels for predissociation are often open and many changes in geometry are possible, PIE curves are often featureless, showing only hints of autoionization (e.g. dimethyl ether 45 and the halogenated methanes 19,46).

Many of the general ideas discussed in this section and the preceeding one are nicely demonstrated in the (essentially ideal) rare gas atom PIE curves. The PIE curve of krypton is shown in Figure II-3. The ground state of Kr + corresponds to the removal of a 4p electron from the neutral atom and is spin-orbit split into ${}^{2}P_{3/2}$ and ${}^{2}P_{1/2}$ levels. The threshold for the ${}^{2}P_{3/2}$ level at 885.6 Å (14.00 eV) is quite sharp, and above this threshold are two Rydberg series converging to the ²P_{1/2} level. Only the lowest two members of the two series are resolved in Figure II-3. The odd line shapes that are often exhibited in autoionization are demonstrated in the Kr + PIE curve by the first two peaks. The decrease in the PIE just above the $^{2}P_{3/2}$ threshold (884 Å) is actually part of the 6d line, as is the sigmoidal decrease of intensity (871-879 Å) on the high energy side of the 6d line. The two Rydberg series join smoothly onto the continuum of the ${}^{2}P_{1/2}$ level of the ion and the threshold for this level (845.4 Å, 14.67 eV) is several Angstroms beyond where the PIE appears to become continuous. (The threshold for the ${}^2P_{1/2}$ level is indicated with the arrow in Figure II-3.) The PIE is relatively constant beyond the series limit.

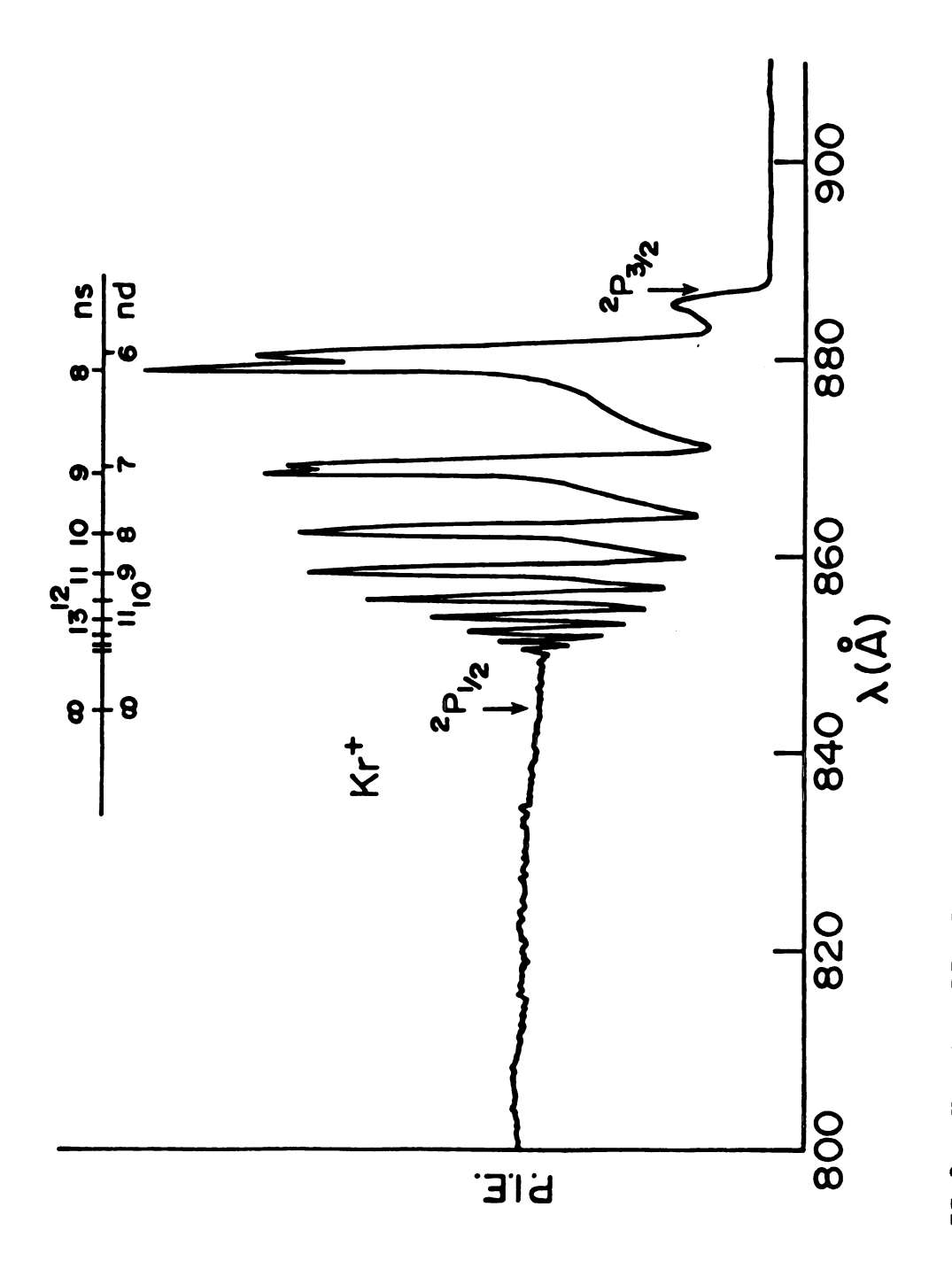


Figure II-3. Krypton PIE Curve.

C. Fragmentation Processes

Fragmentation processes can be very complex, and therefore they are often more difficult to analyze on a detailed level than direct ionization or autoionization. As an example, consider the four-atomic molecule, ABCD. When a parent ion is detected, the overall process: ABCD + hv + ABCD + e has occurred. The energy of the photon (hv) is precisely determined by the monochromator setting, and the internal energy of the parent ion is easily calculated by subtracting the electron's kinetic energy from the photon energy. Thus, the energetics and composition of the system are well characterized.

If the fragment ion A⁺ is detected, then

ABCD + $h\nu \rightarrow A^+$ + (BCD) + e^- . The ion mass and photon energy may be accurately measured and even the kinetic energy of the electron can be measured, but this is only part of the system. The neutral fragment or fragments are not detected with PIMS and their composition may be uncertain (they could be BCD, B+CD, BC+D or B+C+D). Moreover, the ion and the neutral fragments may also carry away kinetic and internal energy. The total system is thus not easily characterized compositionally or energetically. The appearance potential of the fragment ion, the lowest photon energy at which the particular ion is detected, may well correspond to the production of neutral and ionic species having significant internal and kinetic energy, which are not simply related to the known energies of the incident photon and ejected electron.

Fortunately, thermochemical information is often helpful in reducing the complexity of the process; on this basis many fragmentation pathways can be eliminated, and kinetic energy releases can be estimated. However, accurate estimates require accurate thermochemical data, which may not be available for all species of the system.

Small molecules (diatomic or triatomic)

For small molecules it is often useful to consider fragmentation as the result of processes which are directly analogous to direct ionization and autoionization, where a neutral molecule undergoes a transition (directly or indirectly) to a repulsive potential energy surface or a repulsive region of a bound potential energy surface of an ion.

Direct dissociation results from a direct transition to a respulsive surface and follows the same principles as direct ionization. The probability of the transition is determined primarily by Franck-Condon overlap of the initial neutral state and the continuous states of the unbound ionic surface. Direct dissociation is very fast (on the order of a vibrational period) and most of the excess energy will be carried away as translational kinetic energy of the products. The products may, however, be formed in excited electronic states if the dissociative surface does not correlate with the ground state of the ion.

Predissociation, sometimes referred to as preionization or autoionization when ion fragments are formed, implies an intermediate undissociated excited state. Two possibilities

arise:

- Case (1). The intermediate state is an excited state of the neutral that undergoes a further transition to a repulsive surface of the molecular ion.

 This is directly analogous to autoionization as discussed in the previous section.
- Case (2) The intermediate state is an undissociated ionic state which undergoes a radiationless transition to a repulsive ionic surface or redistributes vibrational or rotational energy such that energy in excess of a dissociation limit ends up in a particular vibrational mode or rotational degree of freedom. The bound ionic state may be populated by direct ionization or autoionization.

Although these two modes of predissociation are conceptually distinct, it is often not possible to separate them experimentally. While peak-like structures in a parent ion PIE curve is a sure indication of autoionization, the same structure in a fragment ion PIE curve only means that a discrete state of the neutral was populated on the pathway to the ion fragment. The dissociation may have occurred by Case (1) or Case (2) predissociation.

Whether predissociation occurs by Case (1) or Case (2), the fragments may fly apart with a considerable amount of vibrational or rotational energy since the intermediate state may be produced with internal excitation. 12,14,24

discussion that follows is adapted from Forst.

In RRKM theory dissociation is treated as a vibrational That is, dissociation will occur when sufficient energy is available in a vibrational mode such that a bond is extended beyond some critical value, leading to rupture. The probability of dissociation is then the probability that at least some critical amount of energy, the energy just needed to rupture a particular bond, is found in that bond. The primary assumption of RRKM theory is that this probability is purely statistical. It depends only on there being sufficient vibrational energy available among all the normal modes of the excited molecule, and the ratio of the number of ways that the vibrational energy of a molecule can be distributed to put at least the critical energy into the dissociating bond to the total number of ways that the vibrational energy can be distributed within the molecule. For the dissociation to behave statistically, vibrational energy must flow freely and randomly throughout the molecule.

RRKM theory considers energy randomization on only a single potential energy surface. STMS makes a second important assumption. STMS assumes also that electronic energy is freely and randomly converted into internal energy of just one low-lying state, usually the ground state of the ion (although it need not be the ground state). The theoretical and experimental evidence for and against randomization of electronic energy is fully discussed by Forst 48 and need not be repeated here; it is concluded that in the great majority of cases the

assumption appears valid. In any case, the utility of STMS lies in its ability to predict the general features of fragmentation of polyatomic molecular ions.

STMS implies that only Case (2), described above, predissociation, will be important. A dissociation is considered to be a unimolecular reaction of a parent ion which is formed with sufficient energy to enable the rupture of a bond. Furthermore, time is required for the energy to flow into the rupturable bond or bonds. Thus, STMS emphasizes the temporal aspects of PIMS. The interaction region (the ion source) of a photoionization mass spectrometer (or any mass spectrometer) is located a fixed distance from the mass analyzer. Any parent ion that fragments in the time it takes to travel from the interaction region to the mass spectrometer will be detected as a fragment ion. The intensity of a fragment ion will depend on the number of parent ions formed with energy above the critical energy, the rate constant for the fragmentation channel, and the flight time from the interaction region to the mass analyzer. Some types of mass analyzers, e.g., magnetic sector and time-of-flight instruments, may allow one to observe fragmentations that occur in the analyzer.

The rate constant (k(E)) for one channel of fragmentation is given by: 12,48

$$k (E) = 0 E < E_{O},$$
 (II-5)

$$k(E) = \frac{\alpha G^*(E-E_O)}{hN(E)}$$
 for $E \ge E_O$,

where k(E) is the rate constant at a total excitation energy E (with respect to the ground state of the ion), N(E) is the density of states at energy E, and $G^*(E-E_O)$ is the density of states of the activated complex (i.e., essentially the parent ion minus the fragmenting bond) integrated from the critical energy, E_O , to the excitation energy E. The constant α is of the order of magnitude unity and takes into account degenerate fragmentation channels due to the symmetry properties of the dissociation, and h is Planck's constant. Note that N(E) is essentially the number of ways that energy E can be distributed in the molecular ion and $G^*(E-E_O)$ is the sum of all the ways that energy E can be distributed so as to leave at least energy E_O in the dissociating bond.

Potential energy surfaces for dissociating ions rarely have a reverse energy of activation. That is, a fragmenting molecular ion usually does not pass over a hump in a potential energy surface, but only over a ledge. This means that, in general, fragments produced at the critical energy will be formed with no internal or translational kinetic energy. If a fragment ion is produced at a detectable rate at the critical energy (E_0) , then the appearance potential (AP) of the fragment (the minimum photon energy at which the fragment is detected, assuming the neutral is in its ground electronic, vibrational and rotational state) will be at a photon energy equal to the ionization potential of the neutral plus the thermochemical threshold for the dissociation. Under these

conditions an accurate heat of formation can be calculated for the fragment ion. For example, if $AB + h\nu \rightarrow A^+ + B + e^-$ and $AP = \Delta Hrxn$, then $\Delta H_f(A^+) = AP(A^+) + \Delta H_f(AB) - \Delta H_f(B)$.

Under what conditions will it be possible for the experimental AP of a fragment ion to correspond to the thermochemical threshold? There are several points to note. First, in a PIMS experiment the PIE is measured at some fixed time after the ionization (usually 10^{-5} - 10^{-6} s.⁹). Second, the rate constant will have a non-zero value at the critical energy given approximately by: 12,51

$$k(E_O) \approx \frac{1}{hN(E_O)}$$
 (II-6)

Third, in general, it is found that k(E) is a monotonically, rapidly-increasing function of E above E_0 . 12,51

Assume for the moment that parent ions are formed with a suitable distribution of energy greater than the critical energy for a dissociation such that the dissociation is not limited by this factor. Three cases can be distinguished.

Case (1). $k(E_O)$ is sufficiently large that all or nearly all parent ions formed with excitation energy $E \ge E_O$ will be dissociated within the flight time to the mass analyzer. The rate at which the fragment ions arrive at the mass analyzer is then the rate at which the parent ions are produced with internal energy greater than E_O . The dissociation rate constant will have no effect on the shape of the fragment ion PIE. In this case an accurate heat of formation of

the fragment ion can be determined from the AP.

- Case (2): k(E_O) is not large enough for a detectable number of fragment ions to be formed during the flight time. Only at energies above Eo would the fragment ion be detected, and the PIE would depend on k(E) and the rate at which the parent ions are formed with internal energy greater than E_{O} . In general as the photon energy (E_p) is reduced from $E_p > E_0$ toward E_0 the fragment ion PIE asymptotically approaches The apparent AP would lie at an energy greater than the critical energy and would serve as only an upper limit to the thermochemical threshold. The shift of the experimental AP above the critical energy due to a low fragmentation rate constant is often referred to as the kinetic shift.
- Case (3): $k(E_0)$ is sufficiently large for a detectable number of fragment ions to be produced at E_0 , but this process competes with one or more other fragmentation channels for which E_0 is lower. Since fragmentation rate constants increase rapidly with energy, the rates for channels of lower critical energy may well be sufficiently fast at the critical energy of a higher energy channel that all parent ions dissociate by one of the lower energy pathways

and no parent ions survive sufficiently long to dissociate by the newly-available pathway. As E_p is increased above E_0 for this higher energy pathway the rate constant will increase such that it can compete with those for lower energy channels, and the fragment will be detected. The fragment ion PIE curve will be similar in shape to those of ions falling in Case (2) and the AP will yield only an upper limit for the thermochemical threshold. The shift from the thermochemical threshold of the measured AP due to competition with other fragmentation pathways is frequently referred to as the competitive shift.

The quantity N(E) in equations II-5 and II-6 is a rapidly 48 increasing function of E and therefore k(E_O) (equation II-6) will be smaller the higher the critical energy and the more likely it is that the corresponding fragmentation channel will fall into Case (2). The function $G^*(E-E_O)$ is also a rapidly increasing function of E ($G^*(E-E_O)$) increases more rapidly than N(E) 48), and at a given energy a fragmentation channel with a higher critical energy will in general have a smaller rate constant than a dissociation with a lower critical energy. This results because N(E) will be the same for both channels whereas $G^*(E-E_O)$ will be smaller for the higher critical energy channel due to the smaller energy range for the integration which determines $G^*(E-E_O)$. The lowest energy fragmentation

process is the one most likely to yield an accurate fragment ion heat of formation. The APs of higher energy fragmentation pathways are almost always shifted above the thermochemical threshold due to kinetic and (more generally) competitive shifts; they are useful only for determining upper limits for the heat of formation of the fragment ions involved. 12

To this point in the discussion, little has been said about the rate at which the parent ions are produced. rate at which a fragment is detected can never exceed the rate at which parent ions are produced with internal energy above the critical energy for the fragmentation process. (The rate at which a fragment is detected, however, may be greater than the rate at which the parent ion is detected if the fragmentation is fast and more parent ions are produced with internal energies above the relevant critical energy than below it.) All fragment ion intensities are eventually limited by this rate. Insufficient production of parent ions with internal energy equal to the critical energy for a fragmentation channel could, like the kinetic effects, delay the detection of a fragment ion until well above its thermochemical threshold. Often this possibility can be eliminated from consideration since many fragment APs are observed in regions where states of the parent ion are known to be populated by direct ionization and autoionization. However, when a fragment ion AP coincides with the threshold of an upper state of the parent ion this source of error should be considered.

Methane and ethane are good examples of smaller polyatomic

molecules that fragment as predicted by STMS. The PIE curves of methane and its fragment ions can be found in Reference and those of ethane in Reference 53. In order to make a comparison between the theoretical predictions of STMS and the results of a PIMS experiment one would need to calculate the rate constants for each fragmentation channel and to know the distribution of internal energies in which the parent ions are formed at a given photon energy. The calculation of the rate constants is fairly straightforward and can be accomplished with modest computational effort. 12,48 The more severe problem is the need to know the distribution of internal energies with which the parent ions are formed. If direct ionization is the predominate process and if the direct ionization cross section approximates a step function, then an estimation of this distribution can be made by taking the first derivative with respect to photon energy of the total (parent plus fragments) PIE. 50 This approach was used by Chupka on $methane^{52}$ and $ethane,^{53}$ and the results showed reasonable agreement with theory. Most of the differences could be attributed to contributions to the PIE by autoionization. agreement between theory and experiment was later confirmed by Stockbauer 54 in a threshold electron-photoion coincidence experiment, where only fragments produced from parent ions of known internal energy are detected.

D. Complementary Experimental Techniques

Since the results of a PIMS experiment depend on the properties of the electronic and vibrational states of ions

and the properties of neutral states above the lowest ionization potential of a molecule, other techniques which provide information about these states often prove useful and complementary. Results from two of these techniques, photoelectron spectroscopy (PES) and electron impact energy loss spectroscopy (EIELS), have been invaluable for interpreting the acetonitrile PIMS data and will be referenced often in the discussion of acetonitrile in Chapter IV. A brief description of these two techniques follows.

1. Photoelectron Spectroscopy

PES, like PIMS, utilizes ionization by photons to investigate ions. In PES the kinetic energy of the ejected photoelectron is measured, but there is no attempt to observe the ions directly. A gaseous sample is irradiated with fixedenergy, monochromatic VUV light; most often, 21.21 eV photons produced from an electric discharge in helium are utilized, but other rare gas resonance lines have been employed. kinetic energies of the photoelectrons are measured with an electron spectrometer and a plot is made of the intensity of the electrons as a function of the difference in energy between the monochromatic photons and the photoelectrons. Since energy and momentum are conserved, this difference is the excitation energy of the product ion with respect to the neutral molecule. The photoelectron spectrum displays the distribution of ionic states that are populated upon ionization.

Photoelectron spectra are usually obtained at a photon

energy where autoionization does not significantly contribute to the photoionization cross section, and since direct ionization cross sections vary little with energy above threshold, PES is useful for judging the contribution of direct ionization to a PIE curve. Indeed, if autoionization did not contribute to the total PIE, the first derivative with respect to photon energy of the total PIE would closely approximate the photoelectron spectrum.

The vibrational frequencies of an ion, as well as relative Franck-Condon factors for the transitions, may often be determined directly from the vibrational structure in a photoelectron spectrum. These in turn are useful for determining changes in geometry between the neutral molecule and the ion. On the other hand, the photoelectron spectrum reveals little or no information about fragmentation of ions. Sometimes fragmentation may be inferred from broadening of or the absence of vibrational structure in a photoelectron spectrum; however this type of evidence is uncertain. Photoelectron spectroscopists most often rely on PIMS for direct evidence of fragmentation. More details of PES are given in References 21, 22, and 55.

2. Electron Impact Energy Loss Spectroscopy

Ordinary optical absorption spectra in the energy range of the ionization continuum are often useful for locating Rydberg states which might autoionize. However, because of the experimental difficulties of working in the VUV, very limited data are available. EIEL spectra provide much the same

information without many of the experimental constraints of VUV absorption spectroscopy.

EIELS is an inelastic electron scattering technique in which a gaseous sample is irradiated with a beam of monoenergetic and fixed-energy electrons, and the kinetic energies of the scattered electrons are measured with an electron spectrometer. In a fashion similar to that used for PES, the electron intensity of the scattered electrons is plotted as a function of the initial electron energy minus the scattered electron energy. The incident monoenergetic electrons induce transitions in the neutral sample molecules and will leave the scattering complex with an energy equal to the incident energy minus the transition energy. The EIEL spectrum will display peaks at the electron energy differences corresponding to the induced transitions.

which may autoionize and thus be observed in a PIE curve, however, they may display more transitions to Rydberg states than can be observed in an optical experiment, due to the relaxed selection rules of electron-induced transitions. The advantage over PIMS for observing transitions to Rydberg states is that transitions to states below the lowest IP of a molecule can be observed. These transitions are often helpful for assigning autoionization structure in a PIE curve for which a limited number of Rydberg series members are observed through autoionization and for which lower members of the series are located below the IP. EIEL spectra, however,

provide little information about ionic states since the Rydberg series join smoothly onto the ionization continuum. More details of EIELS can be found in References 20, 56 and 57.

CHAPTER III

EXPERIMENTAL APPARATUS AND PROCEDURES

A. Introduction

The purpose of this chapter is threefold: to present a brief description of the MSU PIMS instrument, to document the experimental conditions under which the data presented in Chapter IV were recorded, and to discuss experimental problems which were encountered in the course of this work. The instrument has been described in considerable detail elsewhere, 19,58 and the brief overview is included here for completeness and to facilitate the discussion in this chapter. A diagram of the apparatus is shown in Figure III-1. The instrumental problems encountered during the course of this investigation were innumerable, many of them due to lack of experience with the instrument, whose construction was completed just prior to the start of the acetonitrile experiments. Many of these problems have been resolved; however, some are likely to occur again, and it is hoped that the following discussion will be of help to future users of the instrument.

B. The Instrument

1. Light Source

The light source is a Hinterregger-type windowless discharge lamp with water-cooled anode and cathode. The discharge tube is a 25 cm long \times 4 mm I.D. water-jacketed quartz capillary to which the discharge gas is admitted at the anode

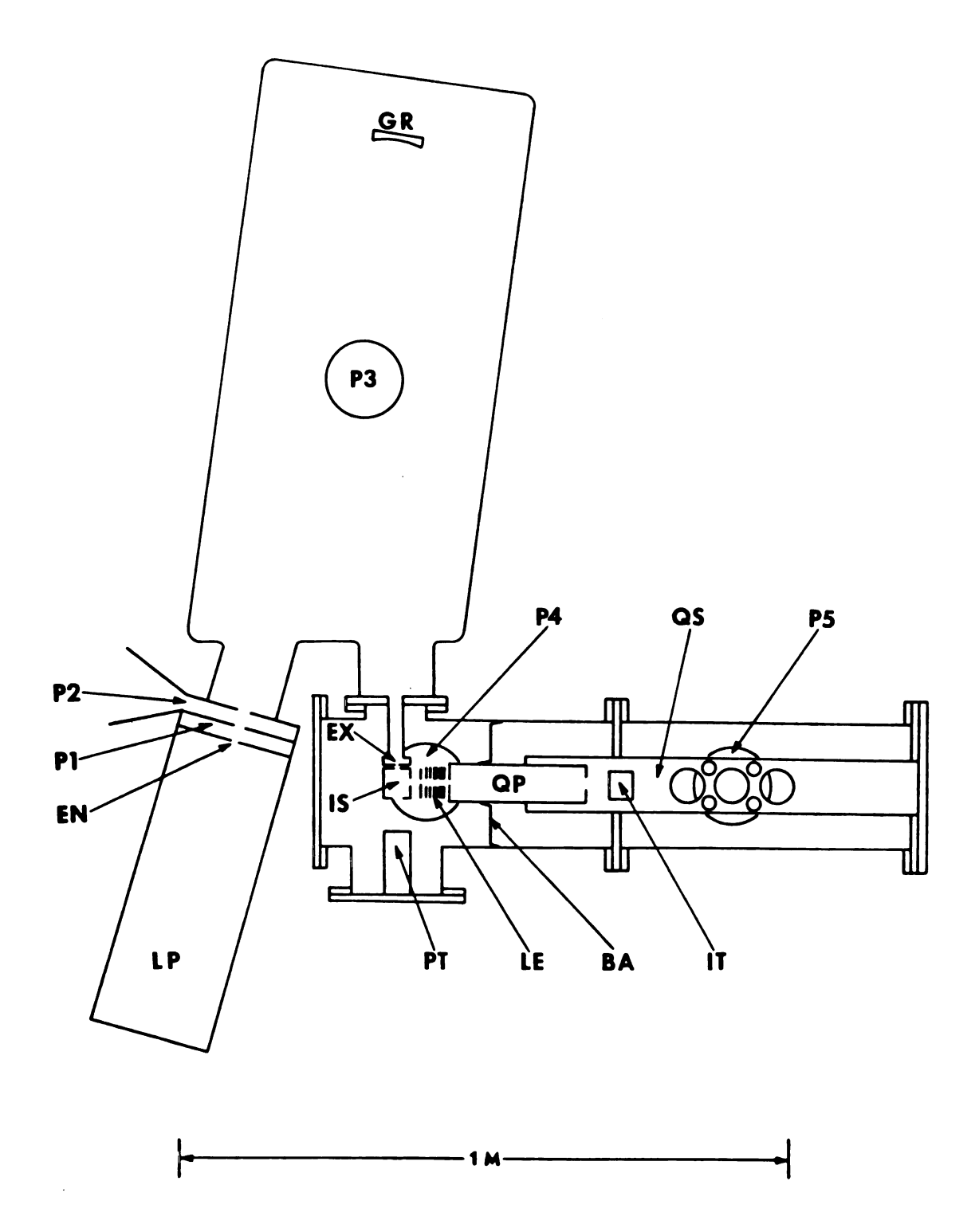


Figure III-1. BA-baffle; EN-entrance slit; EX-exit slit; GR-grating; IS-ion source; IT-ion transducer; LP-lamp; Pl-first differential pumping port; P2-second differential pumping port; P3-monochromator pumping port; P4-sample chamber pumping port; P5-quadrupole chamber pumping port; PT-photon transducer; QP-quadrupole; QS-quadrupole support; LE-Ion Lense.

after it has passed through a molecular sieve trap immersed in liquid nitrogen. A small differential pressure is maintained down the length of the discharge by pumping on the cathode end of the lamp; this stabilizes the discharge and helps eliminate sputtering of the cathode onto the monochromator entrance slits. The cathode vacuum pump is throttled with a needle valve.

The rare gas continua can be produced by a high-power pulsed discharge in the pure gas. The MSU instrument utilizes a home-built, single vacuum tube, high-power switching circuit to pulse the output of a high voltage d.c. power supply.

The switching circuit is in turn driven by a Cober A model 605P high-power pulse generator. A schematic diagram of the switching circuit is shown in Figure III-2.

The hydrogen many-line pseudo continuum is produced by a d.c. discharge in pure hydrogen at a pressure of 2-4 torr. The d.c. high voltage power supply used in the switching circuit, from which it is disconnected in this application, powers the hydrogen discharge. A 1500Ω , 1500 W resistor limits the current drawn from the supply.

The ionization potential of acetonitrile falls in a region of overlap between the helium Hopfield continuum, hereafter referred to as the helium continuum, and the hydrogen pseudo continuum; however, neither light source is very intense in the overlap region. The output of both lamps is shown in Figure III-3. Preliminary data were taken with both lamps and the helium continuum was found to be the better

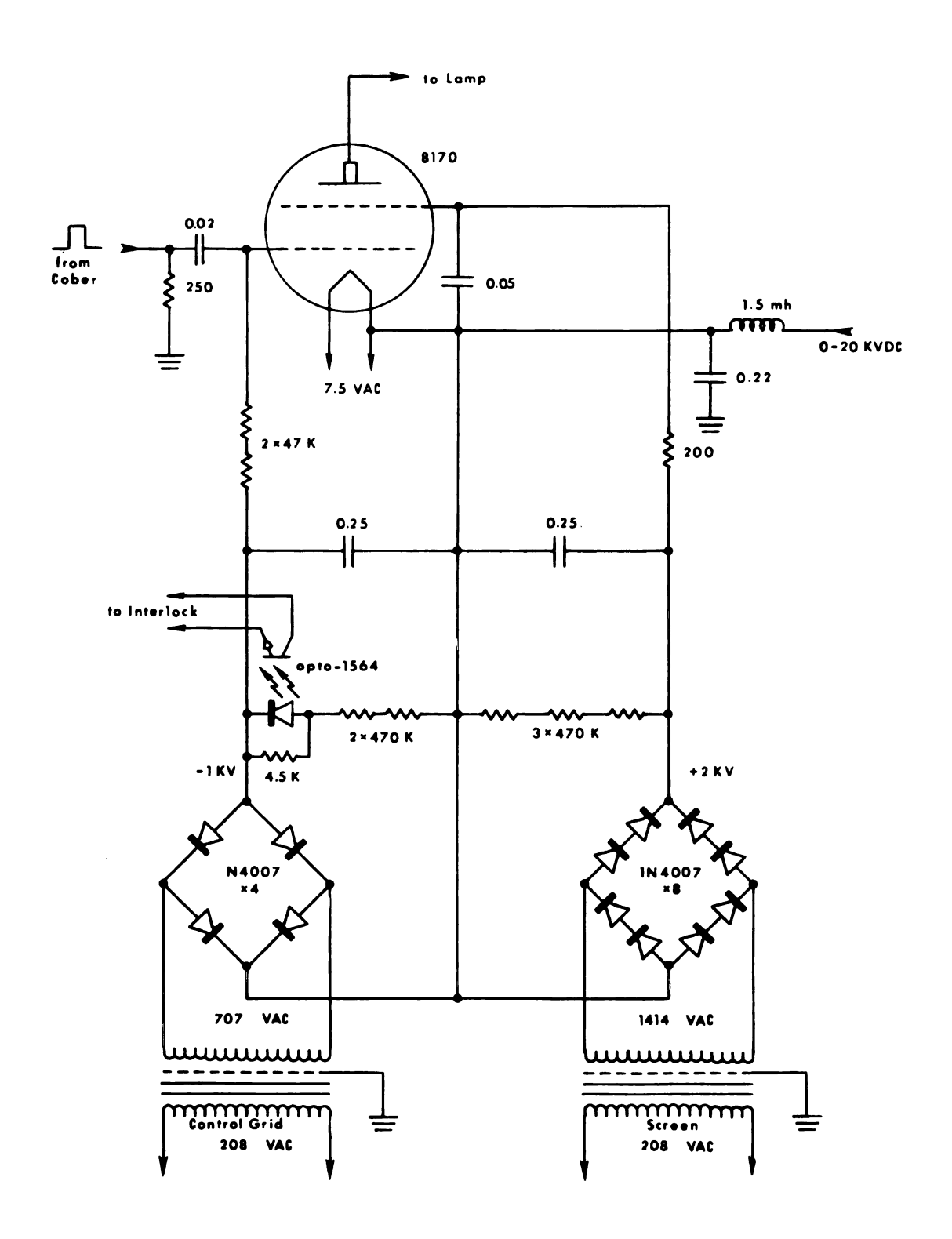
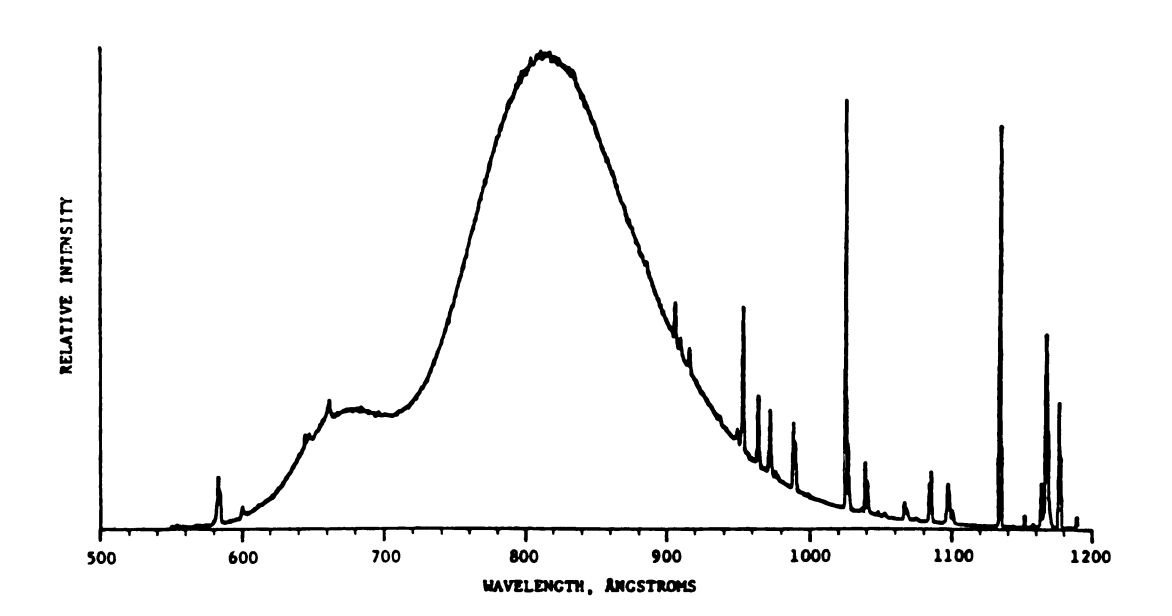


Figure III-2. Rare Gas Lamp High Power Switching Circuit.



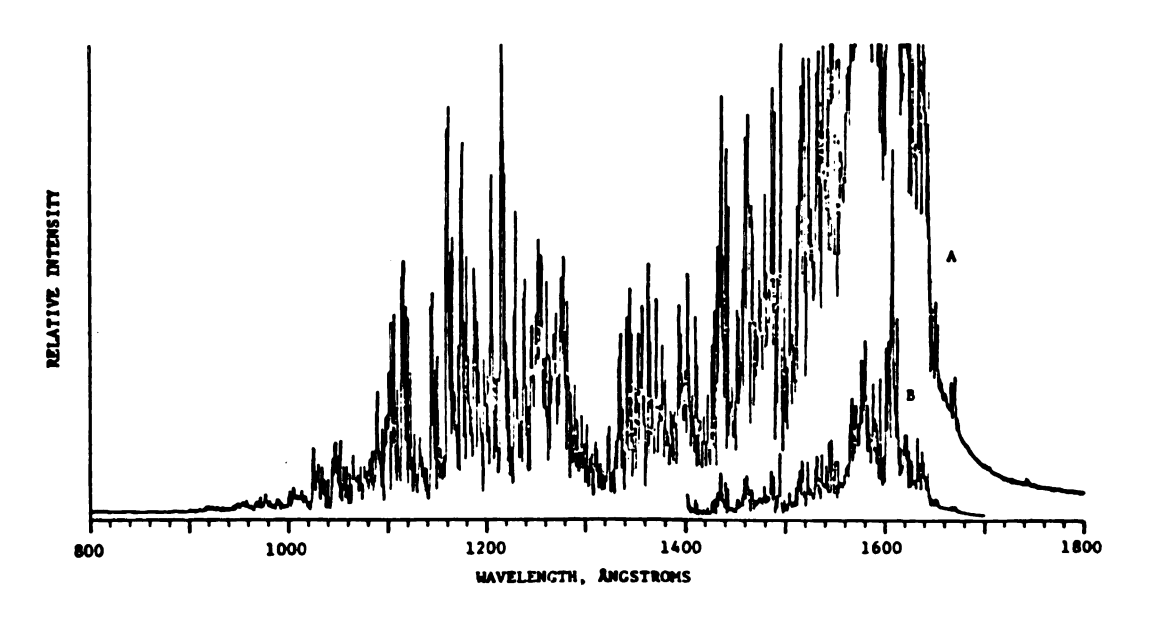


Figure III-3. Spectral Distribution of the Helium Continuum (top) and Hydrogen Pseudocontinuum (bottom) Lamps.

light source for the acetonitrile experiments; all PIEs presented in this thesis were taken with that source. The hydrogen continuum with its large variation in intensity as a function of wavelength made it impossible to tell if structure in the PIEs was real or an artifact caused by scattered light. The smooth intensity variation of the wavelength output from the helium source, plus the few sharp lines from impurities in the lamp gas, made it relatively easy to distinguish real structure from artifacts and to properly correct for scattered light. However, to minimize artifacts a great deal of effort went into reducing impurities to a minimum by always using a clean gas trap and a leak-free lamp gas plumbing system.

The intensity of the helium continuum is controlled by several variables: helium pressure and purity, pulse width and frequency, d.c. high voltage, Cober pulse generator peak output voltage, and the condition of the lamp electrodes.

The highest helium pressure possible, which is limited by the differential pumping between the lamp and monochromator and by the pumping speed of the monochromator pump, produces the highest intensity. Under current instrumental conditions the maximum pressure is about 70 torr with 100μ entrance slits, and about 130 torr with 50μ entrance slits.

The pulse frequency, pulse width and Cober high voltage

A discussion of such artifacts appears in Reference 21, p.319.

are adjustments made on the Cober pulse generator. The capabilities of the Cober and the limitations and requirements of the switching circuit constrain these parameters. The best set of parameters are a pulse width of $0.42\mu s$ a frequency of 33.3 kHz and a Cober high voltage setting of 1.3 kV d.c. A narrower pulse width would allow a higher frequency to be used and would increase the lamp intensity. However, the pulse width is limited to $0.42\mu s$ by the turn-on time of the switching circuit. The Cober's d.c. high voltage is set (1.3 kV) for a peak output voltage of 1 kV, which should not be exceeded since doing so may cause damage to the switching tube.

With the above setting on the Cober and 70 torr of helium, the maximum intensity is attained with the switched high voltage at 10 kV d.c. At this voltage a current of 90-100 mA are drawn from the supply when the lamp gas is pure and the lamp electrodes are clean. Increasing the voltage above 10 kV increases the current drawn from the supply, but has no effect on the lamp intensity.

A current from the high voltage power supply of less than 90 mA at 10 kV is a fairly good indicator of a dirty lamp cathode or impure lamp gas, both of which decrease the intensity of the lamp. After several months of operation the surface of the cathode on which the discharge occurs becomes blackened by deposits of unknown composition. The cathode is easily restored by removing the deposits with emery cloth and steel wool or by sand blasting, after which the cathode

should be thoroughly cleaned with 1,1,1-trichlorethane followed by methanol to remove any oil and debris.

Impurities, primarily air, in the discharge gas not only cause a large number of very intense emission lines to be superimposed on the continuum, but also limit its intensity. The impurity level is most easily determined by recording a lamp output spectrum. Excessive impurities, indicated not only by many intense emission lines but also by absorption lines of nitrogen, are usually due to a leak in the lamp plumbing system. When the lamp plumbing is adequately leakfree it can be pumped down to 10μ and the pressure will remain below about 300μ when the closed system stands overnight.

Another source of impurities can be the compressed helium cylinders and the lamp gas manifold. When helium tanks are changed the lamp gas manifold should be thoroughly pumped out to remove any air that was admitted during cylinder changeover. Once the helium pressure is restored the manifold poses no problem, since it is considerably above atmospheric pressure. The quality of the helium gas varies from tank to tank, even though it has a stated purity of 99.99% (Airco, Inc.). Usually the molecular sieve trap will clean the helium sufficiently, and its use can increase the intensity of the lamp by as much as a factor of two. If one is working in a region where the continuum intensity is low and intense emission lines are a problem, a tank that is sufficiently free of impurities can usually be found by trying several Higher purity helium would alleviate this problem tanks.

but probably is not worth the extra cost since helium of reasonable purity is always available in the chemistry department, and a good clean trap usually provides sufficient cleanliness.

The helium 584 Å line, $(1s2p)^1P + (1s^2)^1S$ transition, is often useful for acquiring mass spectra since it can be produced with high spectral purity and intensity. It was used as the ionization source for the mass spectra presented in this thesis. The 584 Å line is generated by a low pressure d.c. discharge. Maximum intensity is obtained with helium pressures just less than 1 torr and the maximum d.c. power supply current available. The high voltage d.c. power supply from the switching circuit, with the addition of a current-limiting resistor, is used to power the helium line lamp and the maximum current available from the supply is 800 mA. However, for reliable operation a current of 750 mA should be used; at 750 mA the voltage is 1500 V.

The lamp and its power supplies were the biggest instrumental bottleneck of the acetonitrile project. Most of the problems were with high voltage devices. Future operators of the instrument should carefully note that all of the lamp circuitry is potentially lethal even when it is unplugged! Strict precautions must be taken to insure that all devices are disconnected from their powerlines and all capacitors are discharged before checking or troubleshooting the system. If one lacks experience with high voltage devices, help should be obtained from an experienced person whenever there is a

problem. Never work on the high voltage circuits alone, and be sure that someone who knows what to do in case of electrocution is present.

The vacuum tube switching circuit is prone to two problems: arcing and breakdown of the rectifier diodes in the screen power supply. The arcing problem, now that all sharp points have been eliminated, is caused by accumulation of dust on the circuit shown in Figure III-2. The circuit is enclosed in a Plexiglas box, but air is forced through the box to cool the tube. Even though the air entering the Plexiglas box is filtered, after several years of operation enough dust can accumulate to cause problems. On the only circuit board in the Plexiglas box is an optoisolator -- part of the interlock system -- which insures that the screen supply is not on unless the control grid supply is also on. Arcing causes the opto-isolator to turn off, which in turn (through an interlock circuit) shuts off the screen power supply, the Cober pulse generator and the d.c. high voltage power supply. The problem is symptomized by the screen, Cober and d.c. high voltage shutting off as the d.c. high voltage is turned up. Arcing can be diagnosed as the problem by removing the tube and disconnecting the Cober at its terminating resistor, as well as the secondaries of the screen, control grid, and filament transformers. Once this has been done the d.c. high voltage can be turned up to 10-15 kV and if arcing is the problem arcs will be observed at several

locations on the circuit. One should look especially closely at the circuit board containing the opto-isolator. The arcs are very dim and can be seen only in absolute darkness; it takes several minutes for the eyes to acclimate to a point where the arcs can be observed. If arcs are confirmed to be the problem the circuit must be disassembled and all the components thoroughly cleaned. Methanol is a suitable cleaning solvent; acetone is not recommended because it dissolves the paint and labels on the components.

Breakdown of the screen's rectifier diodes can occur when there is input from the Cober while the d.c. high voltage is off. This has happened in a variety of situations and causes current from the filament to be collected by the screen instead of at the tube anode; the screen's rectifier diodes are damaged by this current. The 200Ω resistor in series with the rectifier and the screen was added and the primaries of the transformers were fused to protect the diodes, but they are still damaged occasionally. When the rectifier diodes have been ruined the fuses on the screen transformer primary will blow immediately when the screen is turned on. Damaged diodes are most easily confirmed as the problem by removing the circuit board on which they are located from the Plexiglas box and measuring the forward and reverse resistance of the diodes. This is most easily done with an ordinary ohmmeter, but the meter must use a high enough voltage to measure resistance to make a good diode conduct in the forward direction. For an ohmmeter which uses 1.5 V to measure resistances on the × 100

scale the forward resistance of a good diode should be about 2500 and the reverse resistance infinity. If any one diode in the bridge does not conform to these standards all diodes in the bridge should be replaced. (It is wise to have a reserve set on hand.) When the diodes are replaced the solder connections must be well beaded to eliminate any sharp points which can cause corona which in turn can cause the opto-iso-lator to shut off.

The Cober pulse generator is quite reliable, but since it is primarily a vacuum tube circuit its performance degrades with extended use. If it is suspected that the Cober is not performing up to the standards outlined in its manual, its performance may be checked under a dummy load. The output is most easily and safely monitored with an oscilloscope at the \div 1000 output connector on the front panel. The load should be a 250 Ω , 250 W noninductive resistor. The rise and fall time of the output pulse should be checked as should the peak shape and peak height as a function of the d.c. high voltage and the repetition rate.

If the Cober is not operating up to specification one of its vacuum tubes is probably weak. A tube in good condition will operate properly with the filament voltage reduced to 90% of its normal value whereas a weak tube will not. A Cinch-Jones two-pronged connector has been spliced into the primary side of the filament transformer, allowing one to insert a variac with which the filament voltage can be reduced. To test the tubes one first makes sure that the high voltage

is off and then observes the wave forms with an oscilloscope at the output of each tube under normal filament voltage. The schematics in the manual indicate the location of the test points and the correct wave forms. The observations are then repeated with the filament voltage reduced to 90% of its normal value. If the wave forms change the tube responsible for the change can be isolated and should be replaced. All the tube circuits are potentially lethal and since this testing process requires attaching an oscilloscope probe to the test points, the power should always be disconnected when the probe is moved. Again, it is also important that someone else be present in the room when these tests are performed.

2. Monochromator

The monochromator is a McPherson model 225, 1-meter, near-normal-incidence instrument. The dispersing element is a concave, magnesium fluoride overcoated aluminum grating, ruled with 1200 lines/mm and blazed at 1200 Å. The grating has a reciprocal dispersion of 8.4 Å per mm.

Three fixed entrance slits: $10\mu m$, $50\mu m$, and $100\mu m$, and four fixed exit slits: $10\mu m$, $50\mu m$, $100\mu m$, and $300\mu m$, are mounted on moveable slit plates. The slits can be changed without breaking vacuum via knobs located outside of the vacuum chamber. The wavelength is driven with a stepping motor which can be operated manually or with a computer.

After several months of use the diffraction grating accumulates a thin coating of diffusion pump oil, which significantly reduces its reflectivity in the vacuum ultraviolet and

increases scattered light in the ultraviolet and visible regions of the spectrum. This condition is most easily detected by observing the scattered light intensity in the 100-500 Å range, by using the helium continuum as the light source and a sodium salicylate light detector. The helium continuum produces no light in this region, and with a clean grating no significant amount of scattered light will be observed. However, if the grating is coated with oil a large hump in the light intensity will be observed in this region, with a maximum at about 250 Å. The scattered intensity varies depending on the amount of oil on the grating and its near 250 Å can exceed the true intensity maximum near 800 Å

Oil on the grating will be polymerized by VUV light and therefore the grating should be promptly cleaned whenever scattered light is observed. The grating must be removed from the monochromator and its mask taken off. To remove the oil, the grating is first rinsed with Freon 11 (CFCl₃), followed by a high purity methanol rinse. The methanol rinsing is best done by simultaneously applying the methanol with a squeeze bottle and drying the grating with low pressure, clean, compressed air, working from top to bottom. Great care must be taken not to touch the ruled surface of the grating. When the grating is reinstalled in the monochromator it will have to be realigned and focused, by following the procedure in the monochromator manual.

3. Ionization Region

The ion source is a cubical, stainless steel box, one inch per side, located one centimeter beyond the exit slit of the monochromator. It has two rectangular apertures on opposite sides to enable transmission of the photon beam; on the horizontal perpendicular to the optic axis is a one-fourth inch diameter ion exit hole. The ion aperture is covered with a fine wire grid to minimize penetration into the source of electric fields from ion focusing lenses located just outside. An electrically-insulated, stainless steel plate, the repeller, is positioned inside the source, across from the ion exit aperture. An adjustable voltage is applied to the repeller to accelerate the ions from the source.

The sample is admitted through a tube located behind the repeller and the sample pressure is measured through a tube in the top of the ion source. The sample pressure is controlled with a Granville-Phillips model 203 leak valve and measured with a Datametrics model 1014-A barocell capacitance manometer. The manometer and leak valve are outside of the high vacuum.

4. Mass Spectrometer and Ion Optics

The ions are guided from the ion source and focused onto the quadrupole mass filter with four electrostatic aperture lenses. The quadrupole mass filter is an Extranuclear model 324-9 with 1.9 cm diameter × 22 cm long rods and is powered by a model 311 power supply, equipped with a model E high-Q head. The ion lenses were supplied with the mass filter.

The transmitted mass is controlled by a dial on the front

panel of the quadrupole power supply or by a voltage applied to a connector on the back of the power supply. When measuring a PIE curve the mass filter is used in the fixed mass mode, the mass being selected with the front panel dial. However, to obtain a mass spectrum the transmitted mass is scanned by applying a voltage ramp to the connector on the back panel. Part of this thesis research included the design and construction of a digital ramp generator that allows manual or computer control of the transmitted mass. Details of the circuit are given in Appendix A.

5. Ion and Photon Transducers

The ion transducer, located on-axis at the exit hole of the quadrupole, is a Channeltron continuous-dynode electron multiplier supplied by Galileo Electro-optics. Most of the acetonitrile data were collected with a model CEM 4028 Channeltron, but unfortunately in the course of modifications it was broken; it has been replaced with a CEM 4816 Channeltron. The CEM 4816 has the advantage of being linear up to higher count rates; it has a lower gain than the CEM 4028, although the difference in gain is very small. The CEM 4816 has been used for both positive and negative ion detection and the circuits used for each mode are shown in Figure III-4.

The Channeltron output is measured either as direct current or pulse-counted. In the former mode the output is amplified with a Keithley model 417 electrometer. However, since the direct current method has several disadvantages

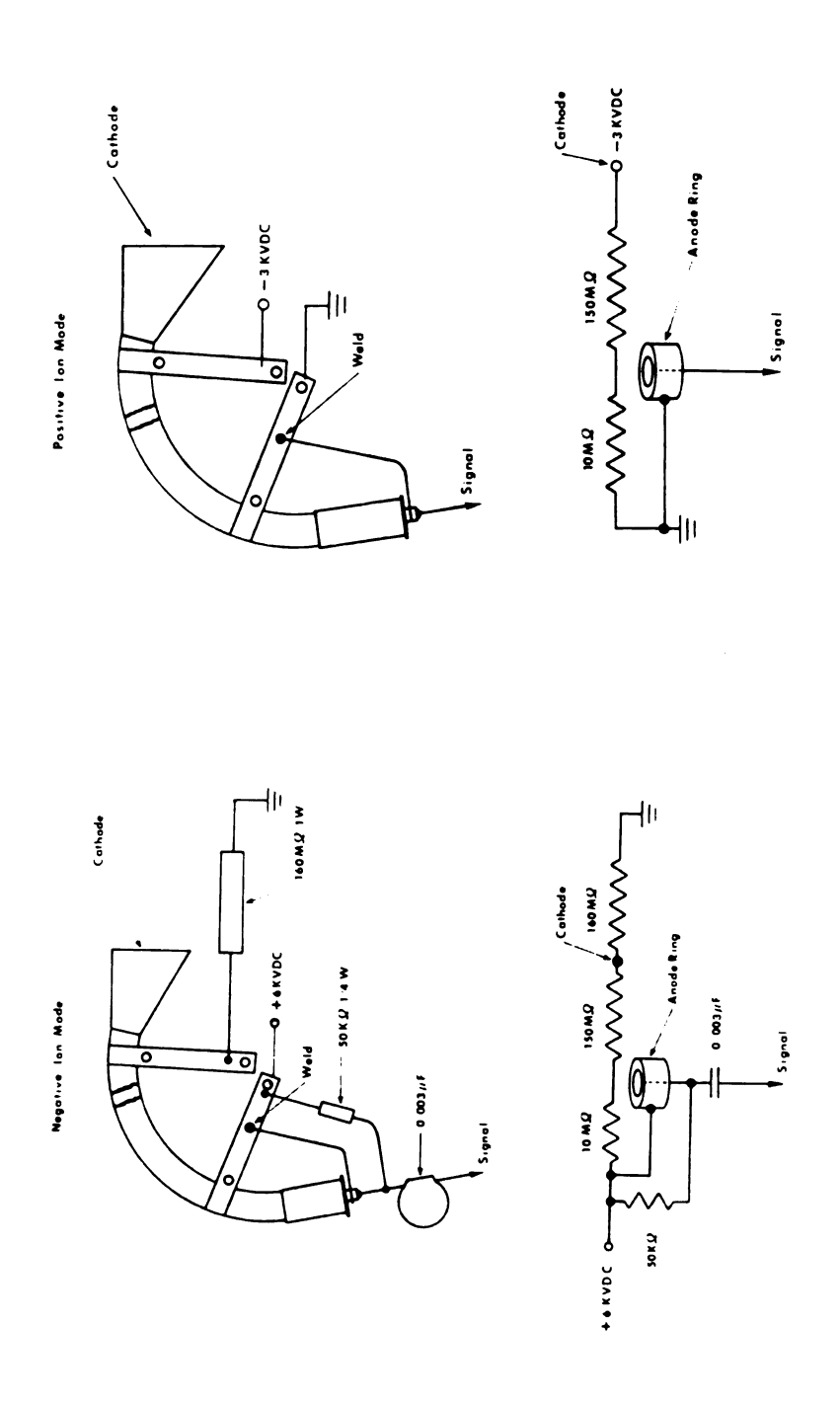


Figure III-4. Channeltron (CEM 4816) Wiring Diagrams for Positive and Negative Ions.

compared to pulse counting when the output current is small, ⁵⁹ it was used only for setting up an experiment. All data were collected with the pulse counting technique, where the output pulses are amplified and discriminated with a circuit developed at MSU, ⁶⁰ and the counts are accumulated with a computerinterfaced counter. ¹⁹ In the negative-ion mode pulse counting must always be used due to the need for a high voltage blocking capacitor on the Channeltron output.

The photon transducer is a sodium salicylate phosphor whose emission intensity is measured with an RCA 8850 photomultiplier tube. Sodium salicylate is superior to ordinary (bare) photomultipliers because it possesses a nearly constant quantum yield throughout the helium continuum. The sodium salicylate emission band does not shift with the exciting wavelength and the emission intensity can be accurately measured with a standard photomultiplier. The output current of the photomultiplier is amplified with a Keithley 1800 current amplifier, and the output voltage is digitized with a voltage-to-frequency converter and a computer-interfaced counter. 19

6. Vacuum System

The monochromator is isolated from the discharge lamp with two stages of differential pumping. The first stage is a 300 l/sec four-inch diffusion injector pump. The monochromator chamber is pumped with a six-inch, 2400 l/sec diffusion pump, as is the sample region. The quadrupole region is pumped with a six-inch 1800 l/sec diffusion pump.

The pumping speeds quoted are for untrapped pumps; however, all four diffusion pumps are trapped with Freon-cooled baffles which reduce the pumping speeds somewhat. All the pumps can be isolated from the experimental vacuum chamber with pneumatically-operated gate valves.

7. Data Collection

Once an experiment is set up, data collection and storage are controlled with a PDP 8/M or PDP 8/I minicomputer. The data are collected by using a variable integration time technique which permits recording data of the desired quality in an optimum amount of time. 59 The monochromator wavelength is stepped in preset intervals, and at each wavelength ion and photon counts are accumulated until the datum has the desired signal-to-noise ratio. Photon and ion count rates, wavelengths and integration times are stored on a floppy or hard disk. The course of the experiment is continuously monitored via a computer-interfaced, stepped, stripchart recorder on which the real-time PIE is plotted. Periodic measurements of "light" and "dark" photon and ion count rates are made at a reference wavelength so that the data can be corrected for sample pressure and instrumental drift. Approximate corrections for stray light are made by measuring the light intensity at two wavelengths where the helium continuum does not emit. Final corrections of the data for sample pressure, instrumental drift and stray light, as well as the final plot, are done with the MSU Chemistry Department's Cemcomgraph computer facility. 61

C. Experimental Details

1. Samples

Reagent grade protonated acetonitrile ($\mathrm{CH_3CN}$) was obtained from the Aldrich Chemical Co. and acetonitrile- $\mathrm{d_3}$ ($\mathrm{CD_3CN}$) from Stohler Isotope Chemicals. The deuterated compound had a stated atom purity of 99.5% D. Air was removed from the samples through the freeze-pump-thaw technique; the samples were frozen with a dry ice-methanol bath. No further purification was done on the protonated compound; however, the deuterated material was contaminated with sufficient quantities of $\mathrm{D_2O}$ and HDO that OD^+ was observed in the $\mathrm{CD_3^+}$ PIE. For collection of the $\mathrm{CD_3^+}$ PIE the sample was dried with molecular sieves and calcium hydride.

The samples were contained in pyrex bulbs which were connected to the leak valve via a glass-to-metal seal and a short length of copper tubing. The temperature of the room in which the instrument is located varies by as much as 5° F over a period of several hours. To minimize the effects of temperature variation on the sample vapor pressure the sample containers were placed in a half-liter Dewar flask filled with water. The data were collected with sample pressures between $4.5 - 5.5 \times 10^{-4}$ torr, and the pressure varied by less than 10% throughout an experiment.

Proton transfer from the acetonitrile parent ion (CH₃CN⁺) to neutral acetonitrile to form CH₃CNH⁺ is an exothermic reaction with a large cross section at low relative kinetic energies. The relative intensity of CH₃CNH⁺ with respect

to CH₃CN⁺ is strongly dependent on the conditions in the ion source. With small potential differences between the repeller and the ion source (less than 1 volt) and a sample pressure of 5×10^{-4} torr the intensity of CH_3CNH^+ is nearly half the intensity of CH3CN+. Because first-order processes were of primary interest and the proton transfer reaction significantly reduced the intensity of the parent ion, the reaction was suppressed by using a rather large potential difference between the repeller and the ion source (=10 V). This reduces the residence time of the ions in the ion source and therefore decreases the chance of a reactive interaction with the neutral compound. For the work reported here the repeller was maintained at +13.8 V and the ion source at +3.8 V. The remaining ion lenses -- the extractor, lenses 1, 2 and 3, arranged in that order as the ions pass from the source to the quadrupole-were set at -18.4 V, -44.8 V, -6.12 V and -5.4 V, respectively. This combination reduced the intensity of CH3CNH to less than 19% of the CH₃CN⁺ intensity, maximized the CH₃CN⁺ signal and provided good mass spectrum peak shapes.

The mass filter was always set to the minimum resolution possible to just prevent overlap of ions that differed in mass by 1 u.

Monochromator entrance and exit slits of 100 μm , which give 0.84 Å fwhm band pass, were used for all the PIE measurements reported here, except for the threshold regions of the parent ions; these were also measured with $50\mu m$ entrance and exit slits, providing a 0.42 Å fwhm band pass. Data recorded

with 100 μ m slits were taken in steps of 0.25 Å, whereas 0.15 Å steps were used with 50 μ m slits.

Integration and experiment times varied considerably depending on the intensity of the ions and photons in the region of interest, the slit width, the size of the wavelength step, and the desired quality of the data. An attempt was always made to record the data with a signal-to-noise ratio of at least 100. For the PIE curves reported here, this required experiment times ranging from 12-48 hours.

CHAPTER IV

RESULTS AND DISCUSSION

Photoionization of Acetonitrile

A. Previous Studies

Prior to the investigation reported here, studies of photo-ionization of acetonitrile had been reported by Watanabe, et al., 63 Nicholson, 4 and Dibeler and Liston. 65 The data obtained in references 63 and 64 were recorded without mass analysis and therefore only the total ionization efficiency could be measured. In both papers it was correctly assumed that the observed threshold was that of the parent ion; in neither paper were PIEs reported. Dibeler and Liston used mass analysis and measured the ionization potential of acetonitrile as well as appearance potentials of $\mathrm{CH_2CN}^+$, CHCN^+ and $\mathrm{CH_2^+}$; however, again no PIEs were published. The results of these three publications are gathered in Table IV-5 together with the results of this investigation, and will be discussed along with the data reported here.

B. The Photoelectron Spectrum

The photoelectron spectrum (PES) of acetonitrile has been reported. 55,66,67 The PES of CH₃CN from reference 55 is reproduced in Figure IV-1. The conclusions are as follows. The first band, with its origin at 12.21 eV in Figure IV-1, results from the removal of an electron from the C \equiv N π -orbitals,

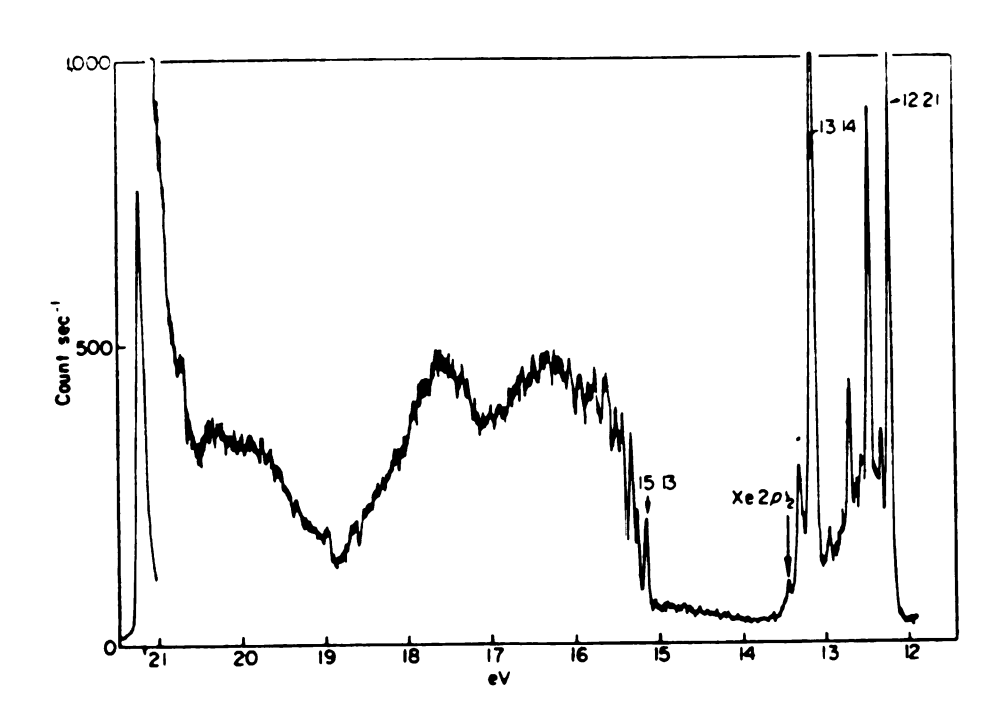


Figure IV-1. Photoelectron Spectrum of CH₃CN (from Reference 55.)

as indicated by the vibrational structure of the band. The observed vibrational modes and their frequencies in the parent ion are compared to those of the neutral in Table IV-1. Three modes are excited in the ground state of the ion: the C \equiv N stretch (ν_2) , the symmetric CH $_3$ deformation (ν_3) , and the C-C stretch (ν_4) . This assignment is supported by the CD $_3$ CN spectrum. When compared to the ground state neutral molecule, the frequencies of the C \equiv N stretch and the C-C stretch decrease in the ion, while the CH $_3$ symmetric deformation frequency increases. This indicates that the orbital from which the electron is removed is C-N and C-C bonding, but C-H antibonding, thus a π -orbital of the C \equiv N bond. This π -orbital has E symmetry in the C $_{3v}$ point group and can be labelled as the 3e orbital. 68,69

The second band, with its origin at 13.14 eV, has very little vibrational structure. The band has been assigned to the removal of an electron from the nitrogen lone pair, and the single vibrational excitation observed to the CH₃ symmetric deformation (ν_3). Since the nitrogen lone pair participates little in the bonding, loss of one of the electrons should have little effect on the structure of the molecule, as is indicated by the paucity of vibrational excitation in the photoelectron band. The nitrogen lone pair can be labelled as $5a_1$. The assignment of the remaining PE structure, in the region from 15-21 eV, is considerably less certain, but it must result from ionization of C-C and C-H σ bonds. Turner identifies the vibrational structure at the head of the band

Table IV-1. Vibrational Modes and Frequencies of $\mathrm{CH_3CN}^+$ and $\mathrm{CD_3CN}^+$ Excited in the Photoelectron Spectra compared to the Frequencies of the Neutral.

State of ion	Vibrational mode excited	Frequen CH ₃ CN ⁺	CH ₃ CN ^a	Frequen CD ₃ CN ⁺	$\frac{\text{cy} (\text{cm}^{-1})}{\text{CD}_3 \text{CN}^2}$
$\widetilde{\chi}$	ν ₂ C N stretch	2010	2267	1990	2278
	v_3 symm. CH_3 def.	1430	1385	1070	1110
	ν ₄ C-C stretch	810	920	810	831
B	v_3 symm. CH $_3$ def.	1290	1385	970	1110
č	v_3 symm. CH_3 def.	1440	1385	—-b	1110
	v_{4} C—C stretch	860	920	—b	831

aVibrational frequency in the ground electronic state of the neutral; taken from reference 88.

bnot determined.

as arising from the ${\rm CH_3}$ symmetric deformation (v_3) and the C-C stretch (v_4) ; the changes in these frequencies from the neutral molecule suggests that the orbital ionized is C-H antibonding and C-C bonding. Frost, et al., 66 does not even attempt an analysis. However, it is clear that in this region there are two bands: one centered at about 16 eV, the other at 17.5 eV, and that ionization from orbitals that are involved with C-C and C-H bonding is implicated in both cases. The absence of a strong transition at the origin indicates that at least some bond lengths have changed considerably. (The band centered at about 20 eV in Figure IV-1 may be an instrumental artifact. 55)

It can be concluded that there are two well defined states and at least two poorly defined states of the acetonitrile parent ion that will be accessible by direct ionization in a PIMS experiment. The ground state of the ion has several bond lengths and vibrational frequencies that differ from those of the neutral molecule, while the vibrational frequencies and bond lengths of the first excited state of the ion are probably very similar to those of the neutral molecule.

The PES ionization potentials reported for $\mathrm{CH_3CN}$ in references 55,56, and 67 are listed in Table IV-5, along with the photoionization data. Although these PES investigations indicated that the spectrum of $\mathrm{CD_3CN}$ was recorded, only Lake and Thompson⁶⁷ reported IPs for $\mathrm{CD_3CN}$.

C. The Photoionization Mass Spectra of $\mathrm{CH_3CN}$ and $\mathrm{CD_3CN}$ The 584 Å (21.2 eV) photoionization mass spectra (PMS) of $\mathrm{CH_3CN}$ and $\mathrm{CD_3CN}$, recorded in the present study, are shown in Figure IV-2. Relative intensities and assignments are presented in Table IV-2. The electron impact mass spectrum (EIMS) of $\mathrm{CH_3CN}$ 62,70,71 shows slightly more fragmentation than the PMS, but the overall agreement between the two spectra is good, and the small differences can be attributed to the higher ionizing energy (50-80 eV) used in the EI experiments.

Most of the assignments of the PMS and EIMS are straightforward even though the deuterated compound was slightly proton contaminated; however, some of the assignments deserve comments. Gray 62 suggested that m/e=15 from CH₃CN might contain some contribution from NH $^+$ since a small amount of NH $^+_2$ (m/e=16) is detected. Therefore the peaks assigned as CD $^+_2$ and CD $^+_3$ (m/e=16,18) might also have some contribution from ND $^+$ and ND $^+_2$, respectively. However, thermochemical calculations show the thresholds for NH $^+$ and NH $^+_2$ to be considerably above those for CH $^+_2$ and CH $^+_3$, so that NH $^+$ (ND $^+$) and NH $^+_2$ (ND $^+_2$) would probably not contribute significantly to the 21 eV PMS. Indeed, no peak is observed at m/e=16.

The high resolution EIMS⁷⁰ of CH_3CN shows that m/e=26 and 27 are multiple peaks (m/e=26 is 60% CN^+ and 40% $C_2H_2^+$, and m/e=27 is 85% HCN^+ and 15% $C_2H_3^+$ at the unstated, but probably >50 eV ionizing energy). However, this need not be of concern in this investigation, since the intensity of these ions is

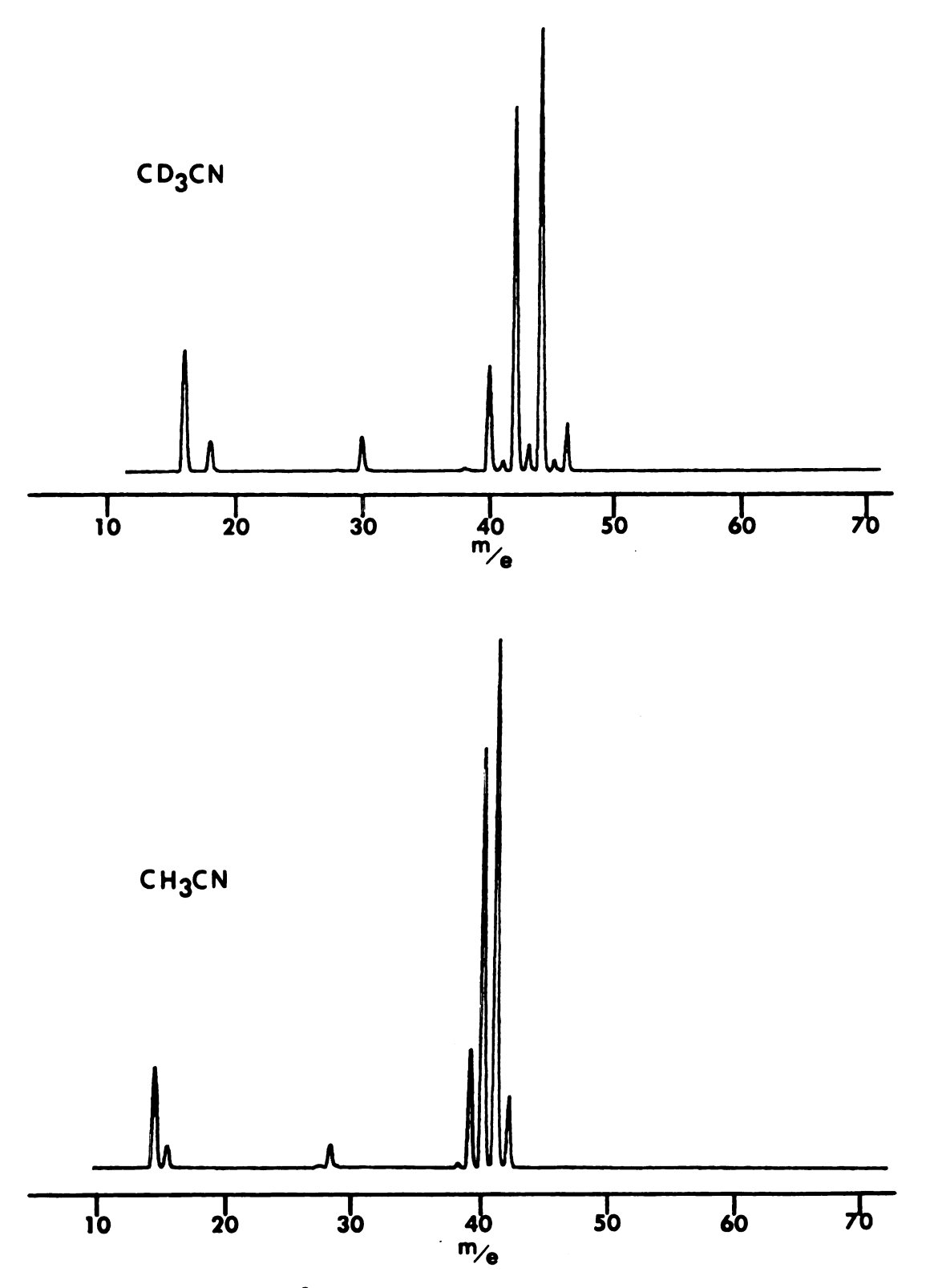


Figure IV-2. 584 Å (21.2 eV) Photoionization Mass Spectra of CH₃CN and CD₃CN. (Quantitative Relative intensities should not be measured from these spectra.)

Table IV-2. CH_3CN and CD_3CN Photoionization Mass Spectra. (Ionization energy = 21.2 eV.)

CH ₃ CN			CD ₃ CN		
m/e	Intensity Relative to CH ₃ CN ⁺ (m/e=41)	Assignment	Intensity Relative to CD ₃ CN ⁺ (m/e=44)	Assignment	
14	18.2	CH ₂ +			
15	4.4	Сн ₃ +	<1	CHD ⁺	
16			27.6	CD ₂ +	
17			<1	CHD ₂ ⁺	
18			6.8	CD ₃ ⁺	
26	<1	CN ⁺ ,C ₂ H ₂ ⁺			
27	<1	$HCN^+, C_2H_3^+$			
28	5.2	H_2CN^+, N_2^+	<1	DCN ⁺ ,N ₂ ⁺ ,C ₂ D ₂ ⁺	
30			8.1	D ₂ CN ⁺ ,C ₂ D ₃ ⁺	
38 39	1.2 23.0	C ₂ N ⁺ HC ₂ N ⁺	1.2	c ₂ n ⁺	
40	78.7	н ₂ с ₂ м ⁺	22.7	DC2N+, (H2C2N+)	
41	100	H ₃ C ₂ N ⁺	2.3	$HDC_2N^+(H_3C_2N^+)$	
42	13.3	H ₄ C ₂ N ⁺	80.4	$D_2C_2N^+$, $(H_4C_2N^+)$	
43		-	6.0	HD ₂ C ₂ N ⁺	
44			100	D ₃ C ₂ N ⁺	
45			3.2	HD ₃ C ₂ N ⁺	
46			19.0	D ₄ C ₂ N ⁺	

too low below 21 eV for a PIE curve to be measured. The peak at m/e=28 in the PMS of CH_3CN does contain some contribution from N_2^+ , but it is quite small as can be ascertained by comparison with the CD_3CN PMS. However, the N_2^+ PIE curve is quite distinct and N_2^+ did interfere with the H_2CN^+ PIE curve. (See section IV-E5.)

The small differences in the ${\rm CH_3CN}$ and ${\rm CD_3CN}$ PMSs are mostly attributable to a difference in the sample pressure (if contributions from the protonated impurity in the ${\rm CD_3CN}$ sample are neglected). The ${\rm CH_3CN}$ PMS was recorded with a sample pressure of 4.9×10^{-4} torr and the ${\rm CD_3CN}$ with a pressure of 5.2×10^{-4} torr. This 6% descrepancy was unintentional, but it serves to demonstrate the pressure dependence of the reaction of the parent ion with the neutral sample to produce ${\rm CH_3CNH}^+$ (${\rm CD_3CND}^+$). Due to the higher pressure of ${\rm CD_3CN}$, the relative intensity of the reaction product is greater in the ${\rm CD_3CN}$ PMS. Thus more of the parent ions initially formed are detected as P+2 in the ${\rm CD_3CN}$ PMS which accounts for most of the higher relative intensities of the fragment ions in the ${\rm CD_3CN}$ PMS compared to the ${\rm CH_3CN}$ PMS.

CH₃CN⁺, CH₂CN⁺, CHCN⁺, H₂CN⁺, CH₃ and CH₂, as well as their deuterated analogs, are produced with sufficient intensity to enable PIE curves to be recorded. Pressure-dependence studies show that all of these are primary ions. The absolute intensity of CH₃CN⁺ and CD₃CN⁺ in the mass spectra are about 3500 ions/sec, which is more than twice the

intensity that they are produced at the maximum (~800 $\mbox{\AA}$, 15.5 eV) of the helium continuum.

A search was made for negative ions and CN and CH₂CN ions were detected; however, their intensity was much too low for PIE curves to be recorded.

D. Parent Ion PIE Curves

1. General Observations

The PIEs of CH₃CN⁺ and CD₃CN⁺ are presented in Figure On the scale of the figure the two PIEs should be, and are, identical. There is a distinct threshold at about 1015 ${\hat{\rm A}}$ (12.2 eV), followed by an autoionizing Rydberg series converging to the first excited state of the ion. From the photoelectron spectrum, the threshold of the first excited state should be about 944 $ilde{A}$ (13.1 eV) and the jump in the PIE at approximately 944 Å is the threshold for this state. The distinctness of the feature at 944 Å indicates that the Rydberg states converging to the first excited state of the ion are strongly predissociating into neutrals, as well as autoionizing, since no ion fragments are observed in this region. If the Rydberg states were not predissociating the Rydberg series would join smoothly onto the direct ionization continuum of the first excited state. Acetonitrile is known to predissociate into neutral fragments at energies considerably less than 13 eV. 70

The region between 944 Å (13.1 eV) and 820 Å (15.1 eV) corresponds to a blank region in the PES spectrum, and thus additions to the PIE from direct ionization to new states are

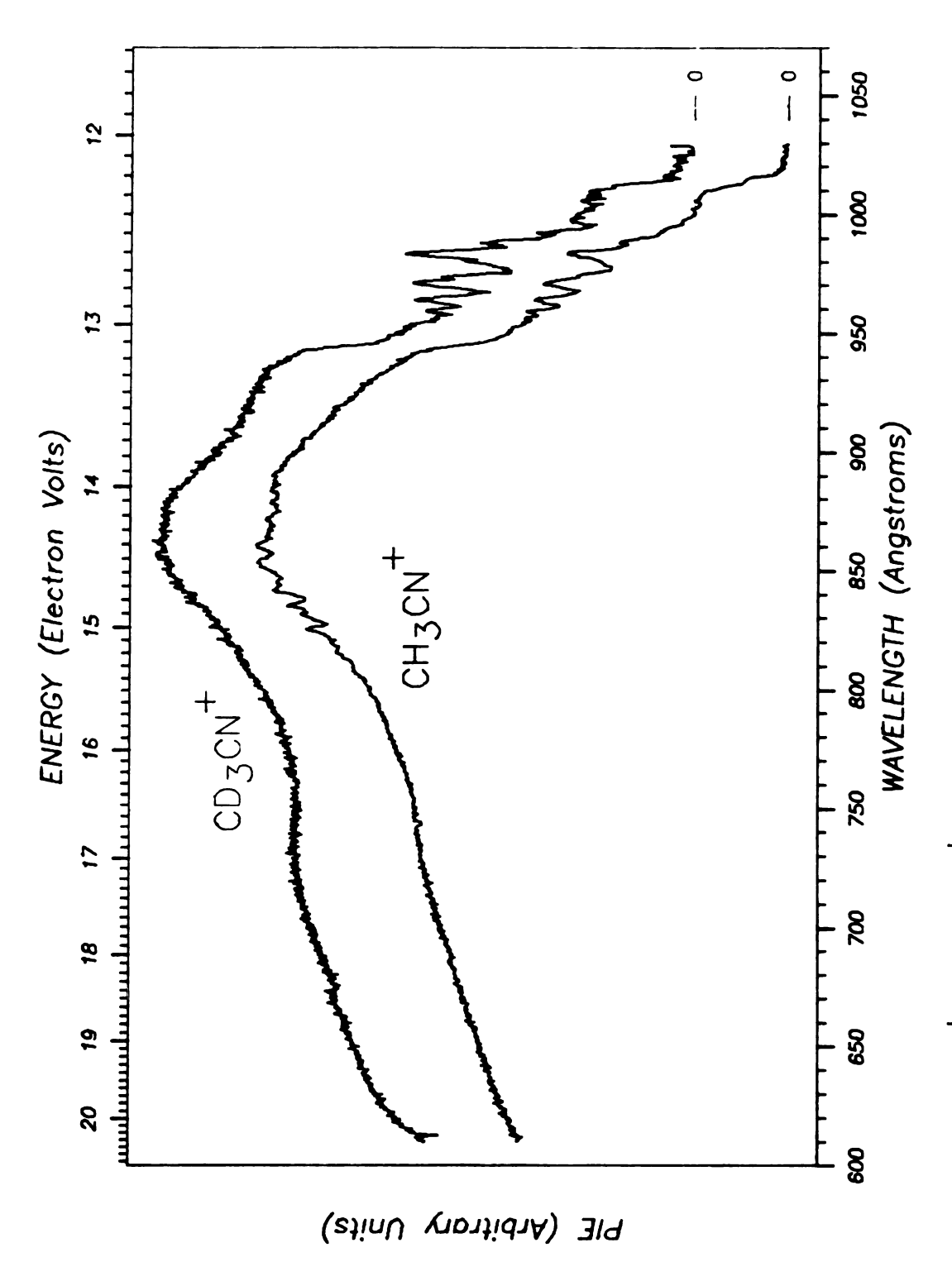


Figure IV-3. CH_3CN^{\dagger} and CD_3CN^{\dagger} PIE Curves: 600-1040 Å.

not expected. Nevertheless, as the photon energy rises following the threshold of the first excited state, the PIE increases. This could be due to an increase in the direct ionization cross section to the first excited state of the ion, but it is most probably due to autoionization. The evidence for autoionization is the onset of fragmentation in this region. Therefore states above the first excited state of the ion are populated following photon absorption, but they must be populated by autoionization since the photoelectron spectrum indicates that there are no ionic states in this region available for direct ionization. Moreover, in the $\mathrm{CH}_3\mathrm{CN}^+$ PIE there is some structure in the 885-800 Å range which can only be attributed to autoionization. The leveling-off of the PIE at about 885 Å (14.0 eV) correlates well with the fragmentation threshold for the first fragment, CH2CN+, and the decrease in the PIE from 885 $\mbox{\normalfont\AA}$ to 820 $\mbox{\normalfont\AA}$ (15.1 eV) is due to cessation of the autoionizing Rydberg series caused by fragmentation. the parent ion states populated by autoionization in this region fragment and are not detected as parent ions. demonstrated in Figure IV-4 in which the dashed line is the total ionization PIE, the sum of parent and fragment ions. The total PIE actually increases.

From the PES spectrum, the threshold for the second excited state of the ion is at approximately 820 Å (15.1 eV). However, there is no discontinuity in the PIE near 820 Å. This is due to a combination of two factors. First, there are Rydberg states converging to this ionic state and the autoionization

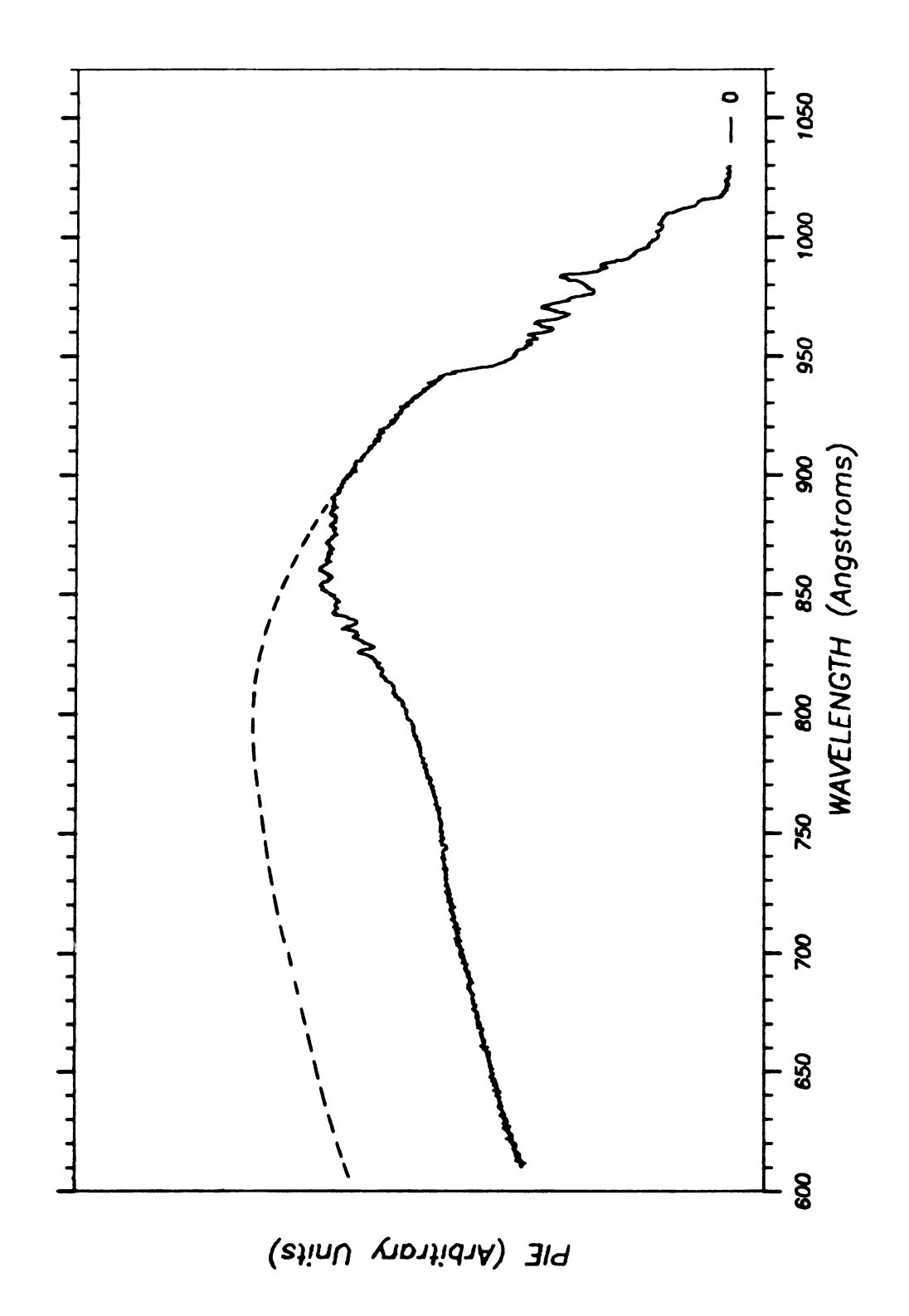


Figure IV-4. Total PIE of CH3CN. (Dashed line indicates the total PIE.)

may join smoothly onto the continuum and hide the threshold. Second, and probably more important, is the likelihood that all, or nearly all, of the parent ions formed in the second excited state are dissociated into ion fragments on the time scale of the PIMS experiment. No discontinuity would be expected because no parent ions formed in this state would be detected as P⁺. It is a general observation for polyatomic molecules that most, if not all, ions formed with internal energies above the first fragmentation threshold dissociate. 13,14 The first fragmentation threshold for acetonitrile is at approximately 885 Å (14.0 eV), well below the threshold of the second excited state. In acetonitrile some ions formed with internal energies just above the first fragmentation threshold do not dissociate, otherwise the autoionization beyond 944 Å would not be observed in the $\mathrm{CH_2CN}^+$ PIE. However, the second excited state is more than 1 eV beyond the onset of fragmentation and is, most surely, nearly completely dissociated.

The region beyond 820 Å in the parent ion PIE, to 600 Å (20.7 eV), then, would show no evidence of ionic states above the second excited state. The PIE in this region thus reflects the cross sections for direct ionization to the ground and first excited states of the ion. As would be expected in this case, the PIE slowly and smoothly decreases with increasing photon energy. ²²

Upon close examination, however, there are some small, but very important, differences in the PIE curves for ${\rm CH_3CN}^+$ and

CD₃CN⁺. In the following sections a more detailed examination of the autoionization structure and the threshold regions of these curves is presented.

2. Autoionization Structure: 1040 Å - 940 Å

The CH₃CN⁺ and CD₃CN⁺ PIEs between 1040 Å (11.9 eV) and 940 Å (13.2 eV) are shown in Figures IV-5 and IV-6. Members of two Rydberg series are readily apparent and are indicated on the horizontal line near the top of the figures. Only two members of the weaker series are resolved; this is due to the broad line widths of the series members and not to instrumental resolution. Fridth⁷² has reported the electron impact energy loss (EIEL) spectrum of acetonitrile and has also observed these two series. In the following pages the assignment of the series type and the series limit are discussed.

The PES provides an initial estimate of the series limit. The location of the first excited state of the ion is known from the PES. From inspection of Figures IV-5 and IV-6 it can be seen that the series are converging to this state, and therefore the Rydberg series arise from excitation of the 5a₁ orbital of the neutral molecule. The quantum defect, which is a primary consideration in the assignment of a Rydberg transition, can then be calculated by using the photoelectron ionization potential of the 5a₁ orbital in the Rydberg equation:

$$E_{h\nu} = IP - \frac{R}{(n - \delta)^2} . \qquad (II-4)$$

However, another option is to fit a series to the Rydberg

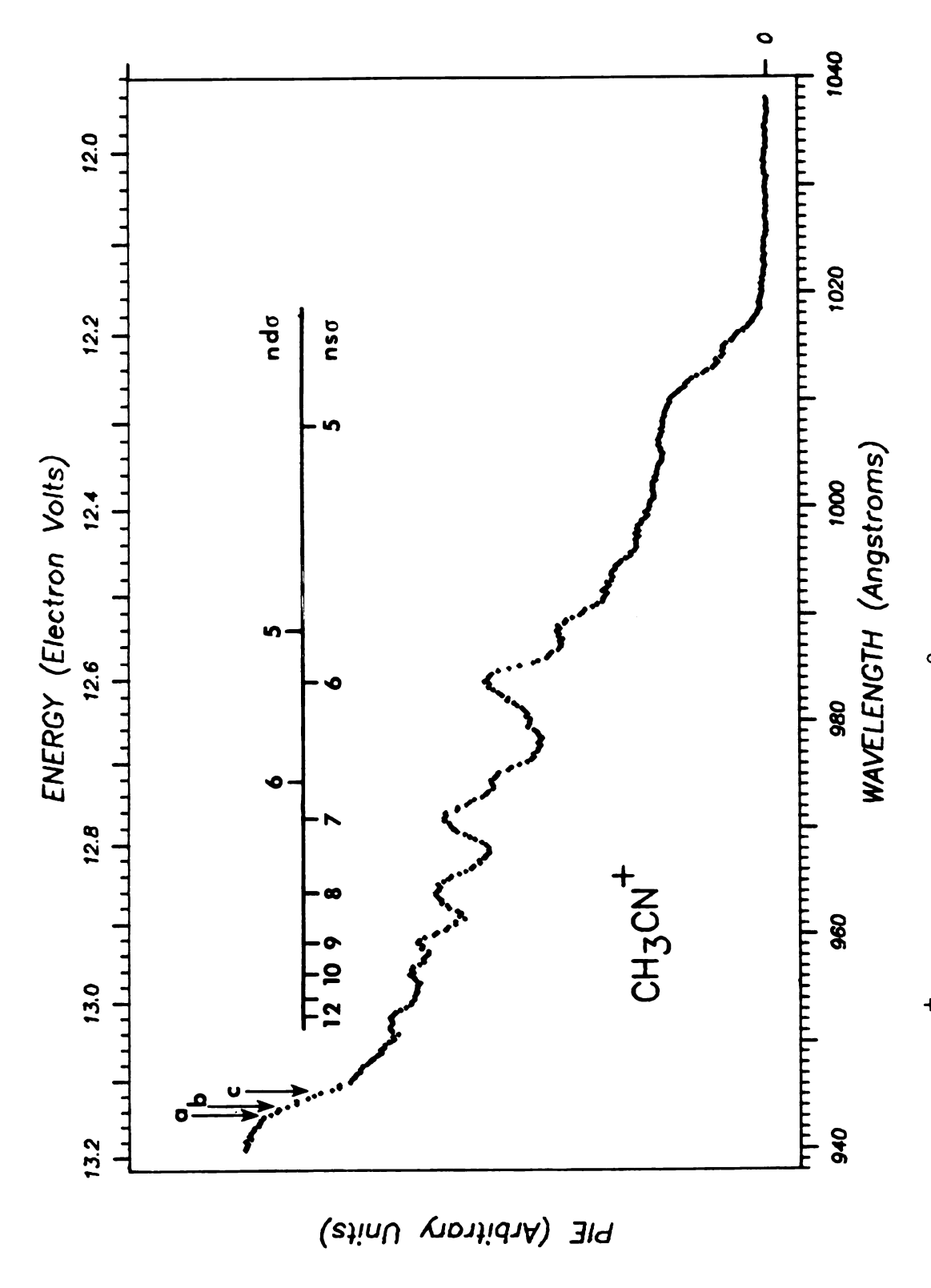


Figure IV-5. CH₃CN⁺ PIE Curve: 940-1040 Å.

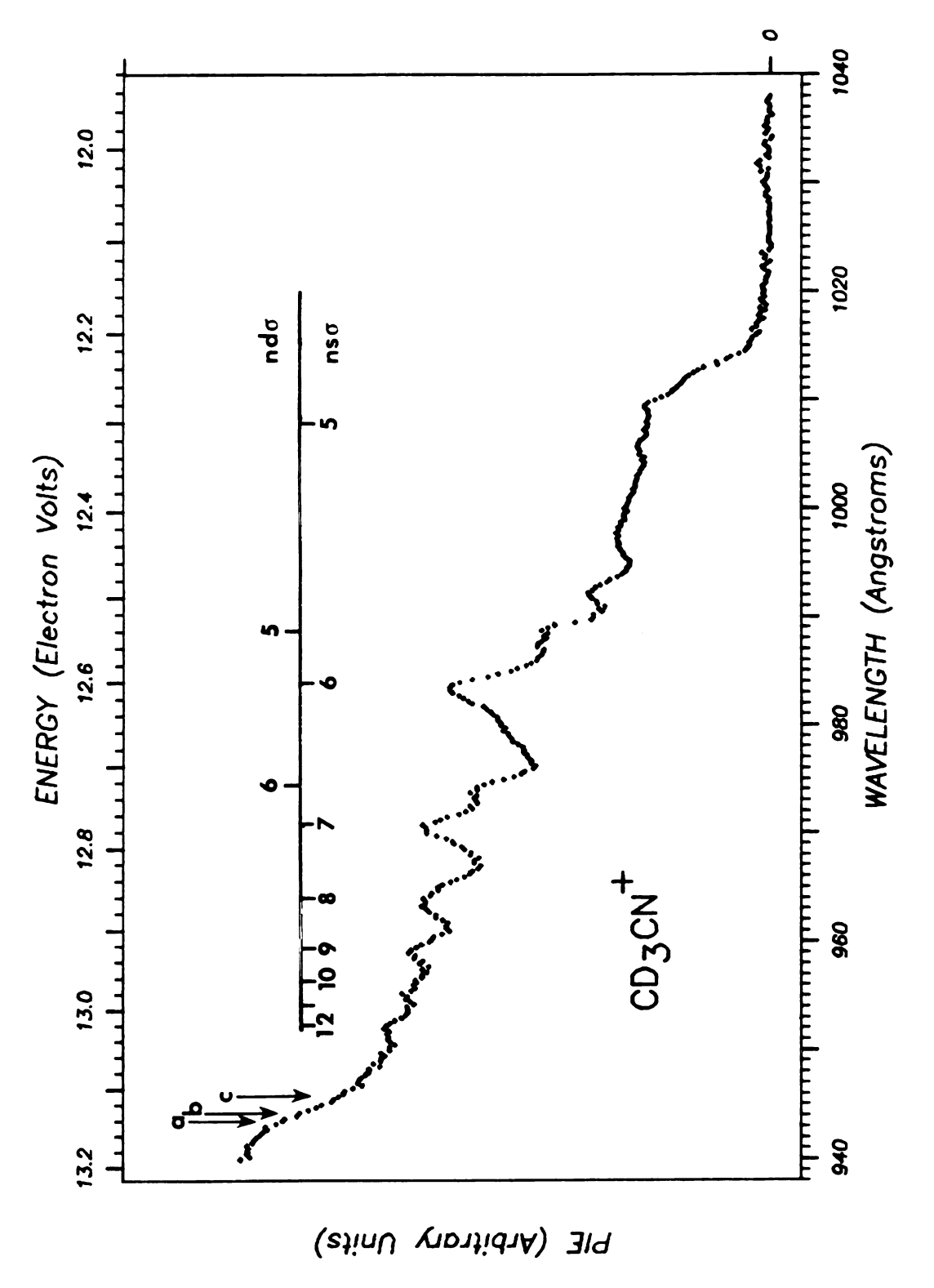


Figure IV-6. CD₃CN⁺ PIE Curve: 940-1040 Å.

equation with the ionization potential and the quantum defect as adjustable parameters. Very accurate ionization potentials can be determined by this method. 73

The more intense of the two series observed in the ${\rm CH_3CN}^+$ and ${\rm CD_3CN}^+$ PIE curves was fit to the Rydberg equation by means of KINFIT 4, a general non-linear, least-squares curve-fitting computer program. The series limit and the quantum defect were taken as adjustable parameters. The quantum defect was assumed to be constant as a function of n. Although this is not strictly correct, the error that results for n \geq 5 for a molecule composed of second row atoms is negligible. The fitting for the photoionization data. The results of the fits are given in Table IV-3 along with the experimental locations of the observed series members.

First consider the series limit. The photoelectron ionization potentials reported for the 5a₁ orbital are 13.11 eV⁶⁶ and 13.14 eV.^{55,67} Although no error limits were published, the PES spectra were probably recorded on instruments with about 50 meV resolution, as will be shown when the lowest ionization potential is discussed. With 50 meV resolution peak positions can usually be measured to within about 10 meV.⁹ Fridth's EIEL data were also collected with an electron energy analyzer having about 50 meV resolution.

The PIE data were obtained with a photon bandwidth of 0.84 Å; at 980 Å this corresponds to an energy bandwidth of 11 meV. It was possible to locate the autoionization peak

Tab

Ser lir

ns

nd

a_E

c (

Table IV-3. Rydberg Series Converging to the First Excited State of CH₃CN⁺ and CD₃CN⁺.

		CH ₃ CN			CD3CN		
	This work		rk	Fridth ⁷²		This work	
Seri	es t(eV)	13.133	± .004ª	13.135	± .006 ^b	13.136	± .004
~δ (n	sσ)	.93	± .04	1.01	± .004	.92	± .04
		rimental o			l δ calcu	lated from	m series
	n	energy(eV) δ	energy(eV) δ		energy(eV) δ	
nsσ	3			9.713	1.01 ^b		
	4			11.594	1.03		
	5			12.295	0.98		
	6	12.601	0.94	12.596	0.98	12.606	0.93
	7	12.775	0.84	12.759	0.99	12.775	0.86
	8	12.864	0.89	12.854	1.03	12.868	0.88
	9	12.924	0.93	12.92	1.05	12.925	0.97
	10	12.964	1.03				
	11						
	12	13.020	1.03			13.023	1.03
ndσ	4		~	12.180	0.23		
	5	12.542	0.22 ^C	12.534	0.24	12.550	0.182
	6	12.724	0.23	12.706	0.37	12.732	0.200

aErrors are linear estimates of the standard deviation.

 $^{^{\}mathbf{b}}$ Results of this investigator's fit of Fridth's pg series.

 $^{^{\}textbf{C}}_{\mbox{Quantum defects}}$ for the $nd\sigma$ series were calculated from limits of $ns\sigma$ series.

centers to within \pm 0.5 Å or \pm 6 meV at 980 Å. Furthermore, the photoionization data have a built-in calibration — the atomic emission lines in the light source output — which the photoelectron and electron impact data lack. If the fit is reliable the photoionization data should provide a more accurate value for the $5a_1$ ionization potential. The series limits obtained from the fit to the photoionization data are 13.133 ± 0.004 eV for CH₃CN and 13.136 ± 0.004 eV for CD₃CN. The estimates of the standard deviation indicate that the fit is quite good. However, because the Rydberg series fit is an indirect method it could be argued that the small difference between the Rydberg series limit and the photoelectron ionization potential is not significant.

However, the PIEs present a very fortunate situation. If the step at 944 Å is indeed the threshold for ionization from the $5a_1$ orbital, then an independent measure of this orbital ionization energy is available. Generally, when a step corresponding to the threshold for direct ionization to a vibronic state of an ion is observed, the point on the step corresponding to the peak center in a resolved photoelectron line, the ionization potential for the vibronic state, will be at the inflection point or midpoint of the rise of the step. This assumes that autoionization does not significantly contribute to the step. Because the autoionization intensity in ${\rm CH_3CN}^+$ and ${\rm CD_3CN}^+$ is low in this region, and because there is a fairly sharp break at the foot of the step, autoionization probably does not significantly contribute in this case, and the step

should yield an accurate ionization potential. The photo-electron ionization potentials for the 5a₁ orbital (13.14 eV and 13.11 eV) are marked on the PIEs in Figures IV-4 and IV-5. Also marked are the limits derived from the Rydberg series fits. The Rydberg series limits are closer to the midpoints of the steps than are the photoelectron results. Considering the smaller error limits of the photoionization data, the series limits derived from the fits, and the step at the limit, it is concluded that the photoionization result is indeed a more accurate determination of the 5a₁ nitrogen lone pair orbital ionization potential.

The difference between the $\mathrm{CH_3CN}^+$ and $\mathrm{CD_3CN}^+$ limits could be real, due to a difference in the change of the zero point energy between the neutral and the ion in the isotopic molecules. However, since the difference is small — within the error limits — and since 13.133 eV appears to be a better estimate of the center of the step rise in the $\mathrm{CD_3CN}^+$ PIE, it can be concluded that $\mathrm{CH_3CN}$ and $\mathrm{CD_3CN}$ have the same $\mathrm{5a_1}$ ionization potential: 13.133 \pm 0.005 eV.

It is worth noting that some members of the more intense series are missing in the PIE curves, based on the quantum defect and the series limit. For example, the n=5 member should provide an intense peak at 1005 Å, but no distinct peak is observed there. Probably an unbound potential surface of the neutral molecule crosses the n=5 Rydberg series surface, allowing it to be nearly completely dissociated. This member is clearly observed in Fridth's EIEL spectrum, and there are

remnants of it in the PIE. The n=10 member of $\mathrm{CH_3CN}^+$, and n=10 and 11 of $\mathrm{CD_3CN}^+$ are also missing, presumably for the same reason. The n=4 member of the less intense series was also observed by Fridth; 72 it is located below the first ionization potential and therefore would not contribute to the PIE.

Consider next the series assignment. Remembering that s-type Rydberg series have quantum defects of about 1.0, p-type of about 0.6, and d-type of near zero, 28,35 it would be reasonable to assume that the more intense series is an s-type with δ =0.92 and the less intense series a d-type with δ =0.2. On the basis of the photoionization data alone, little more can be said. However, Fridth 2 was able to observe several series members converging to the second ionization potential in the spectroscopic range inaccessible to PIMS (below the first ionization potential), as well as some members above the first ionization potential. Moreover, several series converging to the first ionization potential were observed. With the addition of these data, more definitive assignments are possible. Two optical studies in the vacuum ultraviolet 68,76 and another EIEL investigation 77 of CH₃CN have been reported, but in all three publications either the data were not recorded to high enough energy or were obtained with inadequate resolution to be of much use.

Fridth has assigned all the prominent features in the EIEL spectrum, 72 including the two series observed in this study. The series corresponding to the weaker autoionization in the PIES was designated do with $\delta = 0.23$, and this assignment is

in good agreement with the photoionization results. However, the more intense series was assigned as $p\sigma$ with $\delta=0.97$. As pointed out by Fridth, this assignment is somewhat questionable and this investigator believes that it would be more correctly assigned as an $s\sigma$ series.

Fridth assigned the series in $\mathrm{CH}_{3}\mathrm{CN}$ by analogy with $\mathrm{HCN}.$ The EIEL spectrum of HCN has been reported by Fridth and Asbrink, 78 and they observed two series corresponding to excitation of the nitrogen lone pair. These two series were assigned as so (δ =0.91 for the higher energy members of the series) and $d\sigma(\delta=0.4)$. Later, however, Asbrink, Fridth and Lindholm⁷⁹ published results of a HAM/3 calculation of HCN. (HAM/3 is a semi-empirical technique for calculating valence transitions, developed by Lindholm. 80) From the results of the calculation it was concluded that some structure in the EIEL spectrum of HCN, which had originally been interpreted as Rydberg transitions, was really due to valence transitions. The Rydberg transitions then needed to be reassigned. As a result only one series, corresponding to excitation of the nitrogen lone pair, was identified. It was assigned as po with $\delta = 0.80.^{79}$ It was suggested that the quantum defect was larger than is typical for a $p\sigma$ series due to penetration of the p Rydberg orbitals into the H-C-N bonding orbitals.

For CH_3CN , Fridth reported three series, all corresponding to excitation of the nitrogen lone pair and converging to the second ionization potential, and four series corresponding to excitation from the $C \equiv N \pi$ -bond and converging to the first

ionization potential. The upper series were assigned as p_\sigma (\delta=0.97), p_\pi (\sigma=0.60), and d_\sigma (\delta=0.23); the lower series as s_\sigma (\delta=0.97), p_\sigma (\delta=0.76), p_\pi (\delta=0.61) and d_\sigma (\delta=0.23). \frac{72}{2}

Two points need to be made. First, a very important observation in the spectroscopy of Rydberg states is that members of the same types of series, converging to different states of an ion, have very nearly the same term values. 33 (A term value is the difference between the series limit and the energy of the transition to the Rydberg state, i.e., $R/(n-\delta)^2$ in equation II-4). Thus, a po series converging to the first excited state of an ion should have nearly the same quantum defect as a po series converging to the ground ionic state, and likewise for other series. The implication is that the molecular orbital from which the electron is excited has very little effect on the energy of the Rydberg orbital; 33 this is a reasonable conclusion when one considers the large spatial extent of the Rydberg orbitals.

Second, when the EIEL data for CH₃CN are compared to the photoionization energies (as in Table IV-3), it is noted that the EIEL values are systematically lower than corresponding photoionization values by an average of 10 meV. Considering that the photoionization data were taken with higher resolution and, most importantly, were calibrated with several atomic emission lines in the lamp output, the error most likely lies in the EIEL data. This type of systematic error is common for electron spectrometers due to changes in contact potentials, caused by contamination of electrodes in the spectrometer. ^{21,22}

Although this error is small, it has a significant effect on the quantum defects calculated for series members with large However, for series members with small n, the EIEL quantum defects should approach the photoionization values. example, from the Rydberg equation and an assumed IP of 13.00 eV, for n=8 a transition energy of 12.758 eV gives δ =0.500, while transition energy of 12.748 eV gives $\delta=0.652$. For n=4, a transition energy of 11.889 eV yields δ =0.500 whereas 11.879 eV gives $\delta = 0.516$. The quantum defects calculated from Fridth's data continue to differ from the photoionization values as n decreases. It appears that some of the lower members of Fridth's po series may have been assigned incorrectly. This is further exemplified by the limit calculated from the data in reference 72, which agrees very well with the photoionization limit, yet should be about 10 meV lower.

The above ideas are represented schematically in Figure IV-7. Figure IV-7a depicts the transition energies from the ground state nitrogen lone pair orbital to Rydberg orbitals as measured and assigned by Fridth. Also included are $\pi + \pi$ transitions assigned in that work. In Figure IV-7b are hypothetical transition energies to Rydberg states converging to the second ionization limit, calculated from the quantum defects reported in reference 72 for series converging to the first ionization potential of CH₃CN. The photoionization data are shown in Figure IV-7c; the dotted lines were calculated from the photoionization quantum defects.

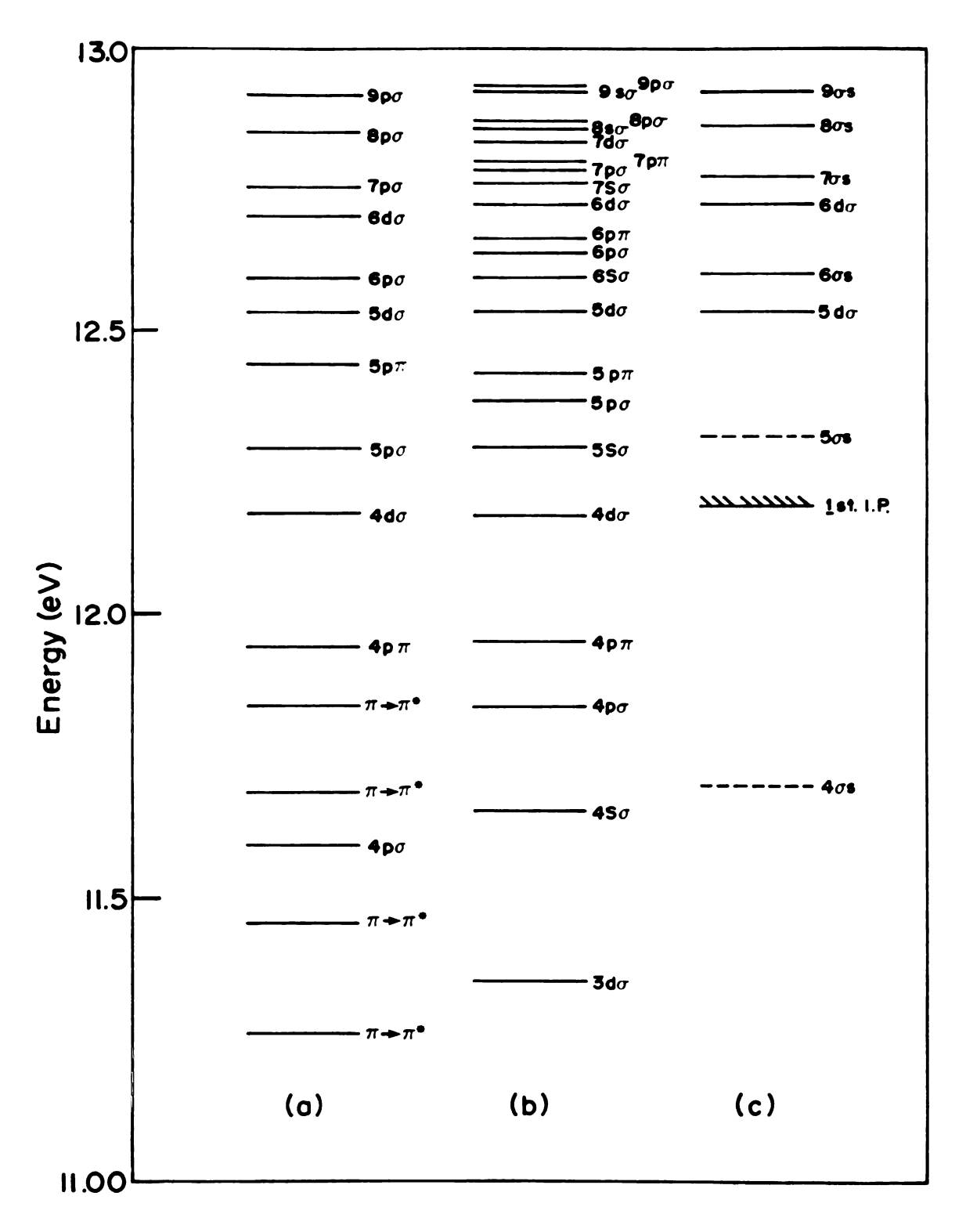


Figure IV-7. Transition Energy Diagram for Excitation from the 5a₁ Orbital of CH₃CN. (a) EIEL transition energies from Reference 72; (b) Hypothetical Rydberg transitions calculated from the quantum defects of Reference 72 for series converging to the ground state of the ion; (c) Photoionization data of this work.

From Figure IV-7a and IV-7b it is easily seen that Fridth's $p\sigma$ series converging to the second ionization potential is inconsistent with the series converging to the first ionization potential. The small discrepancy between the calculated series and the photoionization series is not unreasonable (see reference 33). Moreover, it seems that the highest energy transition labeled $\pi-\pi^*$ by Fridth would be better assigned as $4p\sigma$, and the third $\pi-\pi^*$ component is more likely $4s\sigma$. These changes would make the EIEL results self-consistent as well as consistent with the photoionization results. The series with $\delta=0.92$ is therefore assigned as $s\sigma$. Figures IV-5 and IV-6 and Table IV-3 have been labeled accordingly.

3. Autoionization: 900-800 Å

PIE curves for CH₃CN⁺ and CD₃CN⁺ from 800 to 900 Å are shown in Figure IV-8. The structure in CH₃CN⁺, which as noted earlier is weak, but prominent, would appear to be autoionization; yet the CD₃CN⁺ PIE in this region is smooth and structureless. No optical or EIEL spectra have been published of this region with which to compare the photoionization data. In general, one would not expect so much difference between a protonated compound and its deuterated analog. If autoionization structure is observed in one, it should also be observed in the other, although any vibrational structure may be different. This leads one to wonder if the structure in the CH₃CN⁺ PIE curve is an artifact. The PIEs in Figure IV-8 are reproducible and therefore it is unlikely that a difference of this type is an instrumental artifact; the

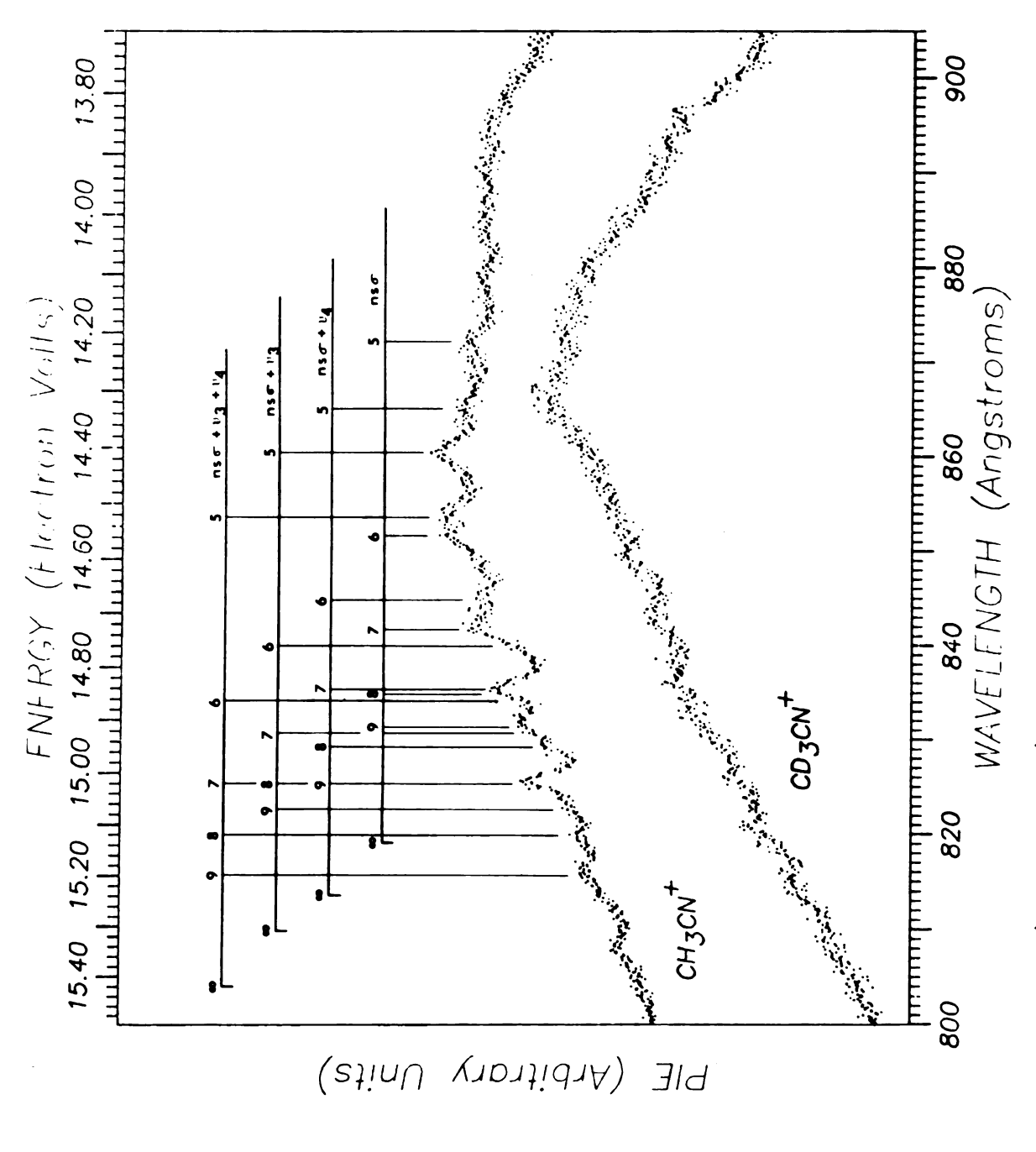


Figure IV-8. CH_3CN^{\dagger} and CD_3CN^{\dagger} PIE Curves: 800-900 Å.

only parameter which is different for the two PIE's is the mass setting.

The m/e of CH₃CN⁺ is 41; the most intense or second most intense peak in the mass spectra of many longer-chain aliphatic nitriles falls at m/e=41. ⁷¹ However, the possibility that the structure in the m/e=41 PIE is caused by another aliphatic nitrile is unlikely for three reasons. First, there is no evidence in the mass spectrum of the acetonitrile used in this investigation of longer chain aliphatic nitriles. Second, it is unlikely that a longer chain aliphatic nitrile would introduce autoionization structure which is so sharp as the observed structure. The photoelectron spectra of longer chain nitriles 81 show only broad and featureless bands for states to which Rydberg series in this region would converge. Rydberg states, being very similar in structure to the ionic states to which they converge, 33 would exhibit autoionization which is also broad and featureless. Third, the same autoionization structure is also observed in the $\mathrm{CH_2CN}^+$ fragment PIE at m/e=40. Other aliphatic nitriles also have a fragment at m/e=40, but its intensity is so low $(3-5\% \text{ of } m/e=41)^{71}$ that it could not account for the structure in the CH2CN+ PIE. (Consistent with the observations for the deuterated parent, this autoionization is also absent in the PIE curve for CD₂CN⁺.)

Another possible source of the structure in the 800-900 Å range is reaction with, or Penning ionization by, excited argon. This would have to arise from argon in the background air. This might seem to be a very remote possibility, but

(1) much of the structure corresponds with optically populatable argon states; 82 (2) with a background air pressure of 10^{-5} torr, 10^{7} argon atoms are in the light beam at any one time (argon is 0.033% of air) and the structure represents variations of only about 30 ion counts/s on a background of about 1500 counts/s; and (3) Ar $^{+}$ is known to react with molecular hydrogen to produce ArH $^{+}$ (m/e=41). 83 Interference from ArH $^{+}$ was also considered in the ion cyclotron resonance ion-molecule reaction study of acetonitrile by Gray. 62

There are three reactions that could account for ions at m/e=40 and 41:

- (1) $Ar* + CH_3CN \rightarrow ArH^+ + CH_2CN$
- (2) Ar* + $CH_3CN \rightarrow Ar + CH_3CN^+$
- (3) $Ar* + CH_3CN \rightarrow Ar + CH_2CN^+ + H.$

the ionization potential of argon. Reaction (1) alone would not account for structure in the $\mathrm{CH_2CN}^+$ PIE, and reactions (2) and (3) should be just as probable for the deuterated compound as for the protonated compound. Thus, argon would not seem to be the cause of the structure. However, to be absolutely sure, the PIE at m/e=41 was measured for a 1:5 argon: acetonitrile mixture. The argon pressure was 1.0×10^{-4} torr, a 3×10^4 fold increase over the highest possible background pressure. There were no significant changes in the $\mathrm{CH_3CN}^+$ PIE. The structure in question can thus be assigned to autoionization from Rydberg series converging to the second excited state of the acetonitrile parent ion.

Rydberg Series Converging to the Second Excited State of CH3CN+. Table IV-4.

vibrational state ^a	grou	nd	104	4	1^{v_3}	æ	1^{ν_3} , 1^{ν_4}	ر 4
Expe	Experimental	Energies	Energies (eV) and &	9				
u	Energy	જ	Energy	\$	Energy	8	Energy	છ
ß	14.218	1.14	14.331	1.11	14.416	1.08	14.524	1.08
9	14.569	1.08	14.674	1.05	14.758	66.0	14.862	1.02
7	14.723	1.22	14.848	1.03	14.921	1.01	15.019	1.10
œ	14.850	1.03	14.946	1.08	15.019	1.04	15.120	1.15
6	14.921	0.93	15.019	0.97	15.083	1.08	15.192	1.10
average $\delta = 1.07$								

From Turner's 55 ionization potential and vibrational assignments for the second excited state of $\mathrm{CH_3CN}^+$, four series converging to four different vibrational states can be identified. The series are shown in Figure IV-8 on the bars near the top of the figure and are listed in Table IV-4. From the quantum defects the series is assigned as an $\mathrm{s}\sigma$ type.

The same Rydberg states are expected to autoionize in CD_3CN ; however if the vibrational frequencies are sufficiently closer in CD_3CN the autoionization structure may be so overlapped that the series are unidentifiable. Indeed the vibrational structure of the second excited state in the photoelectron spectrum of CD_3CN is much less distinct and more overlapped than in CH_3CN ; 66 the same should be expected of the Rydberg series converging to this state.

4. The Threshold Region: 1000-1040 \mathring{A}

In order to precisely determine the adiabatic ionization potentials, and to resolve as much structure as possible, PIEs of the parent ions in the threshold region were acquired with a monochromator bandpass of 0.42 Å (5 meV at 1010 Å); they are presented in Figure IV-9. Recall from Chapter II that in the absence of autoionization a PIE would be a series of steps, each step being the threshold for a transition to a new state of the ion. The threshold region of ${\rm CH_3CN}^+$, for which there are two well defined steps at 1016 and 1012 Å, demonstrates this nicely. Judging from the high intensity and location of the first peak of the photoelectron spectrum

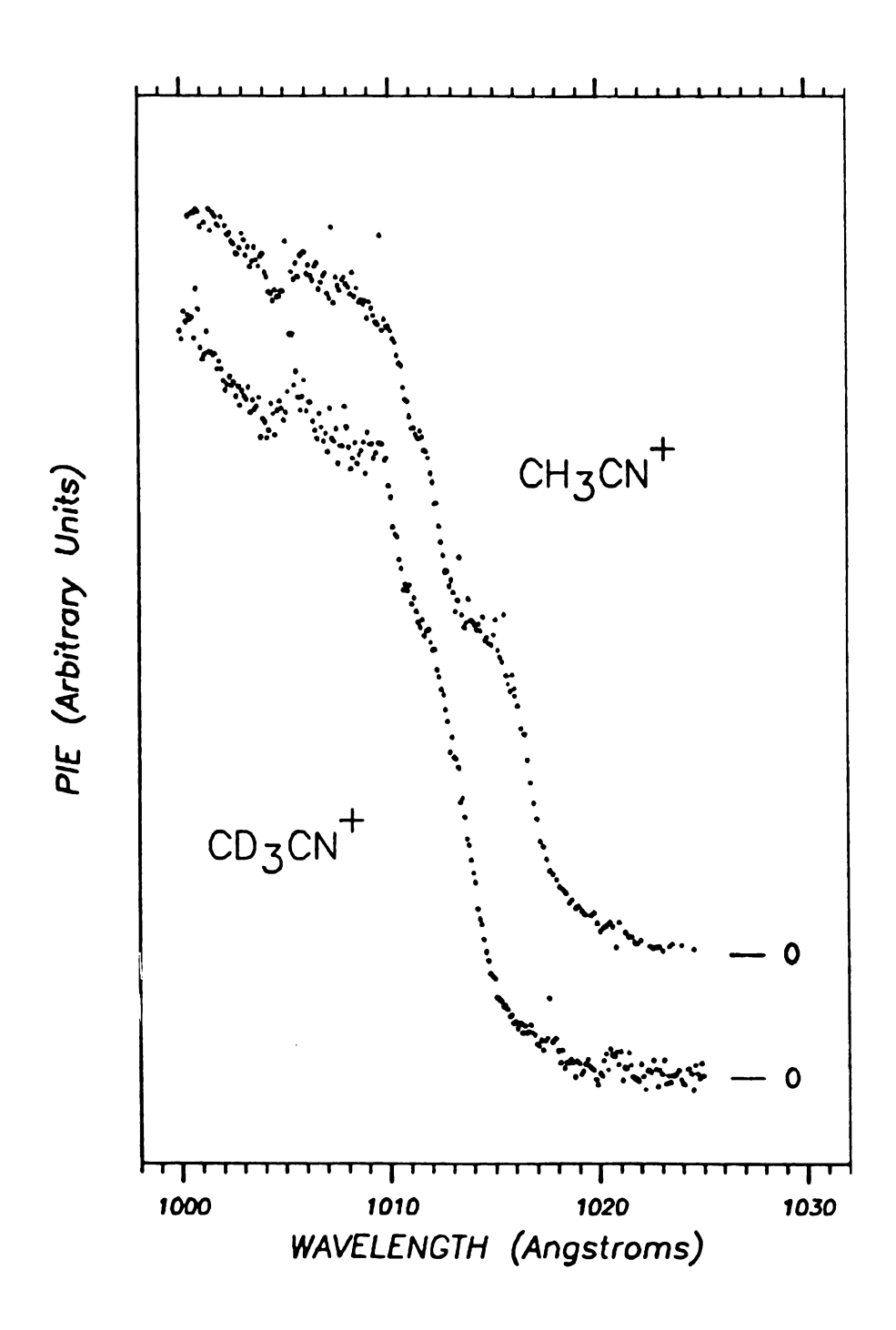


Figure IV-9. CH_3CN^+ and CD_3CN^+ PIE Curves: 1000-1040 Å.

		,
		;
		•

of CH₃CN, there is little doubt that the first step is the threshold for the transition to the ground vibrational state of the ground electronic state of the ion (the adiabatic ionization potential). The second step must be a vibronic transition to an excited vibrational state of the ion, and is a transition which has not been resolved from the 0+0 transition in the photoelectron spectrum. It is only because Rydberg states converging to excited vibrational states of the ion are strongly predissociated that these steps are so distinct. The third very small step at 1010 Å is in all probability due to autoionization, as will be discussed below.

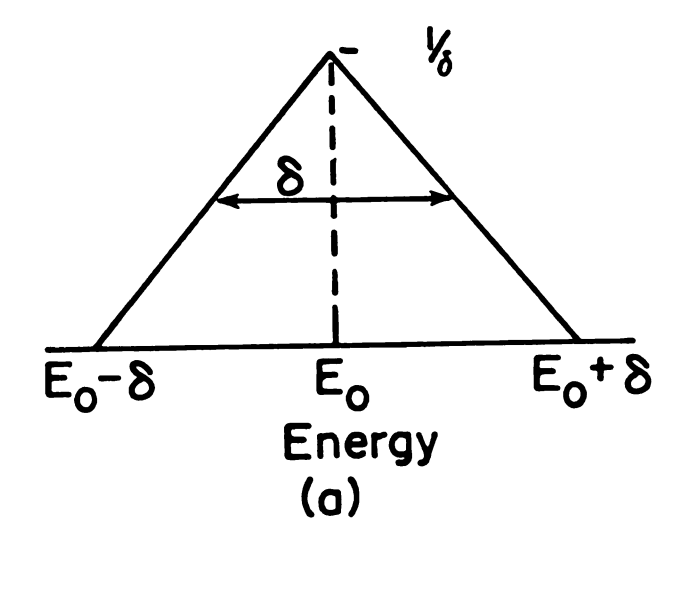
The $\mathrm{CD_3CN}^+$ PIE in this region is significantly different from that of $\mathrm{CH_3CN}^+$. There is only one poorly defined step at 1012 Å, followed by an increase in intensity which, like the third step in the $\mathrm{CH_3CN}^+$ PIE, can be attributed to autoionization. Close examination shows also that the initial step in the $\mathrm{CD_3CN}^+$ PIE is at a slightly shorter wavelength than the corresponding rise in the $\mathrm{CH_3CN}^+$ PIE. It appears that the first ionization potential of $\mathrm{CD_3CN}$ is higher than that of $\mathrm{CH_3CN}$. Indeed, one photoelectron study 67 has reported a difference in the first ionization potential of $\mathrm{CH_3CN}$ and $\mathrm{CD_3CN}$, in the same direction indicated by this work.

The adiabatic ionization potential is unambiguously defined as the difference in energy between the neutral molecule in its electronic, vibrational and rotational ground state and the ion in the lowest vibrational and rotational level of a particular electronic state. Since it is certain, by

comparison with the photoelectron spectrum, that the initial step of the acetonitrile PIE is the transition from the ground vibrational state of the neutral to the ground vibrational state of the ion, the problem remains to determine the location of the rotationless transition on the step. This requires an approximation since the resolution of the instrument is far from sufficient to resolve rotational structure. The 5 meV bandpass is equivalent to 40 cm⁻¹. Before discussing the rotational structure of the steps, the effect of the instrument function should be considered.

The effects of the instrument function have been discussed in the literature, 84 and the results are presented in Figure IV-10. A step function is assumed for the photoionization cross section for a single transition from the neutral to the ion and is convolved with a triangular slit function, which has been shown to be a good approximation. 85 The result is a sigmoidal curve whose inflection point is at the true threshold and for which a line drawn tangent to the inflection point intercepts the energy axis at $\delta/2$ (δ is the slit width) below the true threshold. Application of this result to the threshold PIEs shows that the slit width accounts for about half the breadth of the rise of the steps. The remainder, then must be due to the rotational envelope within the vibronic transition.

The rotational structure within a vibronic photoionization transition has not been well characterized experimentally or theoretically. In only a very few cases has some rotational



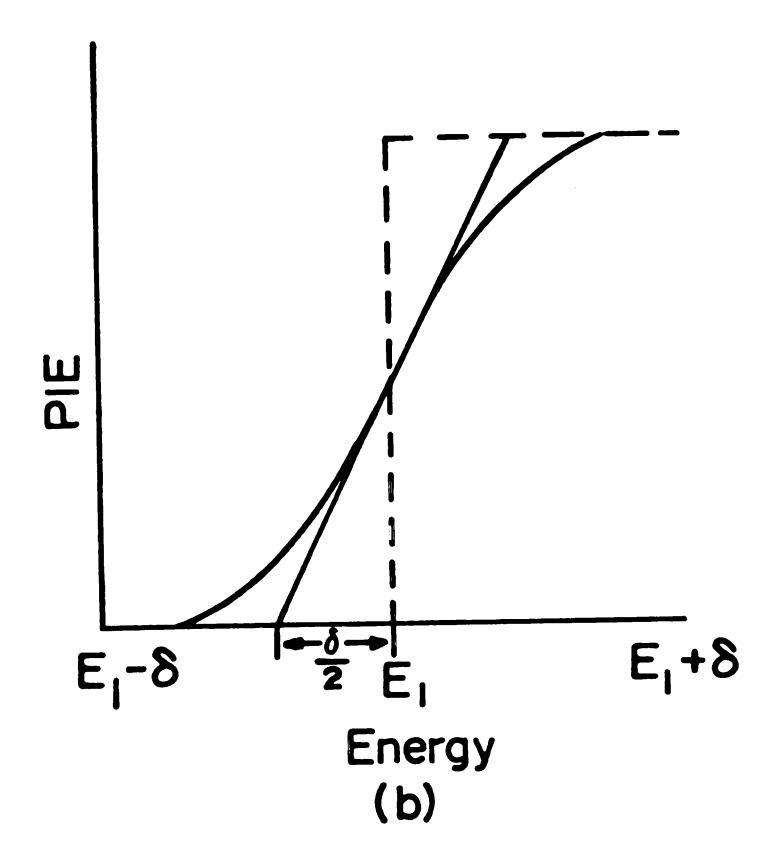


Figure IV-10. The Effects of a Triangular-Slit Function on a Step Function. (a) Triangular-Slit Function; (b) Triangular-Slit Function convoluted with a Step Function.

structure been experimentally resolved (the photoelectron spectra of H₂, ⁸⁶ HF and DF⁸⁷), and the theoretical derivation of the applicable selection rules is complicated by coupling of the ejected electron's angular momentum, which can take on several values, with the total angular momentum of the ion. ²² However, the selection rules for bent AB₂-type molecules have been worked out, ²² and it is clear that rotational transitions in P, Q and R branches are allowed. It is likely that at least P- and R-branch, and perhaps even Q-branch, transitions will be allowed in acetonitrile.

Because the PIEs were measured at room temperature, the thermal distribution of populated rotational states of the neutral molecule is available for ionization. Therefore a photoionizing vibronic transition will be accompanied by a rotational envelope. An approximation is needed for the transition probabilities within the rotational envelope which includes the thermal distribution of rotational states of the neutral. The transition probability then can be convolved with the slit function and a step function to obtain a model PIE which could be used to fit the experimental data in order to arrive at an accurate ionization potential.

The model chosen to approximate the transition probability within the rotational envelope, convoluted with the slit function was a Gaussian distribution centered at the ionization potential. The choice of a Gaussian distribution is easily checked by fitting the data, and it will be shown that

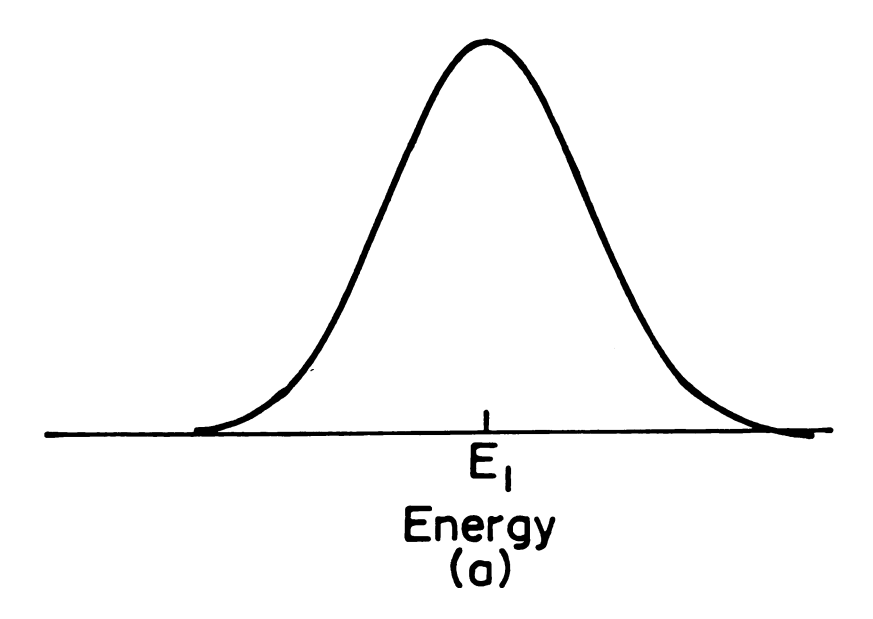
it is a good approximation to the transition probability. The assumption that the rotationless transition is at the center of the rotational envelope is somewhat less certain. However, a survey of ordinary absorption spectra²⁴ supports this assumption within the limits of resolution of these experiments. Moreover, this is the same assumption that is used in photoelectron spectroscopy, where the maximum of the lowest energy vibronic peak of an electronic band is assigned as the ionization potential.

For a Gaussian transition probability within the rotational envelope, the PIE (E_p) , the photoionization efficiency at photon energy E_p , is calculated by integrating the Gaussian from -0 to E

PIE
$$(E_p) = a \int_{0}^{E_p} e^{-b(E-IP)^2} dE$$
, (IV-1)

where E is the excitation energy above the ground state of the neutral, IP is the ionization potential, b determines the width of the step and a represents the height of the step. An example of this model is given in Figure IV-11; the ionization potential is at the inflection point on the rise of the step.

To test this model and to locate the inflection points as accurately as possible, the thresholds were fit by means of KINFIT 4 74 with a, b, and IP chosen as adjustable parameters. The results of the fits, which demonstrate that a Gaussian is indeed a reasonable approximation, are presented in Figure IV-12. For CH_3CN^+ the second step was also included in the fit by integrating the sum of two Gaussians, one for each step,



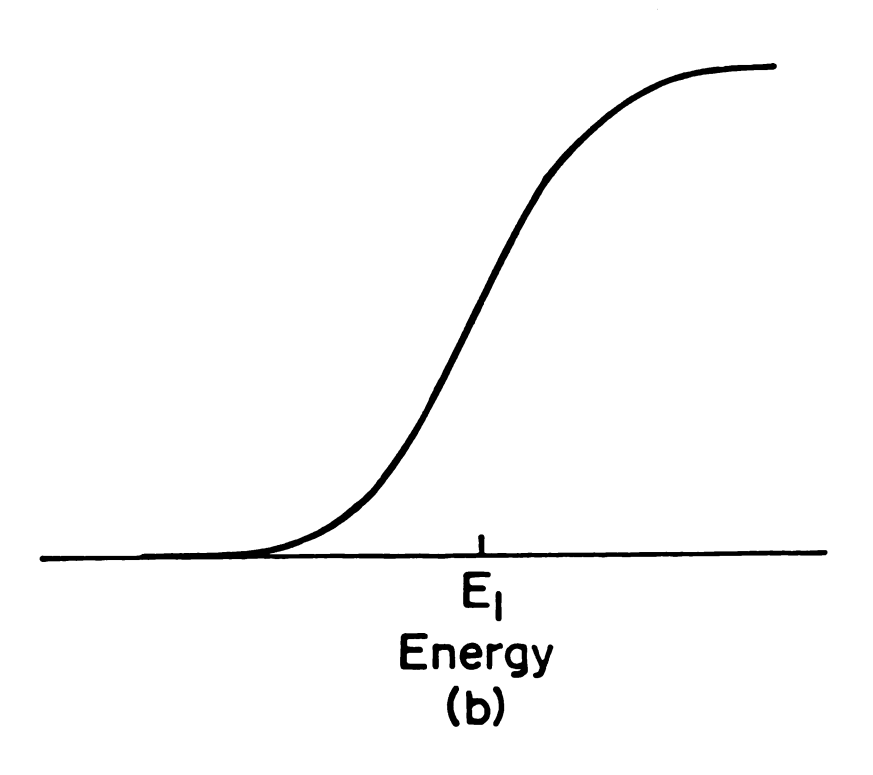


Figure IV-11. Integration of a Gaussian Transition Probability. (a) Gaussian function; (b) The integrated Gaussian function.

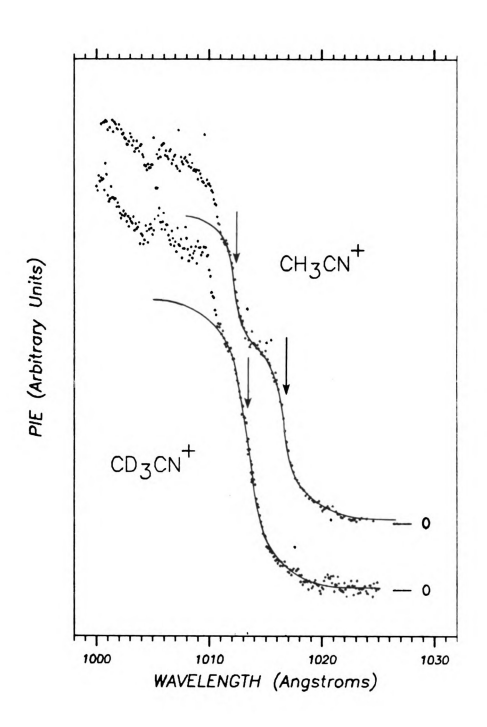


Figure IV-12. The Fit of the ${\rm CH_3CN}^+$ and ${\rm CD_3CN}^+$ Thresholds.

with different parameters a, b, and IP. In this way the fundamental vibrational frequency of the excited vibrations can be obtained.

The ionization potentials arising from the fits are indicated with arrows in Figure IV-12, and are listed and compared with values reported by other investigators in Table IV-5. In general the agreement is good, but merits some comment. For CH₃CN note that all the values, except those of references 65 and 66, are higher than the ionization potential determined in this work. Probably the reason is that the vibronic transition corresponding to the second step of the PIE was not resolved, which would cause one to arrive at a higher ionization potential. This is definitely the case for the photoelectron results for which spectra were published, and although neither instrumental resolution nor PIE curves were reported, this was probably the case with the previous photoionization results too, judging from other publications of the investigators. The ionization potential of reference 66 is obviously too low.

The limits of error reported for this work are realistic.

The PIE curves can be calibrated to better than ± 0.1 Å with atomic emission lines in the light source output, and differences in the ionization potential of ± 0.3 Å were clearly discernible in the quality of the fit. The propagated sum of these two errors is ± 3.6 meV at the ionization potential.

The error limits reported in Table IV-5, ± 5 meV, reflect the uncertainty that the ionization potential is at the center of

Table IV-5. First Ionization Potentials of CH_3CN and CD_3CN .

	Reported Value (eV)	Method ^a	Reference
CH ₃ CN	12.194 ± 0.005	PIMS	This work
	12.19 ± 0.01	PIMS	65
	12.205 ± 0.004	PI	64
	12.22 ± 0.01	PI	63
	12.20 ± 0.01	PE	67
	12.21	PE	55
	12.12	PE	66
CD ₃ CN	12.235 ± 0.005	PIMS	This work
	12.23 ± 0.01	PE	67

^aPIMS - Photoionization mass spectrometry; PI - Photoionization without mass analyses; PE - Photoelectron spectroscopy.

the Gaussian transition probability assumed for the fit.

The ionization potential of CD₃CN is indeed higher than the ionization potential of CH₃CN by approximately 41 meV. This difference agrees with the results of reference 67, the only published ionization potential of CD₃CN, and is further substantiated by a shift to higher energy in CD₃CN (compared to CH₃CN) of Rydberg series converging to the ground state of the ion. This isotope shift must be the result of a difference in the difference of zero-point energies between the neutral and the ion in the two molecules.

The second step in the ${\rm CH_3CN}^+$ PIE is 53 meV (427 cm⁻¹) above the ground vibrational state of the ion. From a comparison of this energy difference to the vibrational frequencies of the neutral molecule, the most likely assignment for the step is the transition from the ground vibrational state of the neutral to the vibrational state of the ion with a single quantum of excitation in the CCN bend (v_8) . The vibration v_8 has a fundamental frequency of 362 cm⁻¹ in the neutral and is the lowest frequency normal mode in acetonitrile. The only other remotely possible assignment would be the transition to v=1 of the next lowest frequency vibrational mode of the ion, the CC stretch (v_4) , for which the frequency in the neutral is 920 cm⁻¹.88 It is extremely unlikely that the CC stretching frequency in the ground electronic state of the ion would be less than half that in the neutral molecule.²²

The ratio v_8 (CH₃CN): v_8 (CD₃CN) in the neutral molecule is

1.094, and from this ratio one would predict $v_{\rm R}$ in ${\rm CD_3CN}^+$ to be approximately 390 cm^{-1} (48 meV). This would put the midpoint of a step in the CD3CN+ PIE for the threshold for a single excitation of ν_{8} at 1009.4 Å. However, the midpoint of the second step in the CD_3CN^+ PIE curve is at 1010.3 Å, the same wavelength as the third step in the CH3CN+ PIE. If the second step in the ${\rm CD_3CN}^+$ PIE is the vibronic threshold for the single excitation of $\boldsymbol{\nu}_{8}$ it would require the frequency of $v_{\rm R}$ in ${\rm CD_3CN}^+$ to be 295 cm⁻¹, which is much smaller than the predicted value. The autoionization in this region is from Rydberg states converging to the first excited state of the ion and is not isotope dependent. Because the second step in the CD3CN PIE is at the same wavelength as the third step in the CH3CN PIE, and because assigning it as the vibronic threshold for the single excitation of ν_{o} would require an unreasonably low frequency for v_8 in CD_3CN^+ , the second step in the CD₃CN⁺ PIE and the third in the CH₃CN⁺ PIE are most reasonably attributed to autoionization. The vibronic threshold for the single excitation of v_8 in CD_3CN^+ is most likely hidden under the autoionization as a consequence of CD₃CN's higher ionization potential.

The transition in ${\rm CH_3CN}^+$ to the first excited level of v_8 , the CCN bend, has important consequences for the structure of the ground electronic state of the ion. In general, photo-ionization transitions are adequately described by the Frank-Condon principle. The Franck-Condon principle assumes that the electronic and nuclear motions of a molecule are not

coupled, and therefore a transition probability can be resolved into electronic, vibrational and rotational factors. The intensity of a vibrational band in an electronically allowed transition is then proportional to the vibrational factor, commonly called the Franck-Condon factor, $|\langle \psi_{\mathbf{v}}^{"}|\psi_{\mathbf{v}}^{'}\rangle|^2$, where $\psi_{\mathbf{v}}^{"}$ and $\psi_{\mathbf{v}}^{'}$ are the vibrational wavefunctions of the lower and upper states respectively. For the Franck-Condon factor to be non-zero the product $(\psi_{\mathbf{v}}^{"}\psi_{\mathbf{v}}^{'})$ must be symmetric with respect to all symmetry operations common to the final and initial electronic states; that is, $\Gamma(\psi_{\mathbf{v}}^{"}) \times \Gamma(\psi_{\mathbf{v}}^{'}) = \Gamma$ (totally symmetric).

 ${
m CH_3CN}$ belongs to the ${
m C_{3v}}$ point group; ⁸⁸ its photoelectron spectrum ^{55,56,57} as well as the Walsh diagram of ${
m CH_3XZ}$ type molecules ⁸⁹ predict that the ground electronic state of ${
m CH_3CN}^+$ is also ${
m C_{3v}}$. The CCN bend is an "e" vibration ⁸⁸ and therefore the first excited vibrational level (v=1) belongs to the E representation. The ground vibrational level (v=0), as always, belongs to the totally symmetric representation ${
m A_1}$. The product E × ${
m A_1}$ = E and the vibronic transition from the ground vibrational level of the neutral to the first excited vibrational level of ${
m v_8}$ in the ion is not allowed within the assumptions of the Franck-Condon principle. It appears that the Franck-Condon principle is not a good approximation for transitions to the ground state of ${
m CH_3CN}^+$

However, this is not completely surprising. The ground electronic state of ${\rm CH_3CN}^+$, which results from the removal of

a π electron from the C=N bond, is orbitally doubly degenerate (a 2E state) and is therefore subject to Jahn-Teller distortion. The Jahn-Teller theorem states that if a non-linear molecule (not $C_{\infty}v$) has an orbitally degenerate electronic state when the nuclei are in a symmetrical configuration, then the molecule is unstable with respect to at least one asymmetric displacement of the nuclei that may lift the orbital degeneracy. ²² In other words, there can be a coupling of the electronic motion with at least one of the non-totally symmetric vibrations such that the vibronic levels which were degenerate by way of the orbital degeneracy are split. ²⁴

The "E" vibrations of an E electronic state of the C_{3v} molecule are Jahn-Teller active. 21 , 22 , 24 That is, they may interact with an E electronic state to split its degeneracy. If vibronic coupling of v_8 with the 2 E state of CH_3CN^+ is invoked, the transition in question is allowed. To demonstrate this the vibronic wavefunction ψ_{ev} and the dipole transition moment M_{ev} must be used. 24 The probability of a vibronic transition is given by $|M_{ev}|^2 = |\langle \psi_{ev}^{"}|\hat{\mu}|\psi_{ev}\rangle|^2$, where $\hat{\mu}$ is the dipole moment operator. For a component $|M_{ev}|^2$ to be non-zero $\Gamma(\psi_{ev}^{"}) \times \Gamma(\psi_{ev}^{"})$ must belong to the same species as a component of $\hat{\mu}$. The initial state vibronic wavefunction $\psi_{ev}^{"}$ (the ground vibrational level of the ground electronic state of the neutral) belongs to the A_1 representation. The species of the final state are found by the product $\Gamma(\psi_{ev}^{"}) \times \Gamma(\psi_{v}^{"})^{24}$ which is E×E, and three vibronic levels result:

 A_1 , A_2 and E. The product $\Gamma(\psi_{\text{ev}}^{"}) \times \Gamma(\psi_{\text{ev}}^{"})$ is then $(A_1 + A_2 + E) \times A_1 = A_1 + A_2 + E$. The z component of $\hat{\mu}$ belongs to the A_1 representation and the transition to the A_1 vibronic level is allowed by $\hat{\mu}_z$. The x and y components of $\hat{\mu}$ belong to the E representation so that the transition to the E vibronic level is also allowed.

The magnitude of the energy splitting of the vibronic levels is impossible to determine from the PIE curve, since only one step for the transition to the $\boldsymbol{\nu_{8}}$ vibronic levels is evidenced in the PIE curve. It is possible that the splitting is not resolved. However, it could also be that only one of the two allowed transitions has sufficient intensity to be observed. The completely analogous situation exists in the high resolution photoelectron spectrum of HCN. 78 The photoelectron band of the ground electronic state of \mbox{HCN}^+ , which corresponds to the removal of a $C\equiv N$ π electron, has a vibrational component assigned to the single excitation of ν_2 , the HCN bending vibration. The ground electronic state of HCN+ is doubly degenerate (a π state), as is v_2 . Thus transitions to the first excited level of ν_2 in a π electronic state of the ion are allowed only if there is vibronic interaction 22,78 (the Renner-Teller effect in the case of linear molecules). When vibronic interactions are considered, transitions to two vibronic levels of v_2 are allowed. However, only a single transition is resolved.

By analogy with HCN it is reasonable to assign the second step in the ${\rm CH_3CN}^+$ PIE curve as a transition to a vibronic

level of the singly-excited CCN bend. It should be noted that the above arguments apply equally well to ${\rm CD_3CN}^+$. The DCN bending vibration has also been observed in the photoelectron spectrum of DCN, ⁷⁸ thus supporting the contentions that the analogous transition in CD₃CN is obscured by autoionization.

There are several other possible vibronic transitions to the ground electronic state of the ion as is demonstrated by the photoelectron spectrum (Figure IV-1). There is the hint of a step at ~994 Å in the $\mathrm{CH_3CN}^+$ PIE curve (~993 Å in the $\mathrm{CD_3CN}^+$ PIE curve; see Figures IV-5 and IV-6) and by comparison with the photoelectron spectrum this feature probably corresponds to a single excitation of the CN stretch (ν_2). ν_2 is an $\mathrm{A_1}$ mode and the transition to ν_2 is allowed by the selection rules imposed by the Franck-Condon principle. Although all the vibronic transitions observed in the photoelectron spectrum will contribute to the PIE curves, the tresholds are hidden by autoionization structure.

E. Fragment Ion PIEs

Fragment ion PIEs are most often smooth and featureless and reveal little information about the structure of the parent ions or the fragments. The most important piece of information to be gleaned from a fragment ion PIE is the appearance potential (AP). Ideally, one would like to determine the O°K AP - the energy of the transition from the ground rotational vibrational and electronic state of the neutral to the state of the parent ion from which fragments are produced in their

ground rotational, vibrational and electronic states with no kinetic energy. This is the 0°K thermochemical threshold for the fragmentation. However, as discussed in Chapter II the observation of fragmentation at the true thermochemical threshold depends on the formation of parent ions with the necessary internal energy, which dissociate sufficiently rapidly that a detectable number of ions are produced.

Another complicating factor is the thermal distribution of populated rotational and vibrational states of the neutral. Neutral molecules in excited rotational and vibrational states will be available for fragmentation at lower photon energies than molecules in the ground rotational and vibrational state. Experimentally, the most obvious effect of the thermal energy is to introduce a low intensity, slowly-rising onset -- a "thermal tail" -- to the fragment ion PIEs. If one scans from high to lower photon energy, the "thermal tail" approaches the base line asymptotically, and if the data are acquired with a sufficiently sensitive instrument, the tails will continue for several hundred millielectron volts below the thermochemical threshold.

The effects of thermal energy of the neutral has been considered in the literature and suitable corrections have been devised. Guyon and Berkowitz, 84 have shown that the internal thermal energy of the neutral shifts the fragment ion PIE curves to lower energy by an amount equal to the average thermal energy of the neutral.

In essence the thermal energy E_T of the neutral adds to the photon energy with an intensity proportional to the number of neutral molecules at E_T . When the fragmentation rate is not kinetically limited, the fragment PIE curves are often linear above threshold. In this case, the experimental AP is found by extrapolating the linear region of the curve to the base line. The 0° AP is then calculated by adding the average thermal energy of the neutral to the experimental AP. It has also been shown that in this case the departure from linearity at the foot of the PIE occurs at the 0° K AP. 49,84 This is important because it serves as a check for the value found by adding the thermal energy.

When fragmentation is kinetically limited, the tail is more prominent and often extends to lower energies with more intensity than can be accounted for by the thermal energy of the neutrals. In this case, the tail is due to both the thermal energy of the neutral and a slowly increasing fragmentation rate. The onsets are gradual and the threshold regions are often curved. The best way to determine the AP is to extrapolate the upper regions of the PIE curves. This method will yield an AP which is greater than the thermochemical threshold and should be considered only as an upper limit. 14

Early PIMS investigators often assigned the AP as the lowest energy at which a fragment could be detected, i.e. somewhere on the low energy tail. This procedure is obviously incorrect when kinetic effects are not important, 49,84 but it could have some merit when the fragmentation rate is kinetically

limited since it would yield a lower value for the AP than that determined by extrapolation. However, since it is impossible to determine how much of the tail is due to thermal energy of the neutral and since the experimental AP would depend strongly on the sensitivity of the instrument with which the data were taken, this method yields an unreliable result. The experimental AP could be to higher or very much lower energy than the thermochemical threshold; the extrapolated value is preferred.

In the following sections the acetonitrile fragment ion PIE curves are presented and discussed. The experimental AP's are summarized in Table IV-8 at the end of this chapter. The heats of formation of several neutral species will be useful for the following discussion. These are listed in Table IV-6 along with several unit conversion factors.

1. CH_2CN^+, CD_2CN^+

The lowest energy fragmentation process in acetonitrile is loss of a hydrogen atom (deuterium atom) to produce $\mathrm{CH_2CN}^+$ ($\mathrm{CD_2CN}^+$). The PIE curves of $\mathrm{CH_2CN}^+$ and $\mathrm{CD_2CN}^+$ are shown in Figure IV-13. As previously mentioned, the thresholds for production of these ions (-880 Å) are in a blank region of the photoelectron spectrum. Therefore in the region from threshold up to about 820 Å, where the second excited state of the parent ion becomes available, the fragmentation is from states of the parent ions populated by autoionization. Some autoionization-like structure, which correlates well with autoionization structure in the $\mathrm{CH_3CN}^+$ PIE curve, is readily

Table IV-6. Heats of Formation of some Neutral Species and some Useful Conversion Factors. a

	ΔH _{fo} (kJ/mole)	^{ΔH} f298 ^(kJ/mole)
CH ₃ CN	94.5	87.4
HCN	135.5	135.1
СН	592.5	595.8
CN	431.8	435.1
Н	216.0	218.0
CD ₃ CN	82.4	
DCN	132.5	
CD	591.7	
D	219.8	221.7
	_1	

 $^{1 \}text{ eV} \equiv 8066 \text{ cm}^{-1}$

¹ eV/molecule = 96.49 kJ/mole

l kcal/mole = 4.184 kJ/mole

^aFrom reference 91 except ΔH_{fO} of CD₃CN, DCN and CD, which were estimated from ΔH_{fO} of the protonated analogs by assuming that differences were due to differences of zero point energies.

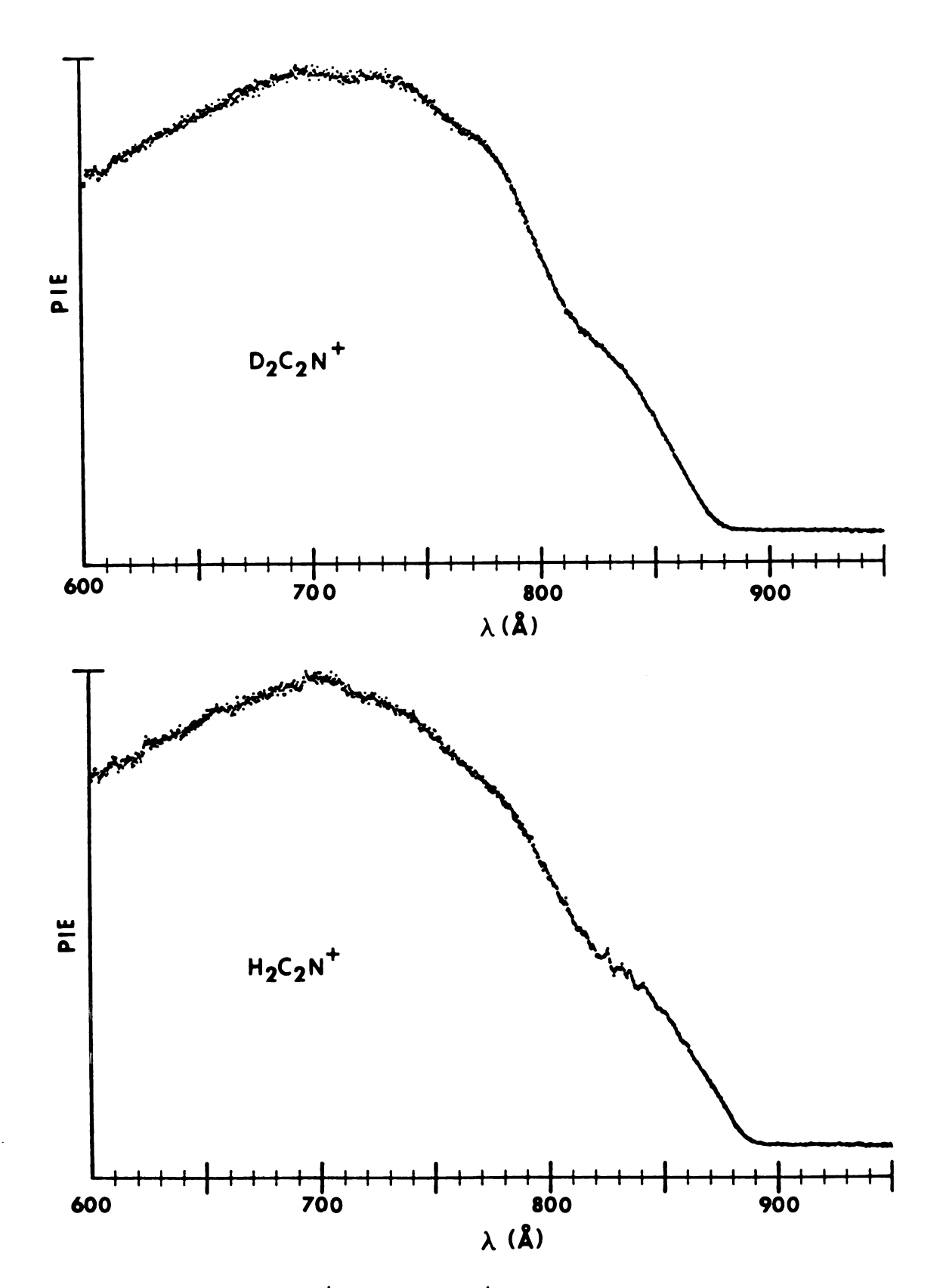


Figure IV-13. CH_2CN^+ and CD_2CN^+ PIE Curves.

		· · · · · · · · · · · · · · · · · · ·
		Ċ
		;
		!
		•

apparent in the $\mathrm{CH_2CN}^+$ PIE curve between 820 - 860 Å. The rise starting at 820 Å and continuing to shorter wavelengths can be attributed to the threshold for the second excited state of the parent ion. The PIEs level off at about 700 Å and decrease at shorter photon wavelengths due to competition with other fragmentation processes.

The APs determined by extrapolating the linear region of the PIE curves between 860 and 880 Å to the base line and subtracting one-half the photon band width are 886.0 ± 0.5 Å $(13.99 \pm 0.01 \text{ eV})$ for CH_2CN^+ and $876.0 \pm 0.5 \text{ Å}$ $(14.15 \pm 0.01 \text{ eV})$ for CD₂CN. The error limits reflect the uncertainty of extrapolating the data to the base line. The AP reported by Dibeler and Liston⁶⁵ for CH_2CN^+ (14.01 ± 0.02 eV), determined by an unspecified procedure, agrees within experimental error with the value found in this work. The AP of ${\rm CD_2CN}^+$ has not been previously determined; however it is reasonable that its value is greater than that of CH2CN+. If the H-atom (D-atom) loss is considered to be a simple extension of a C-H (C-D) bond, both the protonated and the deuterated compounds will dissociate over the same potential surface. Because the zero point energy of a C-D stretch is lower than that of a C-H stretch, in the former case more energy will be required to get over the top of the surface and the AP of the deuterated fragment will be at a higher energy. To quantitatively account for the difference in the APs of the protonated and deuterated fragments, the zero point energies of both the neutral and the ionic transition state would have to be

known in both cases. However, since one can only guess the structure of the transition state, this would require a difficult and uncertain analysis. 48

There are several reasons to believe that the H-atom loss is sufficiently fast that the experimental APs are not significantly affected by the kinetics of the fragmentation.

First, since this is the lowest energy fragmentation it is not in competition with any other fragmentation pathway at the threshold. Competition almost always causes the experimental AP to be shifted to higher energy than the true thermochemical threshold. Second, the PIEs are very linear in the region just above threshold. Fragments whose intensity is kinetically limited usually exhibit PIEs with a slowly rising threshold and with considerable curvature. Third, the small curved section at the foot of the PIEs can be completely accounted for by the internal thermal energy of the neutrals.

The average thermal vibrational energy of neutral ${\rm CH_3CN}$ at $300^{\circ}{\rm K}$ (calculated by using the statistical thermodynamics expression for independent harmonic oscillators 90) is 23 meV/molecule. For ${\rm CD_3CN}$ it is 29 meV/molecule. The average thermal rotational energy (3/2KT) is 39 meV at $300^{\circ}{\rm K}$. When the sum of the vibrational and rotational thermal energy (62 meV for ${\rm CH_3CN}$ and 68 meV for ${\rm CD_3CN}$) is added to the experimental AP of the fragments it puts one at the point of departure from linearity at the foot of the PIEs. This is the predicted result for fragment ion PIEs whose intensity at threshold is not kinetically limited. Thus it can be concluded that the experimental APs accurately reflect the true

the

Add

the

14.

cal

res

iH f

lit

AP :

the in

Wit

hov

Alt

CH.

the

tha to

the

à s

cal

men

thermochemical threshold for the fragmentation process. Addition of the rotational and vibrational thermal energy of the neutral to the experimental APs gives O K APs of 14.05 ± 0.01 eV for CH_2CN^+ and 14.22 ± 0.01 eV for CD_2CN^+ .

From the O°K APs, the O°K heats of formation are easily calculated. The calculations are shown in Table IV-7 and the results are: $\Delta H_{fo} (CH_2CN^+) = 1235 \text{ kJ/mole}$ and $\Delta H_{fo} (CD_2CN^+) = 1234 \text{ kJ/mole}$. There are no currently accepted literature values with which to compare these numbers.

2. CHCN⁺,CDCN⁺

CHCN⁺ and CDCN⁺ are the fragments with the next higher AP; PIE curves are shown in Figure IV-14. The curves are smooth and structureless and there is little to be said about them. The leveling off at about 700 \mathring{A} , followed by a decrease in intensity at shorter wavelengths, is due to competition with other fragmentation processes. An important feature, however, is the curved region at the foot of the PIEs. Although it is not readily apparent in Figure IV-14, the curvature extends over a much wider region than in the CH2CN and CD2CN PIEs, and it cannot be accounted for by the thermal energy of the neutral. This is evidenced by the fact that when the average thermal energy of the neutrals is added - to the experimental AP, the result is significantly lower than the point of the departure of the PIE from linearity. This is a sure sign that the intensity of these fragments is kinetically limited at the thermochemical threshold and the experimental APs will be higher than the true thermochemical threshold.

Table IV-7. Calculation of ΔH_{fo} of CH_2CN^+ and CD_2CN^+ .

$$CH_3CN \rightarrow CH_2CN^+ + H \qquad \Delta Hrxn = AP (CH_2CN^+)$$

 $\Delta H_f (CH_2CN^+) = AP (CH_2CN^+) + \Delta H_f (CH_3CN) - \Delta H_f (H)$
 $AP_{0^0 K} (CH_3CN^+) = 14.05 \text{ eV} \qquad 1356 \text{ kJ/mole}$
 $\Delta H_{fo} (CH_2CN^+) = 1356 + 95 - 216 = 1235 \text{ kJ/mole}$

$$CD_3CN \rightarrow CD_2CN^+ + D$$
 $\Delta Hrxn = AP(CH_2CN^+)$
 $\Delta H_f(CD_2CN^+) = AP(CD_2CN^+) + \Delta H_f(CD_3CN) = \Delta H_f(H)$
 $AP_{0^0K}(CD_2CN^+) = 14.22 \text{ eV}$ 1372 kJ/mole
 $\Delta H_{fo}(CD_2CN^+) = 1372 + 82 - 220 = 1234 \text{ kJ/mole}$

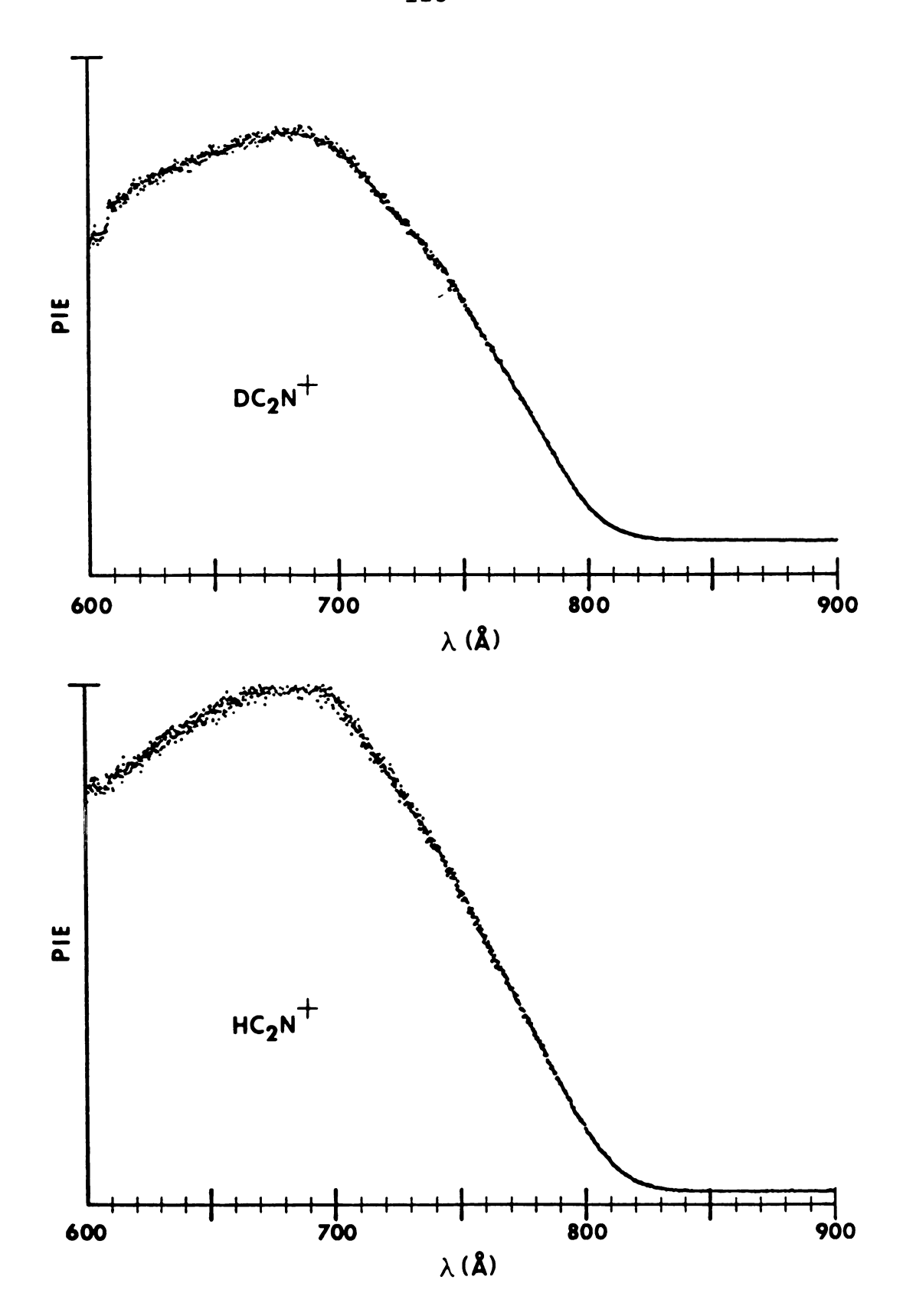


Figure IV-14. CHCN⁺ and CDCN⁺ PIE Curves.

Kinetic limitation is to be expected in this case since fragmentation to produce CHCN^+ (CDCN^+) is in competition with dissociation to produce $\mathrm{CH_2CN}^+$ ($\mathrm{CD_2CN}^+$).

The experimental APs determined by extrapolating the region 760-790 Å to the base line are 813 \pm 2 Å (15.25 \pm 0.04 eV) for CHCN⁺ and 807 \pm 2 Å (15.36 \pm 0.04 eV) for CDCN⁺. Because of the curvature at the foot of the PIEs, the extrapolation is much less certain than for CH₂CN⁺ (CD₂CN⁺), and this is reflected in the error limits. The AP reported for CHCN⁺ in reference 65 is 15.1 \pm 0.1 eV. This is significantly lower than the AP determined in this work and the difference may well be due to the (unspecified) procedure used in reference 65 to determine the AP.

The currently accepted literature value for the heat of formation of HCCN⁺ (1551 kJ/mole⁹¹) was calculated by using Dibeler and Liston's AP⁶⁵. This value is 150 meV lower than would be calculated from the AP determined in this work; however, the PIE curves reported here indicate that 1551 kJ/mole should be considered only as an upper limit for the heat of formation. The tails on the PIEs continue to lower energy with more intensity than can be accounted for by thermal energy alone, and it is estimated from the data of this work that the literature value may be more than 30 kJ too high.

There are two possibilities for the neutral fragments: two H-atoms (D-atoms) or $H_2(D_2)$. The formation of $H_2(D_2)$ is energetically more favorable by about 4.5 eV and is most certainly the pathway near threshold. Fragmentation to produce

two H-atoms (D-atoms) is estimated to be energetically possible at about 19 eV (650 \mathring{A}); however, there is no evidence that this pathway contributes to the PIEs, even at energies above 19 eV.

Since the heat of formation of $CDCN^+$ has not been reported it is worthwhile to calculate an upper limit; by assuming D_2 as the neutral product and by using the experimental AP, the upper limit for the heat of formation (298°K) of $CDCN^+$ is $\le 1564 \text{ kJ/mole}$.

3. CH_2^+, CD_2^+

The ${\rm CH_2}^+$ PIE curves (Figure IV-15 are very similar to the CHCN⁺ and CDCN⁺ PIE curves and show even more curvature at the thresholds. This is to be expected since this fragmentation process is in competition with two other pathways; the experimental APs should be considerably higher than the thermochemical threshold. Due to the curvature of the PIE curves in the threshold region it is difficult to accurately extrapolate the data. Nevertheless, extrapolation from the 730-750 Å region yields 811 ± 2 Å $(15.29 \pm 0.04$ eV) for ${\rm CH_2}^+$ and 805 ± 2 Å $(15.40 \pm 0.04$ eV) for ${\rm CD_2}^+$.

The AP reported by Dibeler and Liston 65 for $\mathrm{CH_2}^+$ (14.94 ± 0.02 eV) is considerably lower than the result of this work and its accuracy is questionable. $\mathrm{CH_2}^+$ was the lowest intensity fragment for which Dibeler and Liston determined an AP, and it can be assumed that its intensity was near the limit of sensitivity of their instrument.

It is difficult to estimate exactly how much more sensitive the MSU PIMS instrument is, but the PIE curves of ${\rm CH}_3^+$ and ${\rm H}_2{\rm CN}^+$

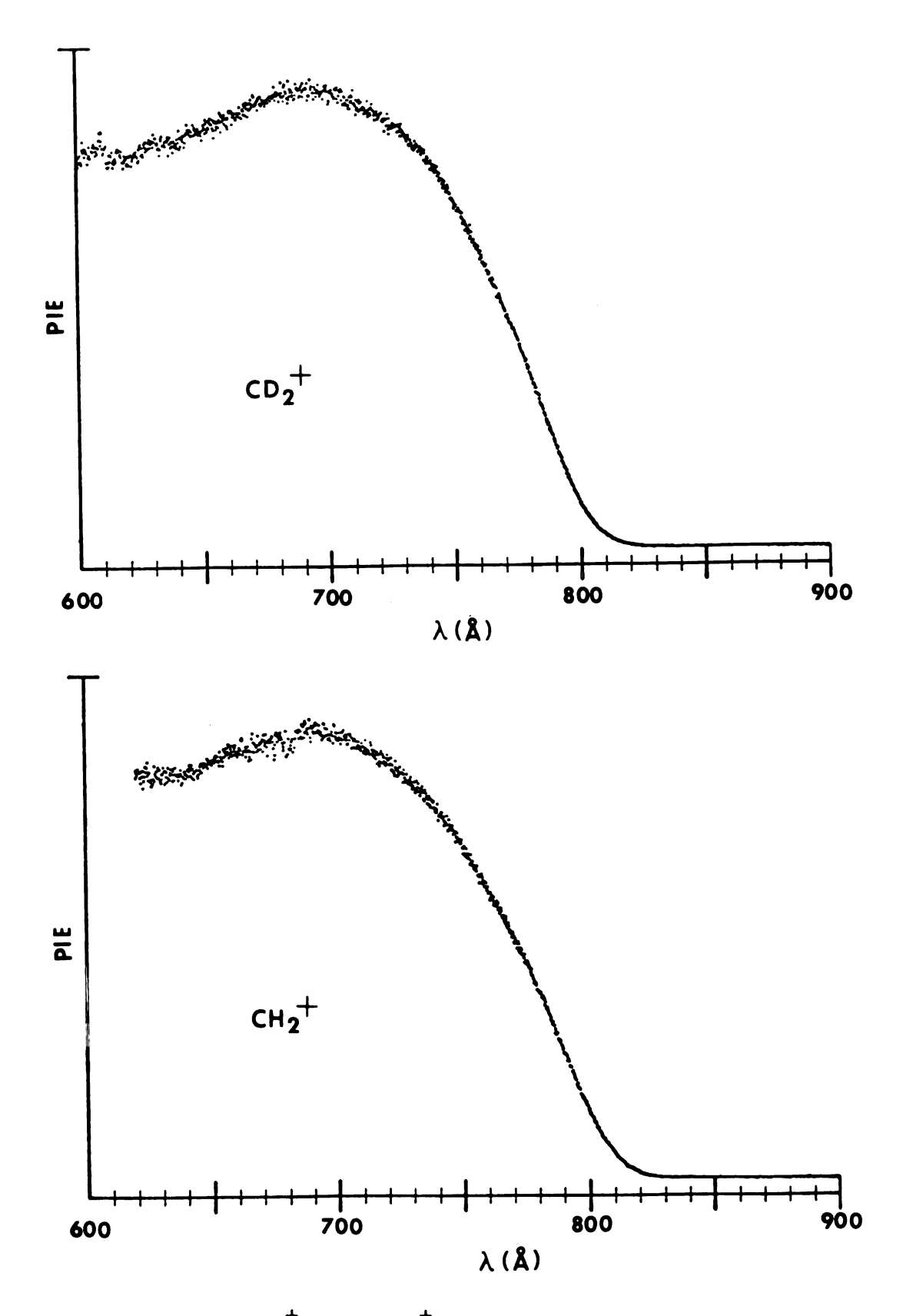


Figure IV-15. CH_2^+ and CD_2^+ PIE Curves.

(to be described subsequently), which are about one-third the intensity of ${\rm CH_2}^+$ (see Table IV-2), were recorded with a signal-to-noise ratio of better than 100. This fact amply demonstrates that the MSU instrument is considerably more sensitive than that of reference 65. Yet, the (low) AP reported by Dibeler and Liston is beyond any measurable intensity in the ${\rm CH_2}^+$ PIE curve reported here. Even if the first detectable signal of ${\rm CH_2}^+$ was assigned as the AP, the value would be higher than 14.94 eV.

The heat of formation of ${\rm CH_2}^+$ (1398 kJ/mole 91) has been accurately determined by several methods (from the spectroscopic IP of ${\rm CH_2}^{92}$ and by photoionization of ${\rm CH_3}^{93}$ and ${\rm CH_4}^{52}$. The thermochemical threshold for the formation of ${\rm CH_2}^+$ from ${\rm CH_3CN}$ calculated from this value is 14.92 eV when the neutral fragment is assumed to be HCN. If the neutral products are H + CN, the thermochemical threshold is 20.2 eV. HCN must be the neutral product in the region investigated in this work. The experimental AP for ${\rm CH_2}^+$ appears to be kinetically shifted above the thermochemical threshold by about 370 meV.

One can conceive of two different mechanisms by which the decomposition $CH_3CN^+ \rightarrow CH_2^+ + HCN$ could proceed. The H-CN bond could be formed simultaneously with the rupture of the C-C bond and a C-H bond, a one-step process; or a hydrogen atom could migrate to the cyanide group, followed by a rupture of the C-C bond, a two-step process. As will be shown below, the CH_3^+ and H_2CN^+ data strongly suggest that the two-step mechanism is the most likely pathway.

There is no currently accepted literature value for the heat of formation of ${\rm CD}_2^+$ to which to compare the AP of this work. However, the experimental AP is most likely kinetically shifted above the thermochemical threshold by even more than the AP of ${\rm CH}_2^+$, since deuterated ions always dissociate more slowly than their protonated analogs and more excess energy is necessary to produce the deuterated ion with a measurable intensity. An upper limit for the heat of formation of ${\rm CD}_2^+$ calculated from the experimental AP is 1441 kJ/mole. This value can be improved upon by assuming that the kinetic shift is at least equal to that of ${\rm CH}_2^+$ (370 meV). The result is that ${\rm \Delta H}_{\rm f_{208}}$ (${\rm CD}_2^+$) \leq 1399 kJ/mole.

4. CH_3^+, CD_3^+

The ${\rm CH_3}^+$ and ${\rm CD_3}^+$ PIE curves, which are smooth and featureless, are shown in Figure IV-16. These curves are expected to be competitively shifted even more than the previously-discussed fragment PIEs since this fragmentation channel is in competition with at least three others. The APs measured by extrapolating the data between 760 and 790 Å are 808 \pm 2 Å (15.34 \pm 0.04 eV) for ${\rm CH_3}^+$ and 797 \pm 2 Å (15.55 \pm 0.04 eV) for ${\rm CD_3}^+$. The APs of these ions from ${\rm CH_3CN}$ have not been previously reported.

The heat of formation of CH₃⁺ has been accurately determined ^{93,94,95} and the currently accepted literature value is 1095 kJ/mole. ⁹¹ The thermochemical threshold calculated from the heat of formation is 14.85 eV, which is approximately 490 meV below the experimental AP. The thermochemical threshold

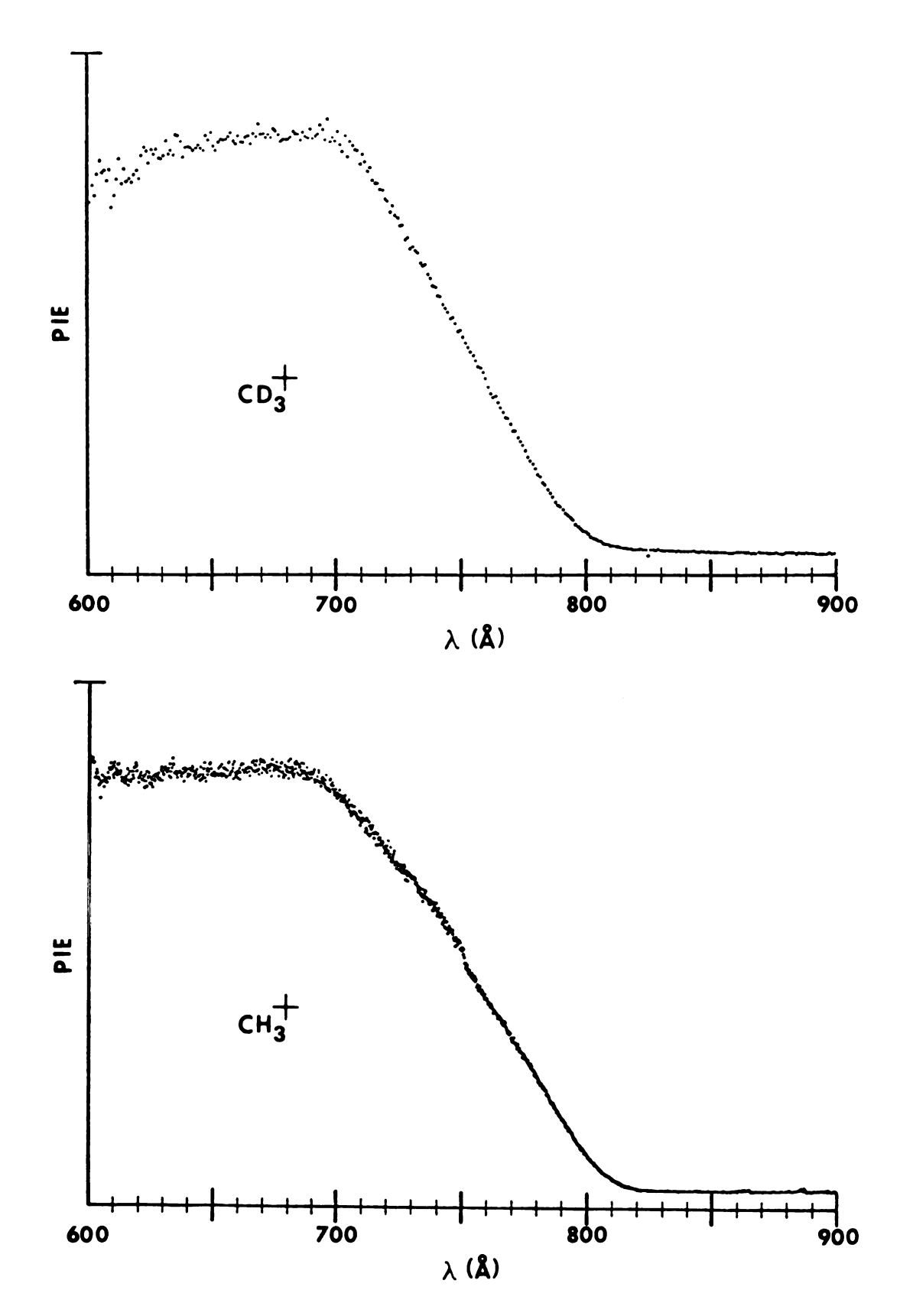


Figure IV-16. CH_3^+ and CD_3^+ PIE Curves.

is also 70 meV lower than that of $\mathrm{CH_2}^+$, yet the experimental AP is greater than the experimental AP of $\mathrm{CH_2}^+$ by 50 meV. Clearly, the fragmentation pathway to form $\mathrm{CH_3}^+$ is suppressed until well above the thermochemical threshold.

The heat of formation of ${\rm CD}_3^+$ is not available in the literature, and it is therefore worthwhile to calculate an upper limit from the AP. ${\rm \Delta H_f}({\rm CD}_3^+)$, corrected for the kinetic shift according to the results for ${\rm CH}_3^+$, is found to be ≤ 1103 kJ/mole.

It is surprising that the ${\rm CH_3}^+$ experimental AP is greater than that of ${\rm CH_2}^+$; in general one would not predict this result. Usually in the threshold region the fragment ion with the lower thermochemical threshold is produced at a higher rate and thus is more intense. It is therefore expected that ${\rm CH_3}^+$ would be produced with measurable intensity at lower energies than ${\rm CH_2}^+$. However, the difference between the thermochemical thresholds is small, and it is possible that the rate constant for the ${\rm CH_3}^+$ fragmentation near threshold increases more slowly with energy than that for ${\rm CH_2}^+$. The ${\rm CH_3}^+$ fragmentation may simply be too slow to compete with the ${\rm CH_2}^+$ fragmentation at photon energies near the ${\rm CH_2}^+$ threshold, and ${\rm CH_3}^+$ is therefore not detected until the photon energy is above the ${\rm CH_2}^+$ AP.

Another possible explanation for the anomalous AP would be a rapid migration of a hydrogen atom from the methyl group to the cyanide group. If the hydrogen migration was faster than the CH_3^+ fragmentation near the CH_3^+ thermochemical

threshold, there would be few parent ions with three hydrogens on the terminal carbon from which ${\rm CH_3}^+$ could be produced. ${\rm CH_3}^+$ would not be detected until an energy was reached at which the rate of fragmentation is comparable to the rate of rearrangement. On the other hand, the intensity of ${\rm CH_2}^+$ might be enhanced since its fragmentation channel would not be in competition with that to form ${\rm CH_3}^+$.

It is not unreasonable that such a migration would occur. Migrations of hydrogen atoms are common for gas phase ions, 96 as well as for ions in solution. 97 CH_3CN^+ is a radical ion and therefore there is a half-filled orbital to which a hydrogen could easily migrate. Moreover, hydrogen migration would not require an especially low potential barrier. The CH_3^+ threshold is more than 3 eV above the ground state of the parent ion. In solution hydrogen migrations occur at thermal energies, 97 and it is conceivable that migration would be energetically possible in the gas phase at energies far below the threshold for formation of CH_3^+ from CH_3CN .

It is interesting to speculate about possible structures for a rearranged parent ion. Some possibilities for which one hydrogen atom has migrated from the methyl group are shown below.

H C =
$$\dot{N}$$
:

H - C +

H - C +

H - C +

H - C +

H - C +

H - C +

H - C +

H - C +

H - C +

H - C +

H - C +

H - C +

H - C +

H - C +

H - C +

H - C +

H - C +

H - C +

H - C +

H - C +

H - C +

H - C +

H - C +

H - C +

H - C +

H - C +

H - C +

H - C +

H - C +

H - C +

H - C +

H - C +

H - C +

H - C +

H - C +

H - C +

H - C +

H - C +

H - C +

H - C +

H - C +

H - C +

H - C +

H - C +

H - C +

H - C +

H - C +

H - C +

H - C +

H - C +

H - C +

H - C +

H - C +

H - C +

H - C +

H - C +

H - C +

H - C +

H - C +

H - C +

H - C +

H - C +

H - C +

H - C +

H - C +

H - C +

H - C +

H - C +

H - C +

H - C +

H - C +

H - C +

H - C +

H - C +

H - C +

H - C +

H - C +

H - C +

H - C +

H - C +

H - C +

H - C +

H - C +

H - C +

H - C +

H - C +

H - C +

H - C +

H - C +

H - C +

H - C +

H - C +

H - C +

H - C +

H - C +

H - C +

H - C +

H - C +

H - C +

H - C +

H - C +

H - C +

H - C +

H - C +

H - C +

H - C +

H - C +

H - C +

H - C +

H - C +

H - C +

H - C +

H - C +

H - C +

H - C +

H - C +

H - C +

H - C +

H - C +

H - C +

H - C +

H - C +

H - C +

H - C +

H - C +

H - C +

H - C +

H - C +

H - C +

H - C +

H - C +

H - C +

H - C +

H - C +

H - C +

H - C +

H - C +

H - C +

H - C +

H - C +

H - C +

H - C +

H - C +

H - C +

H - C +

H - C +

H - C +

H - C +

H - C +

H - C +

H - C +

H - C +

H - C +

H - C +

H - C +

H - C +

H - C +

H - C +

H - C +

H - C +

H - C +

H - C +

H - C +

H - C +

H - C +

H - C +

H - C +

H - C +

H - C +

H - C +

H - C +

H - C +

H - C +

H - C +

H - C +

H - C +

H - C +

H - C +

H - C +

H - C +

H - C +

H - C +

H - C +

H - C +

H - C +

H - C +

H - C +

H - C +

H - C +

H - C +

H - C +

H - C +

H - C +

H - C +

H - C +

H - C +

H - C +

H - C +

H - C +

H - C +

H - C +

H - C +

H - C +

H - C +

H - C +

H - C +

H - C +

H - C +

H - C +

H - C +

H - C +

H - C +

H - C +

H - C +

H - C +

H - C +

H - C +

H - C +

H - C +

H - C +

H - C +

H - C +

H - C +

H - C +

H - C +

H - C

Many more structures can be drawn, including those with a C-C double bond and a C-N single bond, with no multiple bonds, or with only one hydrogen atom on the terminal carbon. Structures such as those shown above would seem most likely to have an effect on the CH₃⁺/CH₂⁺ fragmentation ratio since they are probably more stable than structures with no multiple bonds, whereas those with a C-C double bond and a C-N single bond would be more likely to fragment at the C-N bond. Structures with only one hydrogen on the terminal carbon would preclude fragmentation to form CH₂⁺.

The stability of the above structures with respect to one another and to $\mathrm{CH_3CN}^+$ with the methyl group intact would be an important factor for determining the possible contribution of each. However it is difficult to judge the relative stabilities, especially considering that a rearranged molecular ion

could be in an excited electronic state and that no molecular ions of these structures have ever been studied. Ions (1-6) are drawn primarily to demonstrate that fairly reasonable structures for a rearranged parent ion can be constructed.

There is some evidence that structure (5) might be more stable than the others. Ketenimine, the neutral equivalent of (5), has been identified as a photolysis product of acetonitrile. Moreover, SCF-MO calculations show ketenimine to be the next most stable molecule with a C-C-N framework to acetonitrile. Structure (5) has also been proposed as the geometry of the ion at m/e=41 in the mass spectra of longer-chain aliphatic nitriles. The CH₂ fragmentation channel might be on an excited state surface of the manifold of states belonging to structure (5).

Another factor which should not be overlooked when rationalizing a fragmentation mechanism is the stability of the products. The more stable products are almost always favored. Structures (3)-(6) imply that the neutral fragment for the CH_2^+ fragment channel is hydrogen isocyanide (CNH), while structures (1) and (2) would lead directly to hydrogen cyanide (HCN). This would suggest that structures (1) and (2) might be more important for the CH_2^+ fragment channel.

Unfortunately, the PIE curves do not provide structural information about the parent ion at energies above the first fragmentation threshold or about the fragment ions. The anomalous ${\rm CH_3}^+$ AP, together with the above ideas, would suggest that a hydrogen migration does influence the ${\rm CH_3}^+$ (CD₃⁺)

fragmentation, as will be discussed in the next section.

5. H_2CN^+ , D_2CN^+

The $\mathrm{H_2CN}^+$ and $\mathrm{D_2CN}^+$ PIE curves are shown in Figure IV-17. $\mathrm{H_2CN}^+$ and $\mathrm{N_2}^+$ both have m/e=28, and even though the acetonitrile sample was thoroughly degassed, autoionization structure due to $\mathrm{N_2}^+$ was readily apparent in the $\mathrm{H_2CN}^+$ PIE curve. The $\mathrm{N_2}^+$ PIE curve is very distinctive, being predominated by autoionization, which made it possible to correct the $\mathrm{H_2CN}^+$ PIE by subtracting from it a scaled $\mathrm{N_2}^+$ PIE. The curve shown in Figure IV-17 is the result of the subtraction.

The APs determined by extrapolating the region 750 - 780 \hat{A} are 797 \pm 2 \hat{A} (15.56 \pm 0.04 eV) and 794 \pm 2 \hat{A} (15.61 \pm 0.04 eV) for H_2CN^+ and D_2CN^+ , respectively. The difference in the AP of the protonated and deuterated ion may reflect both disparate kinetic shifts and zero point energy differences.

The reaction channel for the neutral fragment CH is 3.5 eV lower than the channel for C+H, and it can be safely assumed that CH(CD) is the neutral fragment of this dissociation at threshold. The extrapolated AP for ${\rm H_2CN}^+$ results in a calculated heat of formation of <1009 kJ/mole. For ${\rm D_2CN}^+$ the result is <997 kJ/mole. There is no currently accepted literature value for ${\rm \Delta H_f(H_2CN}^+)$ (or ${\rm \Delta H_f(D_2CN}^+)$) from which to determine the kinetic shift, and since this fragmentation channel is in competition with several others, the values should be considered only as upper limits.

It is difficult to conceive of a mechanism for the formation of ${\rm H_2CN}^+$ in which two hydrogens from the methyl group are

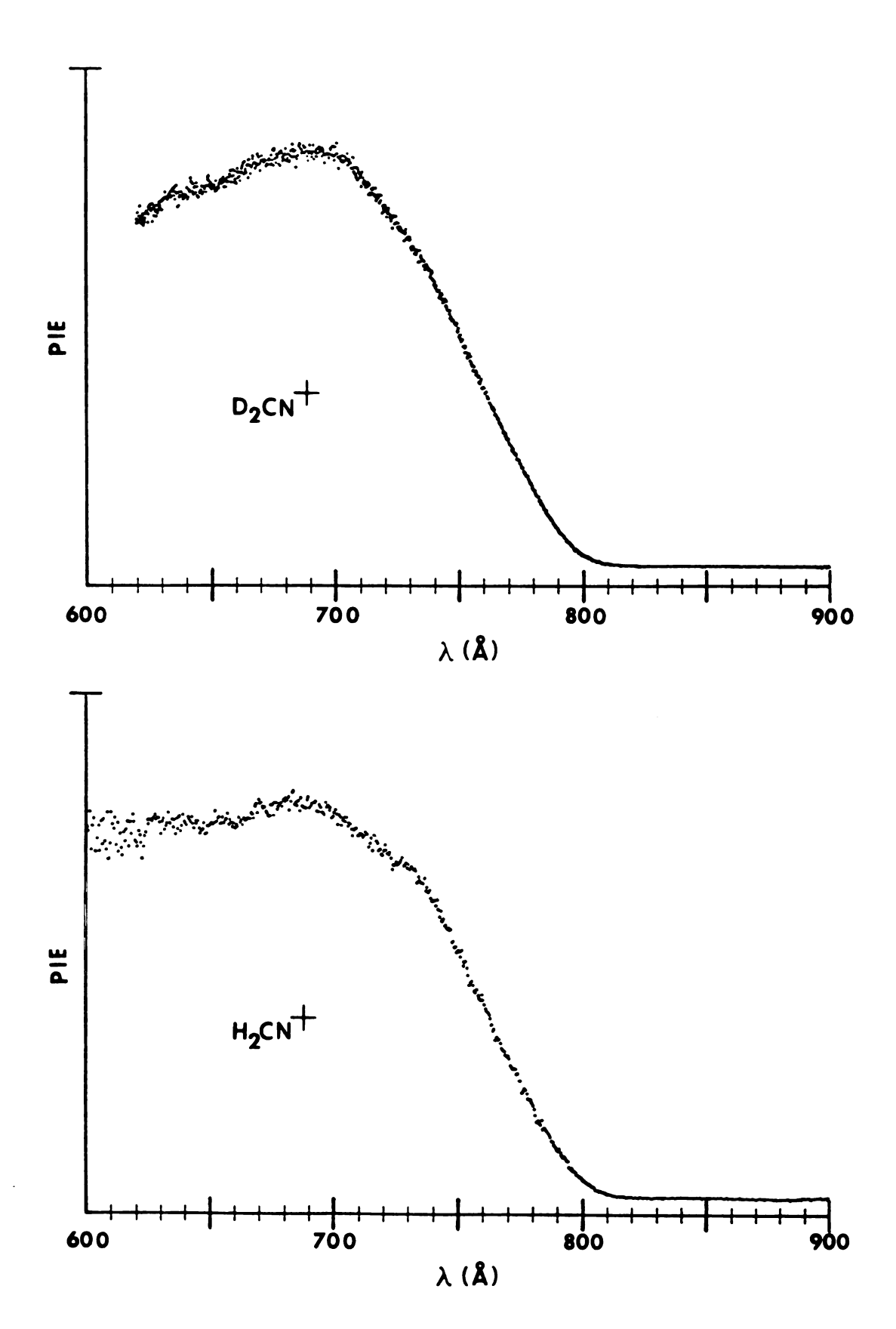


Figure IV-17. H_2CN^+ and D_2CN^+ PIE Curves.

transferred to the cyanide group in concert with the breaking of the C-C bond. It is most probable that this fragmentation proceeds via a rearranged parent ion intermediate in which two hydrogens have migrated from the terminal carbon to the nitrile moiety. Again it is entertaining to speculate about possible structures for a rearranged parent ion, and in this case about the structure of the fragment ion also. Some possibilities for H₂CN⁺ are:

H C = N · H - C = N : H - C
$$\equiv$$
 N - H : C = N | H (7) (8) (9) (10)

On the basis of the PIE curve alone it is not possible to make a definite assignment of the structure of the ion at m/e=28. There is thermochemical evidence for structure (9), protonated hydrogen cyanide. The proton affinity of HCN in the gas phase has been measured, 100,107 and the heat of formation of H-C=N-H is 942 kJ/mole, a value that is 67 kJ/mole lower than ΔH_f determined from the experimental AP. This difference is reasonable, considering the kinetic shift of the experimental AP, and thus structure (9) is consistent with the available data.

Some structures which can be drawn for ${}^{\rm H}_3{}^{\rm C}_2{}^{\rm N}^+$ for which two hydrogens have migrated from the methyl group are:

Structures (11) and (12) would lead most directly to ion (9). The photoionization data do not provide any evidence for the contribution of structures (13)-(15), but at excitation energies above 20 eV, structures with two hydrogens on the nitrogen must be formed since $\mathrm{NH_2}^+$ is detected in the electron impact mass spectrum. 62

The relative intensities of ${\rm CH_2}^+$, ${\rm H_2CN}^+$ and ${\rm CH_3}^+$ in the photoionization mass spectrum are 1:0.29:0.24, respectively. Without the benefit of the experimental AP and PIE curves of these ions this would be a rather unexpected result. In general, one would not predict that ${\rm CH_2}^+$ would be four times as intense as ${\rm CH_3}^+$. However, this is easily explained when hydrogen migrations are taken into account. The rapid migration of hydrogen reduces the number of excited parent ions with the methyl group intact from which ${\rm CH_3}^+$ must be formed and thus limits the intensity of ${\rm CH_3}^+$. The fact that ${\rm CH_2}^+$ and ${\rm H_2CN}^+$ are more intense than ${\rm CH_3}^+$ means that the migration must

be more rapid than the CH_3^+ fragmentation, even at 21 eV.

The detection of ${\rm H_2CN}^+$ and ${\rm D_2CN}^+$ provides clear evidence that hydrogen and deuterium atom migrations do occur, at least at photon energies above ~15.6 eV. The APs of ${\rm CH_2}^+$ and ${\rm CH_3}^+$ (15.29 and 15.34 eV respectively) are only slightly lower than that of ${\rm H_2CN}^+$ (${\rm D_2CN}^+$), and it is reasonable that migration is important also at the fragmentation thresholds for these ions.

Summary of Appearance Potentials and Heats of Formation. Table IV-8.

		Appearance P	Appearance Potential (eV)		
From CH ₃ CN Ion	Neutral	This Work	PI Literature ^b	ΔH _{fo} (kJ/mole) ^C	$^{ m \Delta H}_{ m f298}$ (kJ/mole) $^{ m c}$
$^{\text{H}_2\text{C}_2\text{N}^+}$	н	13.99 ± 0.01	14.01 ± 0.02 ⁶⁵	1235 ± 1 ^d	
HC_2N^+	Н2	15.25 ± 0.02	15.1 ± 0.1 ⁶⁵	1551 ^{65,91}	
CH ₂ +	HCN	15.29 ± 0.02	14.94 ± 0.02 ⁶⁵ 14.92 ⁹¹ ,c	≤1398 ⁹¹	
CH ₃ +	N	15.34 ± 0.04	14.85 ⁹¹ ,c	1095 ⁹¹	
$^{+}_{2}$ CN $^{+}$	СН	15.56 ± 0.04			≤1009 ^d
From CD ₃ CN					
$D_2C_2N^{\dagger}$	Д	14.15 ± 0.01		1234 ± 1 ^b	
DC ₂ N ⁺	D_2	15.36 ± 0.02			≤1565 ^d
$c_{D_2}^+$	DCN	15.40 ± 0.02			≤1399 ^d
CD ₃ +	CN	15.55 ± 0.04			≤1103 ^d
D ₂ CN ⁺	CD	15.61 ± 0.04			₅ 997 ^d

^aLiterature values for heats of formation are listed when they are considered to be more reliable.

drhis work.

bhotoionization literature values.

^cBased on heat of formation of neutrals from Table IV-6.

CHAPTER V.

CONCLUSIONS AND SUGGESTIONS FOR FURTHER WORK

The acetonitrile PIE curves yield a remarkable amount of information for a photoionization mass spectrometry investigation. From the parent ion curves, accurate ionization potentials for the 3e (C=N bonding) and 5a₁ (nitrogen lone pair) orbitals of CH₃CN and CD₃CN were determined and it was found that the 3e ionization potential is isotope dependent. Previously unresolved vibrational structure was observed in the CH₃CN⁺ PIE, from which the vibrational frequency of the CCN bending mode of the ground state of the parent ion was measured. This in turn led to the conclusion that the Jahn-Teller effect is operable in this ionic state. Rydberg series converging to the first and second excited electronic states of the ion were observed and definitive series assignments were made.

The fragment ion PIE curves provided less structural information than the parent ion curves, but they did reveal the important fragmentation pathways and mechanisms. Accurate heats of formation of ${\rm H_2CCN}^+$ and ${\rm D_2CCN}^+$ were determined. The remaining fragment ion APs were kinetically shifted, but comparison with accurate literature values for the protonated fragments provided corrections for their deuterated counterparts. Although the derived heats of formation are only upper limits for these fragments, the data should be useful to scientists interested in the ion chemistry of acetonitrile.

Often a thesis research project raises new questions.

The unanswered questions resulting from this investigation

lead to the suggestion of further experiments that should help

provide a more complete understanding of the ionization and

fragmentation of acetonitrile.

Although the CCN bending vibration was resolved in the $\mathrm{CH_3CN}^+$ PIE curve, it was not observed for the deuterated ion. It was suggested that this transition was obscured by autoionization in $\mathrm{CD_3CN}^+$. A high resolution photoelectron spectrum of $\mathrm{CD_3CN}$ should be able to resolve this feature and would be useful for confirming the observations of the PIMS experiment.

One of the shortcomings of any mass spectrometric experiment is that only the m/e of an ion is measured, and one must use other sources of information to infer the structures of the detected ions. The PIMS data show that rearrangement of the parent ions occurs at energies above the H₂CN⁺ threshold, and strongly suggest that a rearrangement is important at even lower energies. However, the data reveal neither a precise energy threshold for the rearrangement nor the structure(s) of the rearranged ion. A potentially useful experiment in this regard would be a matrix isolation study of the parent ions. In a low temperature, inert matrix the parent ions may well retain the rearranged geometry, and their structures could be determined by means of standard spectroscopic techniques such as infrared and visible-ultraviolet absorption spectroscopy and Raman scattering, perhaps supplemented by ESR

measurements. The approximate energy at which the rearrangement becomes possible could be determined by observing changes in the spectra of the matrix-isolated ions as a function of the ionizing energy. This technique has been successfully applied to several ionic systems. 102

The rearrangement of the parent ion raises questions about the structures of the ${\rm H_2C_2N}^+$, ${\rm HC_2N}^+$ and ${\rm H_2CN}^+$ fragments (and their deuterated counterparts). To which atoms on the carbon-nitrogen framework are the hydrogen atoms bonded? The structures of these ions could also be studied with the matrixisolation technique.

The relative intensity and energy dependence of a fragment ion PIE is a function of an energy-averaged fragmentation rate constant and the number and distribution of parent ion states populated with sufficient energy to fragment. From the PIE curve one can determine an appearance potential and the energy dependence of the ion yield, and a reasonable fragmentation mechanism can often be deduced. However, several parameters remain unknown; the kinetic and internal energy of the fragments is not measured and the potential surface on which the fragmentation occurs is not determined.

tron coincidence technique (PIPECO) is well suited for determining these parameters. ²¹

Experimentally, PIPECO is very similar to ordinary PIMS, with the added feature of an electron energy analyzer which is most often constructed to detect only zero-kinetic energy electrons. Only fragment ions that are produced in coincidence

with an electron of zero-kinetic energy are detected, and their intensity is followed as a function of photon energy. Since the photon and electron energy are precisely known, the excitation energy of the parent ion is determined and the fragmentation rate of state-selected parent ions is directly measured. With a knowledge of the electronic structure of a parent ion (i.e. the photoelectron spectrum), one can directly infer the ionic state from which the fragmentation occur. Further, in a PIPECO experiment the fragment ions are often mass selected by their time of flight from the ionization region to the ion detector. From the mass spectral line shapes (the intensity versus time distribution of ions of a given mass) one can often arrive at the kinetic energy release accompanying the fragmentation. (More details on PIPECO can be found in reference 103.)

A PIPECO investigation of acetonitrile could be interesting and informative. As a supplement to the PIMS data, it would be useful for measuring the kinetic shifts of the experimental APs, allowing more accurate heats of formations of the various fragments to be determined. As an extension of the acetonitrile investigation, it would provide a measurement of the state-selected fragmentation rate constants, which in turn would provide a more complete characterization of the fragmentation mechanisms. Moreover, the rate constants could be compared directly with those calculated with the statistical theory of mass spectra.

Although some questions remain, it should be emphasized

that the photoionization mass spectrometric investigation reported in this dissertation was highly successful. Acetonitrile is the first molecule to be studied in detail with the PIMS apparatus which was designed and constructed at MSU. The instrument performed extraordinarily well and allowed the study of processes too weak to observe with instruments which are not computer-controlled. Valuable thermochemical and kinetic information has been obtained for acetonitrile.

APPENDIX A

PIE curves are most reliably acquired by recording the curve of a single m/e at a time, hence the mass spectrometer is used most of the time in a fixed mass mode. However in the course of an investigation it is often desirable to scan the transmitted m/e to record a mass spectrum. The Extranuclear quadrupole mass filter controller used in this investigation does not have this capability but it does have provisions for the addition of mass scanning circuitry. The mass can be scanned via an externally supplied voltage or current ramp. The following is a description of a digital ramp generator that was designed and constructed as part of this thesis research.

There were several design requirements to be considered for use in conjunction with the MSU PIMS instrument. First, it was desirable to be able to control the ramp generator with the PDP-8/M computer that is used to operate many other devices on the instrument and to also be able to manually operate the device. Second, the ramp generator needed to be linear to insure the linearity of the mass scale of a mass spectrum. Third, the device needed to be stable over a long period of time, and fourth, it needs to provide scan rates over the range of 10 ms to several hours.

A block diagram of the device is shown in Figure A-1.

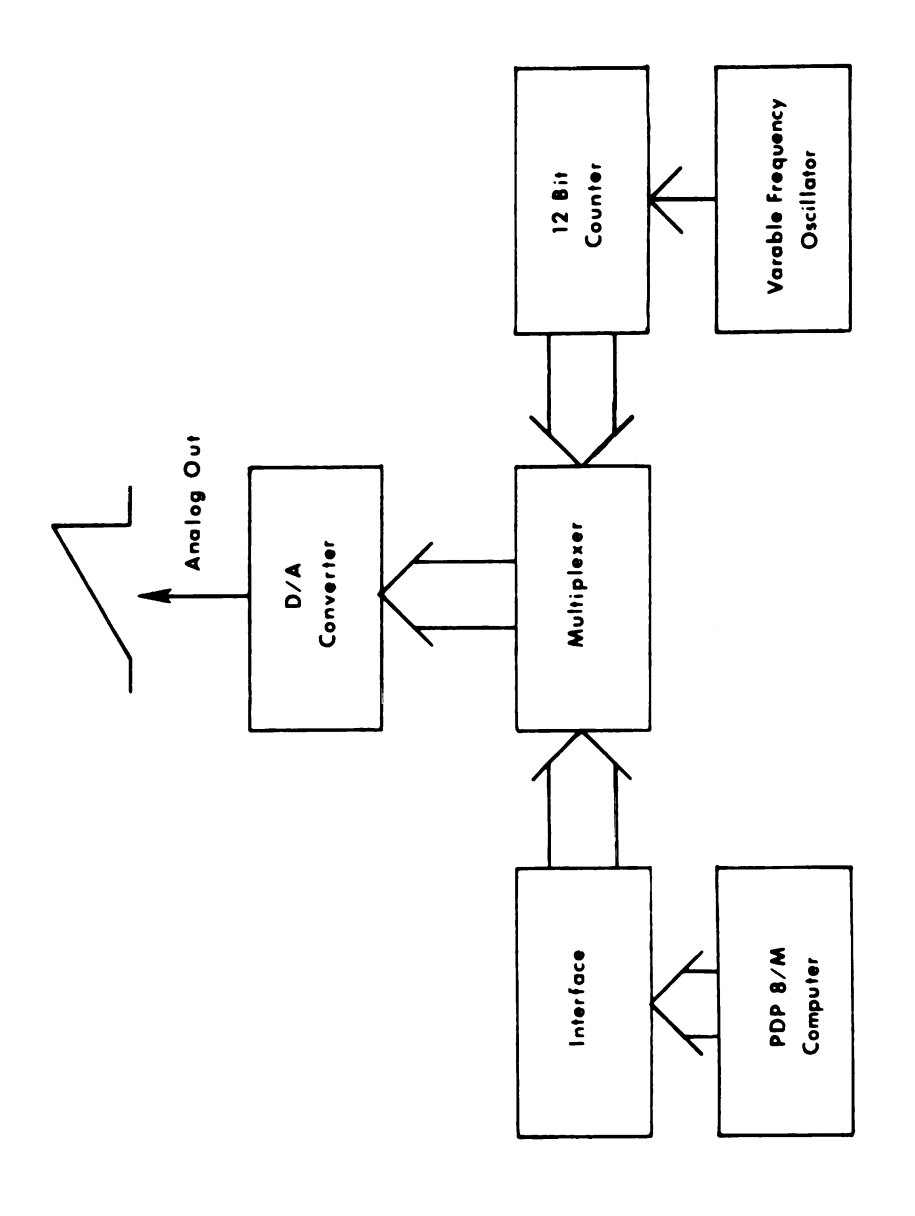


Figure A-1. Block Diagram of Digital Mass Scanner.

The heart of circuit is a 12-bit digital-to-analog converter which receives a 12-bit number from the PDP 8/M mini-computer via an interface circuit or from a 12-bit counter for manual operation. Under computer control the DAC input can be set to any desired value or incremented one bit at a time. The manual control allows the input to be set to a fixed value via a thumb wheel switch or to be scanned by filling the counter with counts from a variable rate oscillator.

The circuits are built on three separate wire wrap boards which are connected with 3-M ribbon cable. The computer interface board is mounted in a card cage in the computer rack which provides access to all signals necessary for communication with the computer. The other two boards, the main logic board and the analog board, are mounted in an aluminum box in a rack containing the mass spectrometer power supplies. The circuits are constructed primarily from standard TTL integrated circuits.

Figures A-2 and A-3 are schematics of the computer interface circuits. Their locations on the computer interface board are shown in Figure A-4. The circuit consist of a 12-bit counter (11-13) and comparator (8-10) which are connected to the computer lines (AC00-11) via latches (1-4). The counters allow the mass to be scanned at a maximum rate by incrementing the count with the increment line. The end of a scan can be checked for with the computer via the SKP line. This allows a preselected mass range to be scanned in a minimum amount of time by eliminating the need to increment and to check the value of a number in the computer accumulator.

The main logic board (Figures A-5 to A-11) consist primarily of the circuits for manual control. It also contains the line receivers for the connections with the computer interface board. The connections from the computer interface board are electrically isolated from the main logic board with 6N137 optoisolators (Figure A-5). This was necessary to eliminate current loops which introduced 60 cycle noise on the output of the D/A converter.

The manual control circuits consist of a crystal controlled oscillator time base and divider (Mostek MK5009P, Figure A-6), a one-through-ten frequency divider (Figure A-7) and a twelve-bit counter (Figure A-8). The MK5009P is used with a 409.6 KHz crystal. With its built-in frequency divider and external control circuitry it provides an output frequency that allows base scan times of 0.01s, 0.10s, 1s, 10s, 1 min.,

and I hour. The output of the base frequency generator goes to a variable, one through ten frequency divider. The output from this circuit is accumulated by the twelve-bit counter whose outputs are connected to the digital-to-analog converter via multiplexers (Figure A-8). The multiplexers allow selection of input from the computer or the manual operation counter.

The manual operation counter can be set to a preset value with thumb wheel switches (Figure A-9). In addition provisions were made to set the counter to all low or all high and to select continuous or single scanning (Figure A-10). The input to the D/A is displayed with seven-segment LEDs.

The analog board (Figure A-12) contains only the digital-to-analog converter (Datel model HZ12BMC). The circuits were originally constructed with the digital-to-analog converter on the main logic board, however there was excessive pickup of digital noise on the analog output. This problem was most easily eliminated by placing the digital-to-analog converter on a separate circuit board. The analog output of the converter is connected to the quadrupole power supply with a short BNC cable.

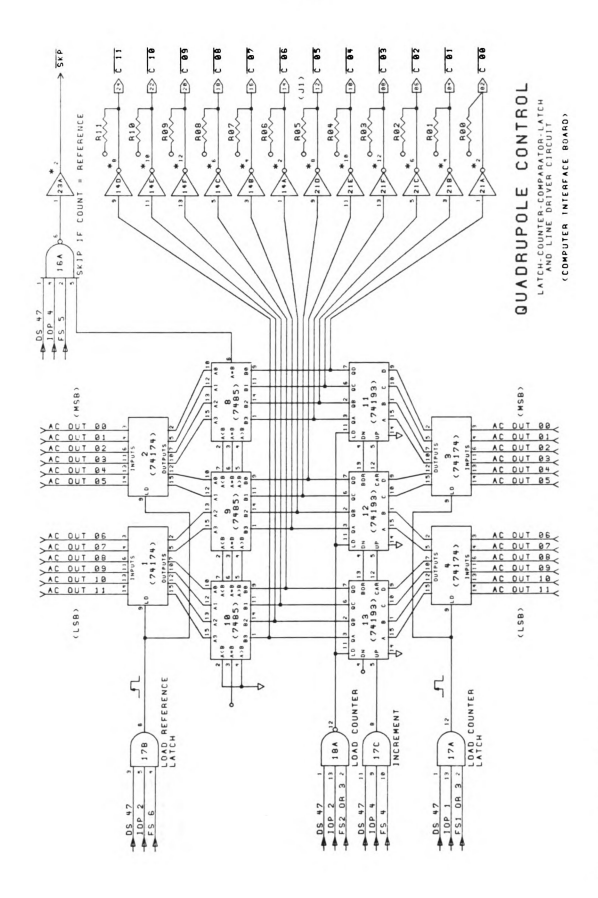


Figure A-2. Scanner Computer Interface.

COMPUTER INTERFACE BOARD

R 12

QUADRUPOLE CONTROL SKIP ON MANUAL CIRCUIT

→ SKP

SKIP ON MANUAL

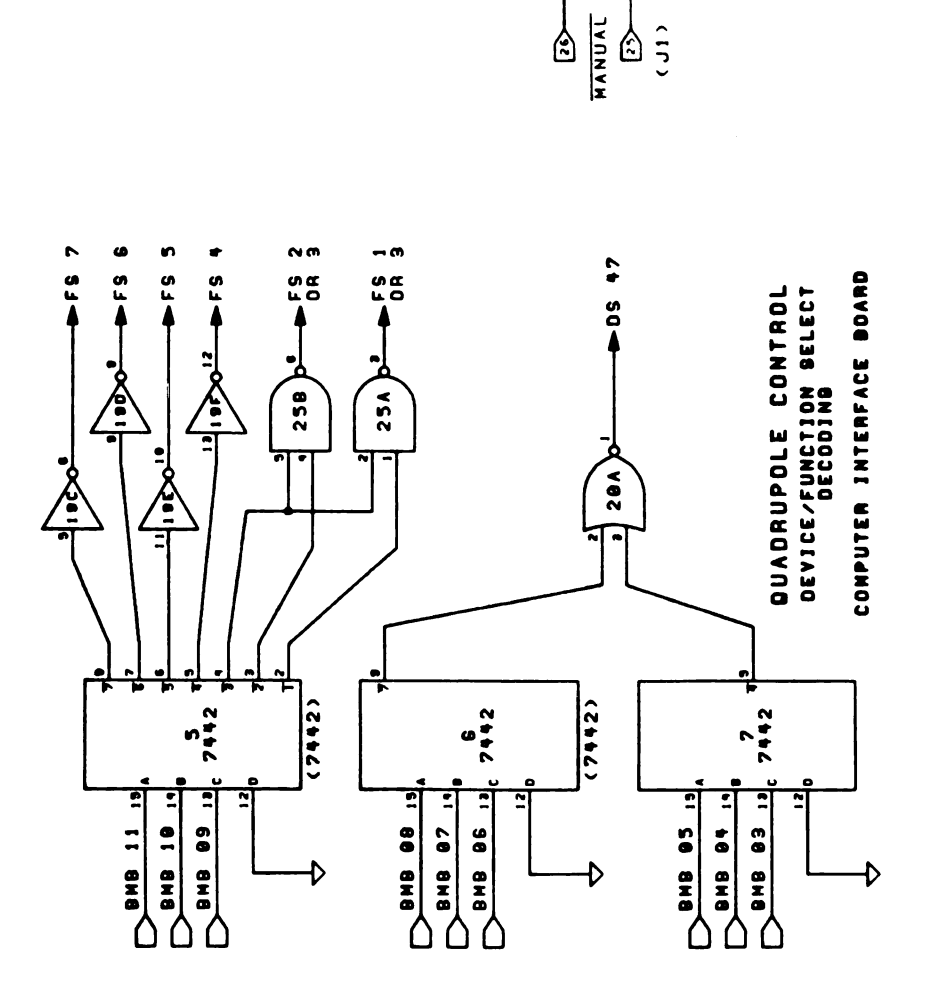


Figure A-3. Scanner Computer Interface.

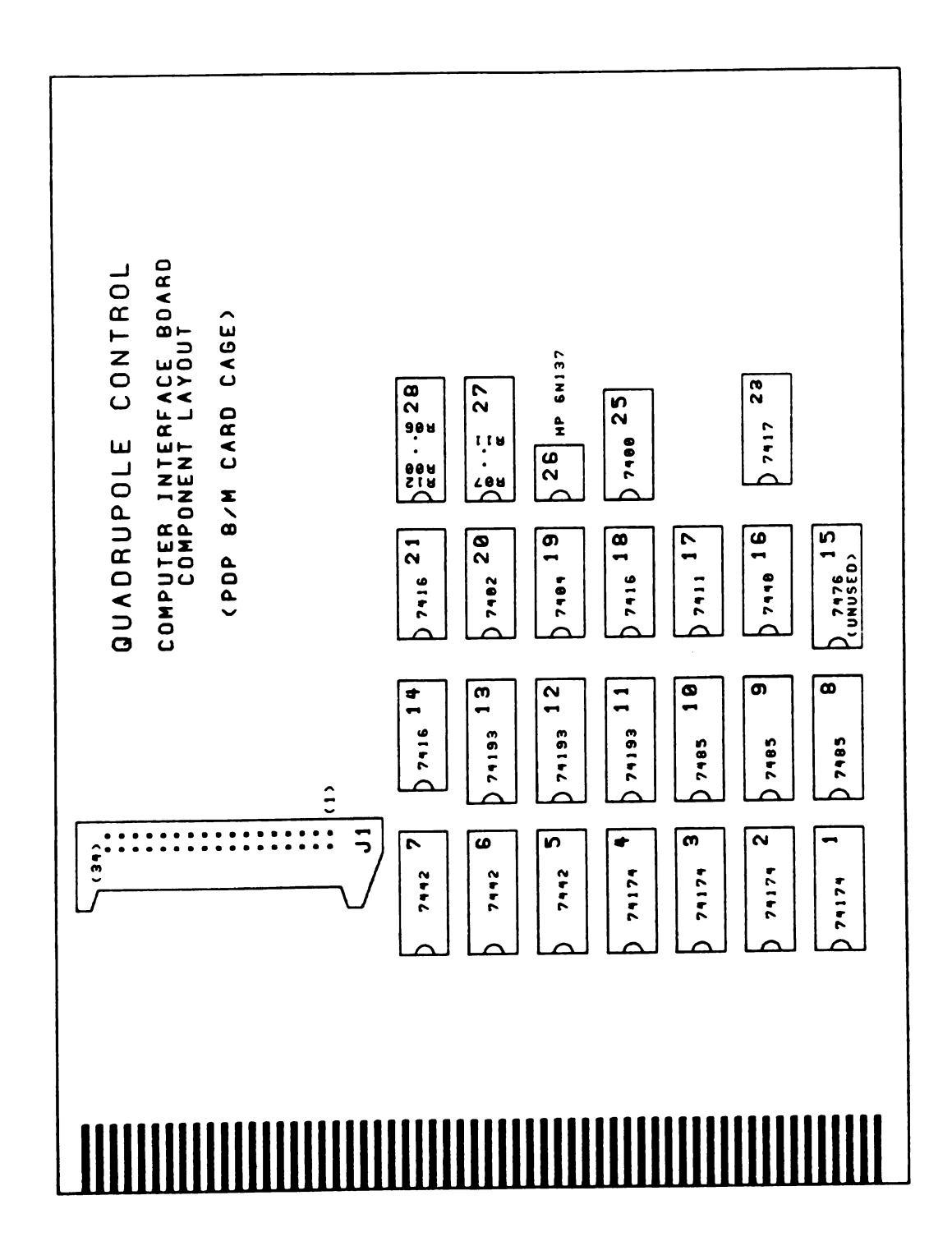


Figure A-4. Computer Interface Board Layout.

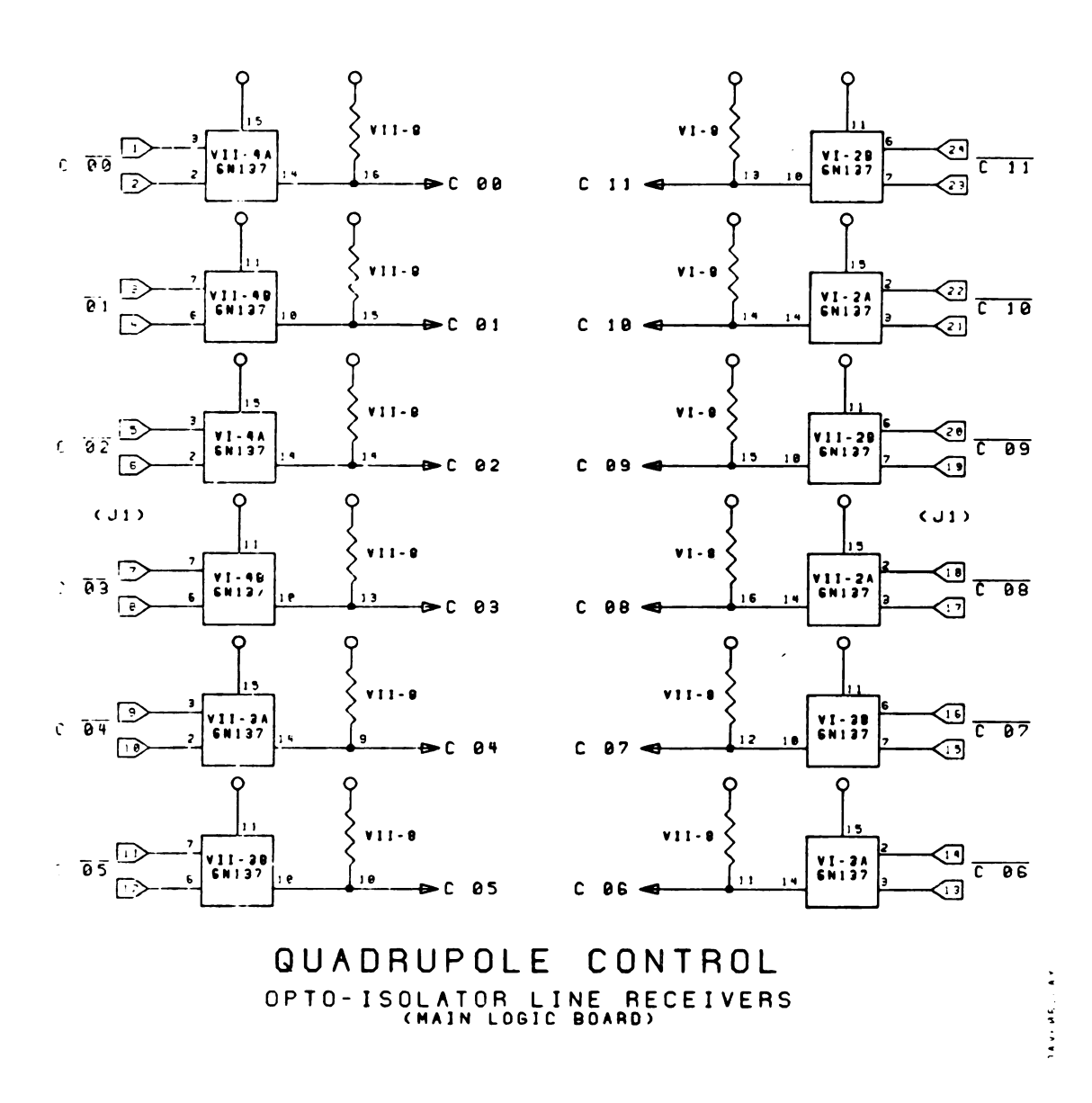


Figure A-5. Main Logic Board Optoisolator Line Receivers.

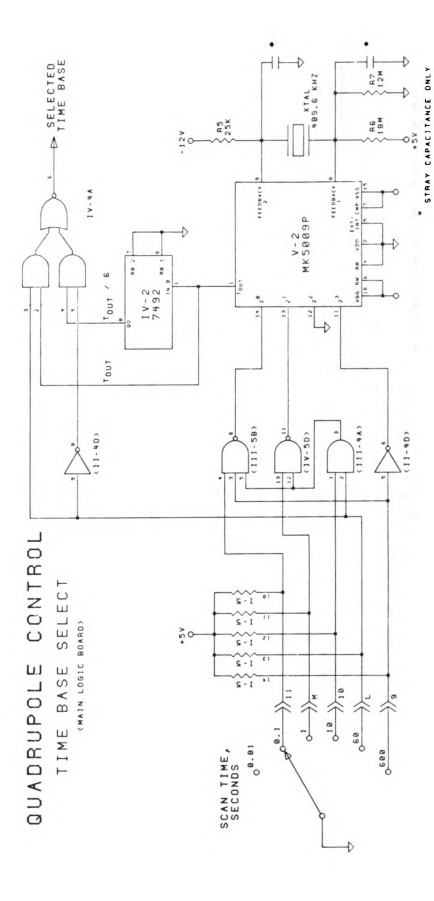


Figure A-6. Main Logic Board Time Base Circuit.

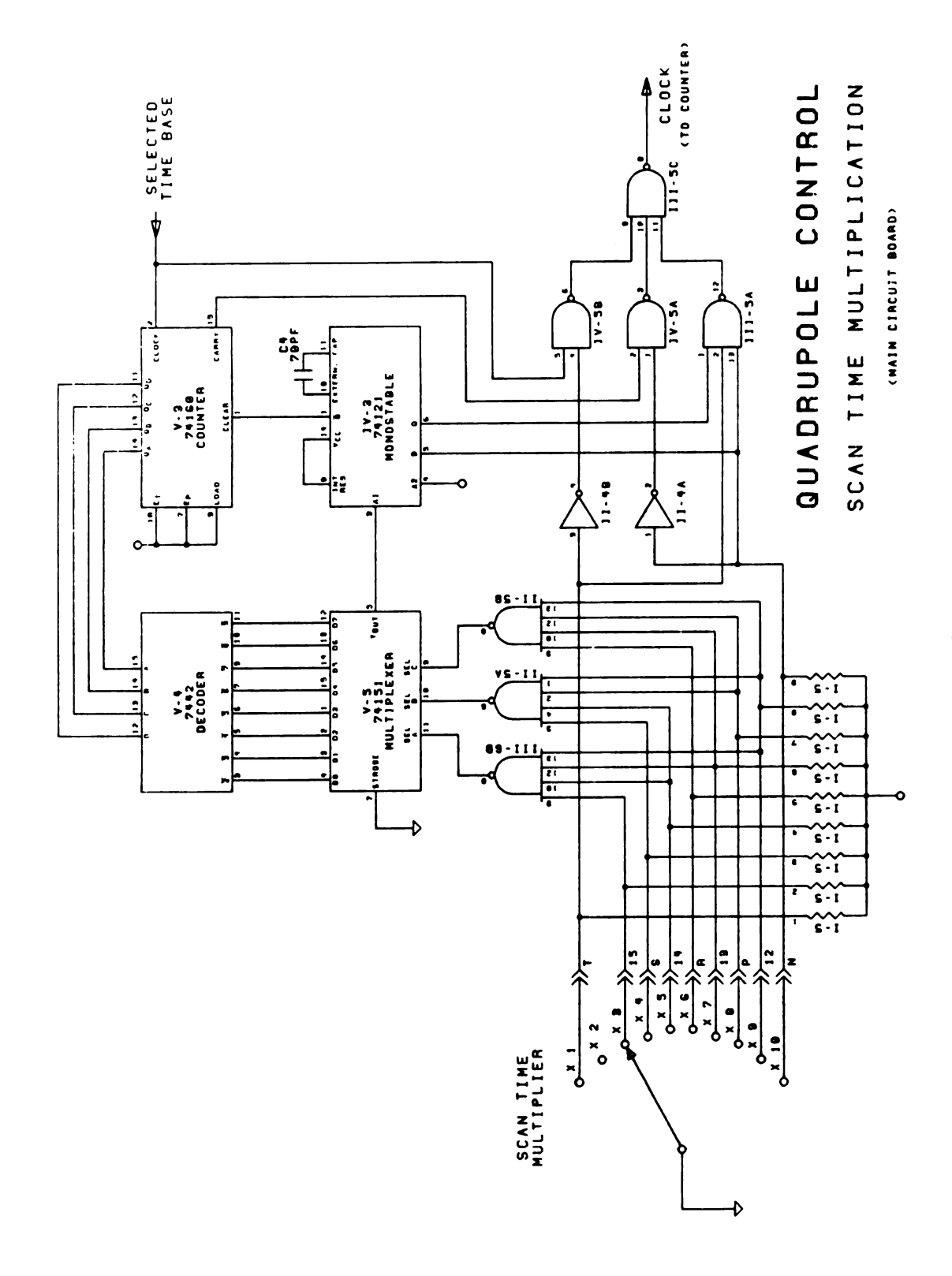
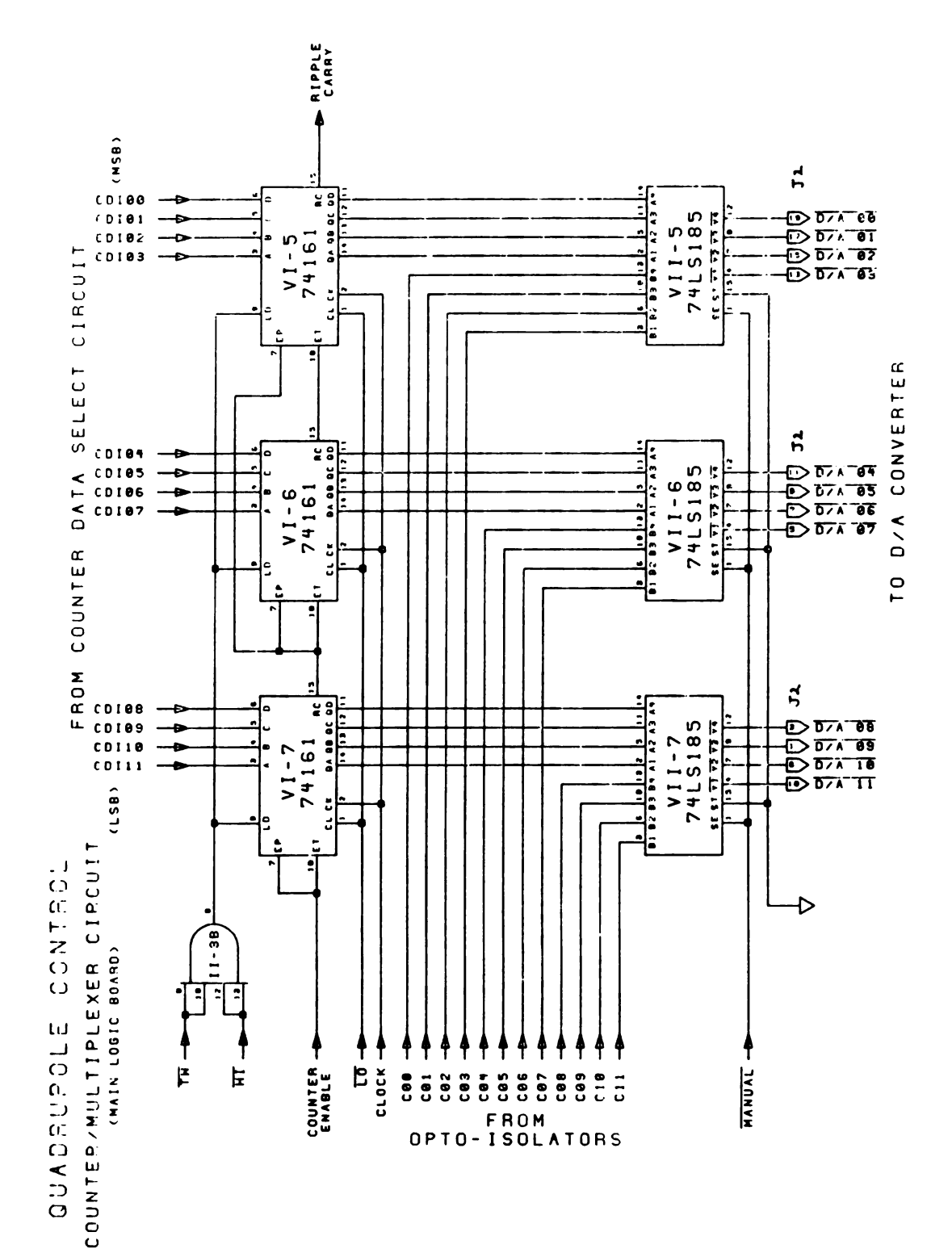
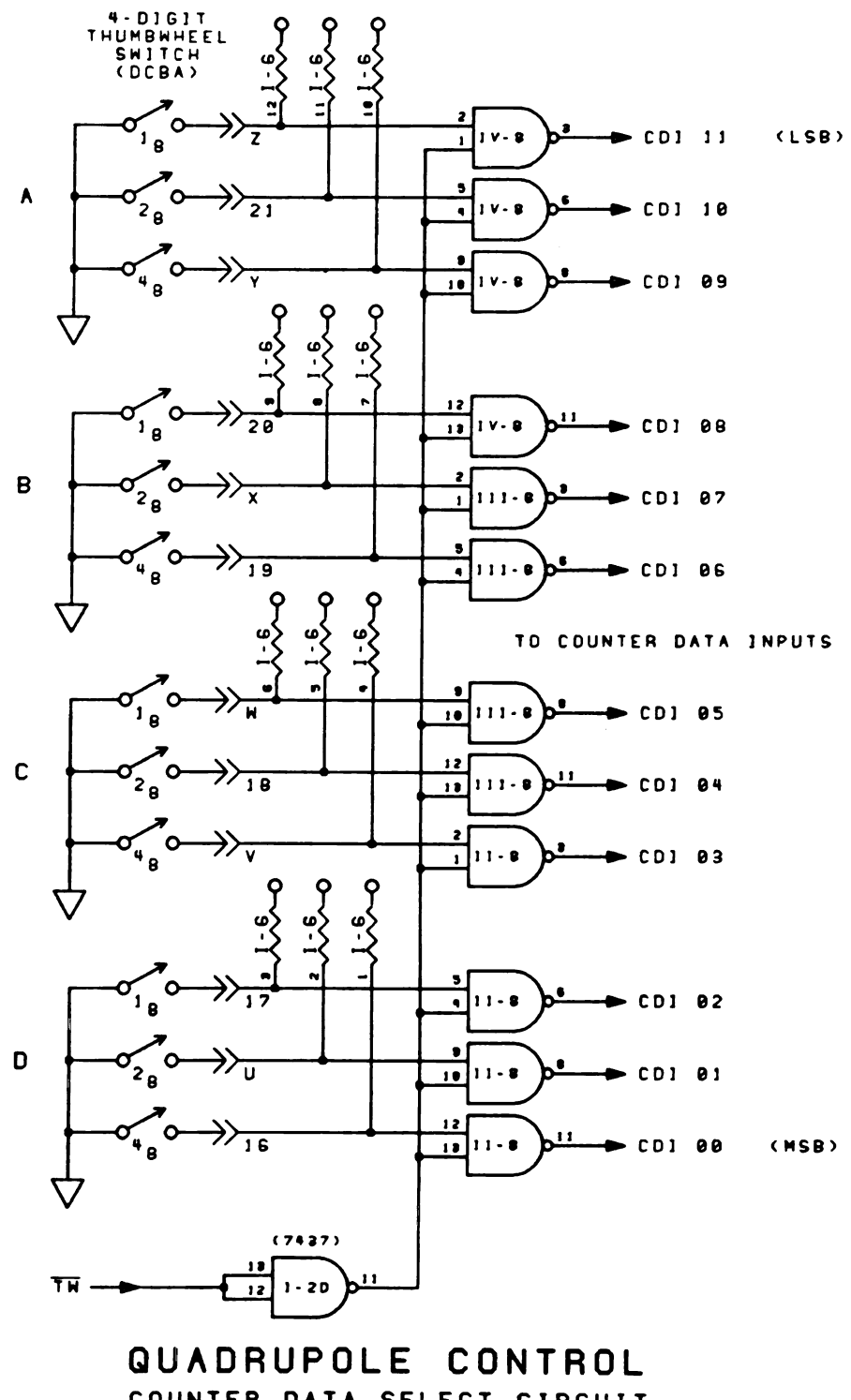


Figure A-7. Main Logic Board Scan Time Multiplier.

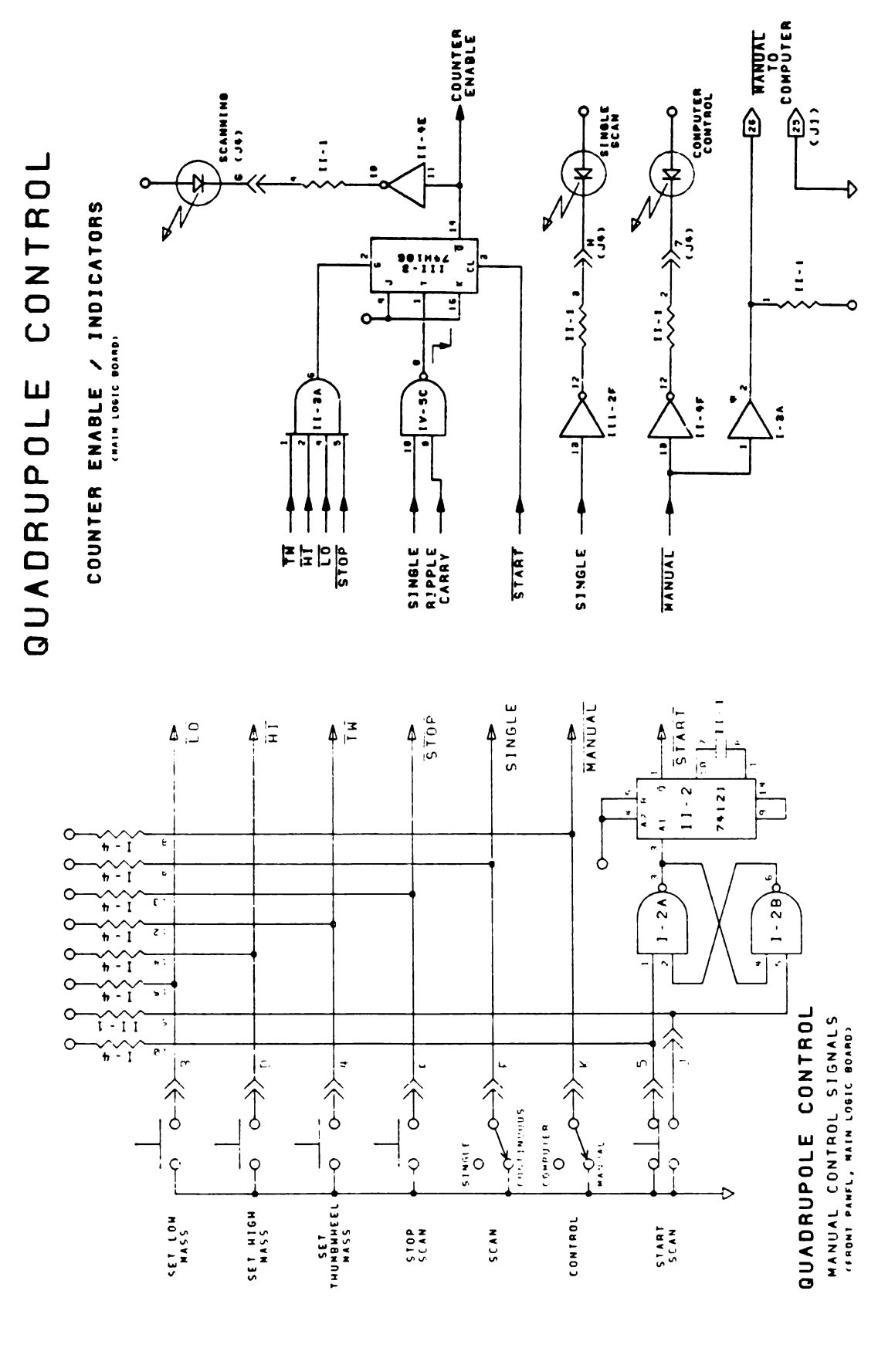


Main Logic Board Twelve Bit Counter and Multiplexer Circuit. Figure A-8.

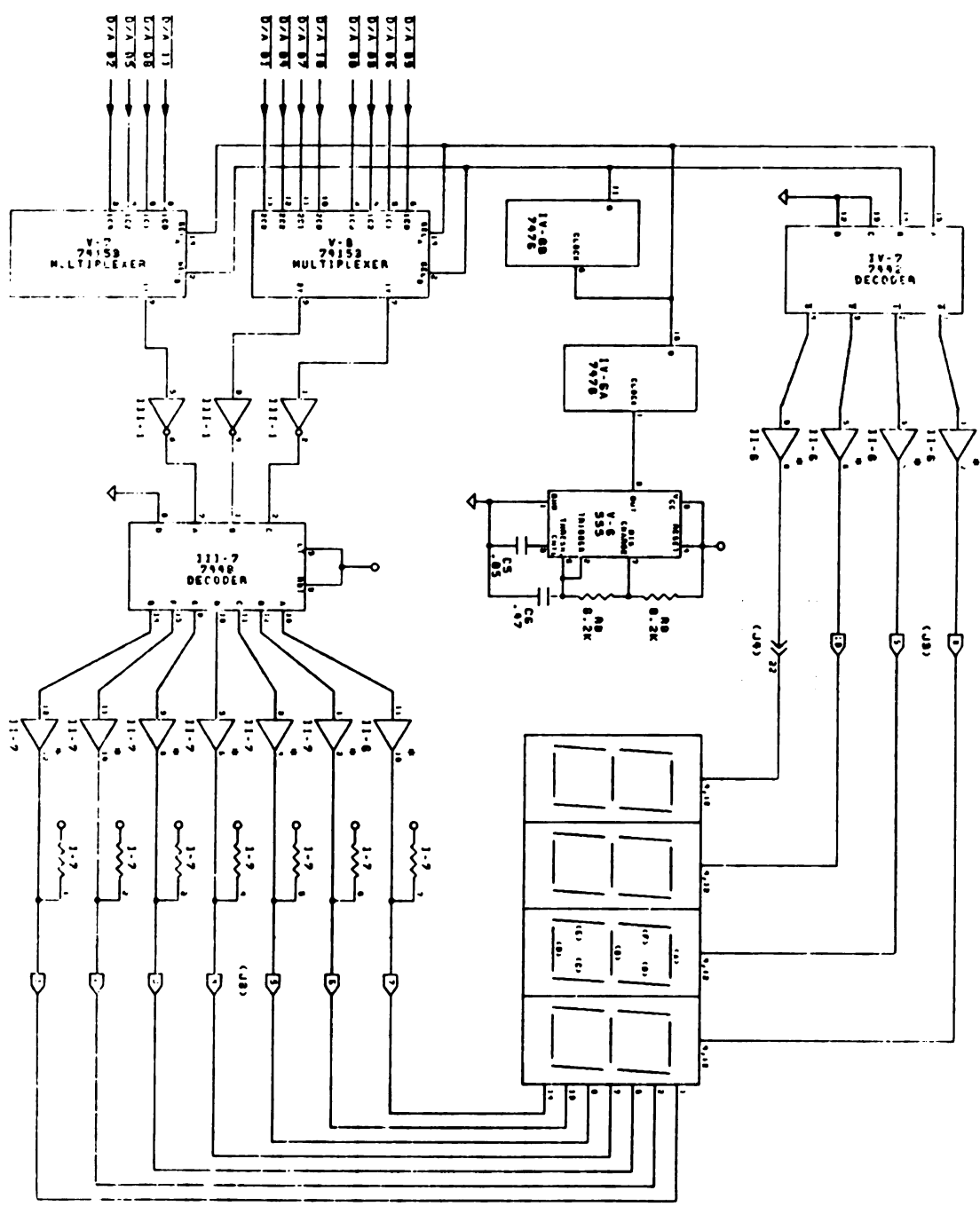


COUNTER DATA SELECT CIRCUIT (MAIN LOGIC BOARD)

Figure A-9. Main Logic Board Thumb Wheel Circuit.



Manual Control Circuits and Counter Enable. Figure A-10.



QUADRUPOLE CONTROL

DIGITAL DISPLAY

Figure A-11. Main Logic Board Digital Display Circuit.

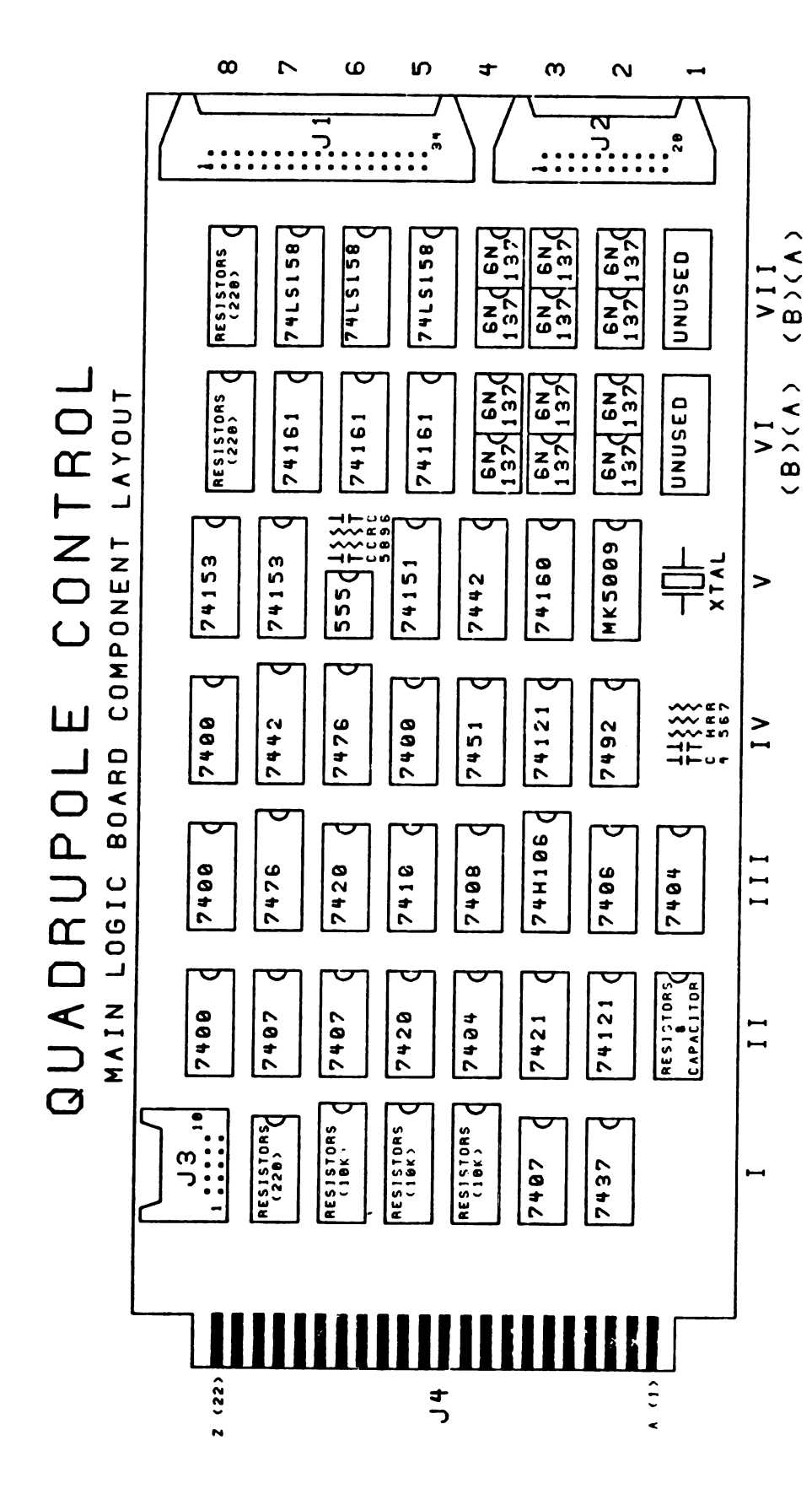


Figure A-12. Main Logic Board Layout.

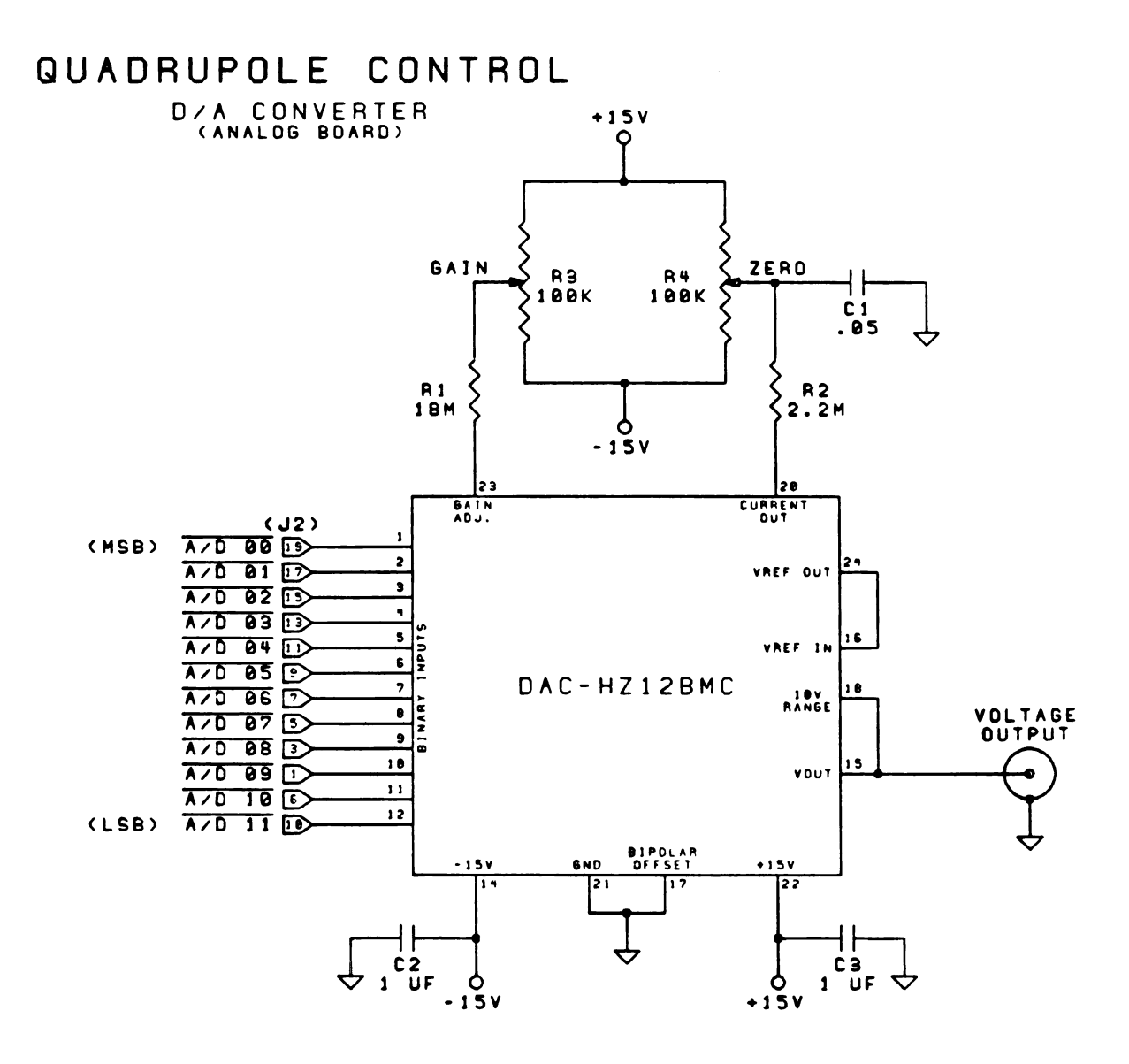


Figure A-13. Analog Circuit.

LIST OF REFERENCES

- B. L. Ulich and E. K. Conklin, Nature 248, 121 (1974).
- P. M. Solomon, K. B. Jeffers, A. A. Pnezias, and R. W. Wilson, Astrophys. J. 168, L107 (1971).
- 3. a) S. L. Miller, J. Amer. Chem. Soc. 77, 235 (1955).
 - b) S. L. Miller and H. C. Urey, Science 130, 245 (1959).
- 4. L. Francesconi and A. Cirulo, Gazz. Chem. Ital. <u>53</u>, 327 (1923).
- 5. F. Hoyle and N. C. Wickramasingle, <u>Lifectoud: The Origin</u> of Life in the Universe (Harper and Row, New York, 1978).
- 6. B. E. Turner, Sci. Amer. 228, no. 3, p. 50 (1973).
- 7. a) E. Herbst and W. Klemperer, Physics Today 29, 32 (1976).
 - b) E. Herbst and W. Klemperer, Astrophysics J. 185, 505 (1973).
- 8. N. W. Reid, Int. J. Mass Spectrom. Ion Phys. 6, 1 (1971).
- 9. H. M. Rosenstock, Int. J. Mass Spectrom. Ion Phys. <u>20</u>, 139 (1976).
- 10. R. W. Ditchburn and F. L. Arnof, Proc. Roy. Soc. <u>A123</u>, 516 (1929).
- 11. A. Terenin and B. Popov, Phys. Z. Sowjetunien 2, 299 (1932).
- 12. W. A. Chupka, "Photoionization and Fragmentation of Polyatomic Molecules", in <u>Chemical Spectroscopy and Photochemistry</u> in the Vacuum Ultraviolet, ec. by C. Sandorfy, P. J. Ausloos and M. B. Robin (D. Reidel, Boston, 1974), pp 431-463.
- 13. A. S. Werner and T. Baer, J. Chem. Phys. 62, 2900 (1975).

- 14. W. A. Chupka, "Ion-Molecule Reactions by Photoionization Techniques", in <u>Ion-Molecule Reactions</u>, vol. 1, ed. by J. L. Franklin (Plenum Press, New York, 1972) pp 33-77.
- 15. A. D. Williamson, Ph.D. Thesis, California Institute of Technology, 1976.
- 16. J. A. R. Samson, Techniques of Vacuum Ultraviolet Spectroscopy (John Wiley and Sons, New York, 1967).
- 17. A. N. Zaidel and E. Ya. Schreider, <u>Vacuum Ultraviolet</u>
 <u>Spectroscopy</u>, trans. by Z. Lermam (Ann Arbor Humphrey
 <u>Science Publishers</u>, Ann Arbor, 1970).
- 18. G. Marr, <u>Photoionization Processes in Gases</u> (Academic Press, New York, 1967).
- 19. Edward J. Darland, Ph.D. Thesis, Michigan State University, 1977.
- 20. J. Berkowitz, "Photoionization Mass Spectrometry and Photoelectron Spectroscopy of High Temperature Vapors", in Advances in High Temperature Chemistry, vol. 3, ed. by L. Eyring (Academic Press, New York, 1971) pp 123-177.
- 21. J. H. D. Eland, <u>Photoelectron Spectroscopy</u> (John Wiley and Sons, New York, 1974).
- 22. J. W. Rabalais, <u>Principles of Ultraviolet Photoelectron</u>
 <u>Spectroscopy</u> (John Wiley and Sons, 1977).
- 23. A. J. C. Nicholson, J. Chem. Phys. 39, 954 (1963).
- 24. G. Herzberg, Molecular Spectra and Molecular Structure, vol. III (Van Nostrand, New York, 1966).
- 25. F. O. Ellison, J. Chem. Phys. 61, 507 (1974).
- 26. J. W. Rabalais, T. P. Debies, J. L. Cerkosky, J. T. J. Huang, and F. O. Ellison, J. Chem. Phys. 61 (1974).
- 27. S. Geltman, Phys. Rev. <u>102</u>, 171 (1956).
- 28. E. P. Wigner, Phys. Rev. 73, 1002 (1948).
- 29. P. C. Killgoar, G. E. Leroi, J. Berkowitz and W. A. Chupka, J. Chem. Phys. 58, 803 (1973).
- 30. V. H. Dibeler and J. A. Walker, Int. J. Mass Spectrom. Ion. Phys. 11, 49 (1973).

- 31. V. H. Dibeler, J. A. Walker and H. M. Rosenstock, J. Res. N.B.S. -A Phys. Chem. 70, 459 (1966).
- 32. P. C. Killgoar, G. E. Leroi, W. A. Chupka, J. Berkowitz, J. Chem. Phys. 59, 1370 (1973).
- 33. M. B. Robin, Higher Excited States of Polyatomic Molecules (Academic Press, New York, 1974).
- 34. U. Fano and J. W. Cooper, Rev. Mod. Phys. 40, 441 (1968).
- 35. A. D. Walsh, J. Phys. Radium 15, 501 (1954).
- 36. E. N. Lassetre, A. Skerbele, M. A. Dillon, and K. J. Ross, J. Chem. Phys. 48, 5066 (1968).
- 37. S. R. La Paglia, J. Chem. Phys. 41 1427 (1964).
- 38. U. Fano, Phys. Rev. 124, 1866 (1961).
- 39. R. S. Berry, J. Chem. Phys. 45, 1228 (1966).
- 40. P. M. Dehmer and W. A. Chupka, J. Chem. Phys. <u>66</u>, 1972 (1977).
- 41. J. H. D. Eland and J. Berkowitz, J. Chem. Phys. $\underline{67}$, 2740 (1977).
- 42. S. Nordholm, J. Chem. Phys. 71, 2313 (1979).
- 43. P. M. Dehmer and W. A. Chupka, J. Chem. Phys. <u>62</u>, 4526 (1975).
- 44. G. R. Cook, P. H. Metzger and M. Ogawa, J. Chem. Phys. 41, 321 (1964).
- 45. R. Botler, J. M. Pechine, and H. M. Rosenstock, Int. J. Mass Spectrom. Ion. Phys. 25, 7 (1977).
- 46. H. W. Jochems, W. Lohr, and H. Baumgätel, Ber. Bunsenges, Physik. Chem. 80, 130 (1976).
- 47. H. M. Rosenstock, M. B. Wallenstein, A. L. Wahrhaflig, and H. Eyring, Proc. Nat. Acad. Sci. U.S. 38, 667 (1952).
- 48. W. Forst, Theory of Unimolecular Reactions (Academic Press, New York, 1973).
- 49. W. A. Chupka, J. Chem. Phys. 54, 1936 (1971).
- 50. W. A. Chupka, J. Chem. Phys. 30, 191 (1959).

- 51. M. Wolfsberg, J. Chem. Phys. 36, 1072 (1962).
- 52. W. A. Chupka, J. Chem. Phys. 48, 2337 (1968).
- 53. W. A. Chupka and J. Berkowitz, J. Chem. Phys. <u>47</u>, 2921 (1967).
- 54. R. Stockbauer, J. Chem. Phys. 58, 3800 (1973).
- 55. D. W. Turner, C. Baker, A. D. Baker, and C. R. Brundle, <u>Molecular Photoelectron Spectroscopy</u> (Wiley-Interscience, New York, 1970).
- 56. J. F. Redina and R. E. Grojean, Appl. Spectrosc. <u>25</u>, 24 (1971).
- 57. E. N. Lassetre, A. Skerbele, M. A. Dillon, and K. J. Ross, J. Chem. Phys. 48, 5066 (1968).
- 58. E. J. Darland, D. M. Ridier, C. G. Enke, and G. E. Leroi, Int. J. Mass Spectrom. Ion Phys. in press (1980).
- 59. E. J. Darland, C. G. Enke, and G. E. Leroi, Anal. Chem. 61, in press (1980).
- 60. E. J. Darland, J. E. Hornshuh, C. G. Enke, and G. E. Leroi, Anal. Chem. 51, 245 (1979).
- 61. Chemcomgraph, computer graphics facility of MSU Chemistry Department.
- 62. G. A. Gray, J. Amer. Chem. Soc. 90, 6002 (1968).
- 63. K. Watanabe, T. Nakayama, J. Motti, J. Quant. Spec. Rad. Trans. 2, 369 (1962).
- 64. A.J.C. Nicholson, J. Chem. Phys. 43, 1171 (1965).
- 65. V. H. Dibeler and K. S. Liston, J. Chem. Phys. <u>48</u>, 4765 (1968).
- 66. D. C. Frost, F. G. Herring, C. A. McDowell, and I. A. Stenhouse, Chem. Phys. Lett. 4, 533 (1970).
- 67. R. F. Lake and H. Thompson, Proc. Roy. Soc. Lon. A. 317, 187 (1979).
- 68. M. N. Ashfold, J. P. Simmons, J. Chem. S. Far. Trans. II 74, 1263 (1978).
- 69. T. K. Ha, J. Mol. Structure, 11, 185 (1972).

- 70. J. L. Franklin, Y. Wada, P. Natalis, and P. M. Hierl, Phys. Chem. 70, 2353 (1966).
- 71. F. W. McLafferty, Anal. Chem. 34, 26 (1962).
- 72. C. Fridth, J. Chem. Soc. Far. Trans. II 74, 2193 (1978).
- 73. P. Houchman, H. Wang, W. S. Felps, S. Foster, and S. P. McGlyn, "On the Assignment of Molecular Rydberg Series", in Chemical Spectroscopy and Photochemistry in the Vacuum Ultraviolet, ed. by C. Sandorfy, P. J. Ausloos, and M. B. Robin (D. Reidel, Boston, 1974) pp 385-393.
- 74. J. L. Dye and V. A. Nicely, Chem. Ed. 48, 443 (1971).
- 75. W. A. Chupka, private communication.
- 76. J. A. Cutler, J. Chem. Phys. 16, 136 (1948).
- 77. R. S. Stradling, A. G. Loudon, J. Chem. Soc. Far. Trans. II 73, 623 (1977).
- 78. C. Fridth and L. Asbrink, J. Elect. Spec. and Rel. Phen. 7, 119 (1975).
- 79. L. Asbrink, C. Fridth, and E. Lindholm, Chem. Phys. <u>27</u>, 159 (1978).
- 80. a) L. Asbrink, C. Fridth, and E. Lindholm, Chem. Phys. Lett. <u>52</u>, 63 (1977).
 - b) L. Asbrink, C. Fridth, and E. Lindholm, "HAM-A-Semi-emperical MO Theory", in Chemical Spectroscopy in the Vacuum Ultraviolet, ed. by C. Sandory, P. J. Ausloos, and M. B. Robin (D. Reidel, Boston, 1974), pp 247-251.
- 81. R. H. Stanley, J. E. Kleckner, J. L. Beuchamp, J. Amer. Chem. Soc. <u>98</u>, 208 (1976).
- 82. C. E. More, "Atomic Energy Levels", Nat. Bur. Std. circ. 467, vol 1.
- 83. W. A. Chupka and M. E. Russell, J. Chem. Phys. <u>49</u>, 5426 (1968).
- 84. P. M. Guyon and J. Berkowitz, J. Chem. Phys. <u>54</u>, 1814 (1971).
- 85. R. D. Hudson and V. L. Carter, J. Opt. Soc. Am. 58, 227, (1968).
- 86. L. Asbrink, Chem. Phys. Lett. <u>7</u> 549 (1970).

- 87. R. N. Dixon, G. Daxbury, M. Horani, and J. Rostas, Mol. Phys. 22, 977 (1971).
- 88. T. Shemanouchi, <u>Tables of Molecular Vibrational</u>
 <u>Frequencies</u>, <u>consolidated Vol. I, Nat. Stand. Ref. Data</u>
 <u>Serv. 39, 84 (1972).</u>
- 89. C. F. Carter, M. R. Levy, and R. Grice, Faraday Discuss. Chem. Soc. 55, 357 (1973).
- 90. D. A. McQuarrie, Statistical Mechanics (Harper and Row, New York, 1976).
- 91. H. M. Rosenstock, K. Draxl, B. W. Steiner and J. T. Herron, J. Phys. and Chem. Ref. Data 6, supplement 1 (1977).
- 92. G. Herzberg, Can. J. Phys. 39, 1511 (1961).
- 93. W. A. Chupka and C. Lifshitz, J. Chem. Phys. <u>48</u>, 1109 (1968).
- 94. G. Herzberg and J. Shoosmith, Can. J. Phys. 34, 523 (1956).
- 95. F. A. Elder, C. Gaese, B. Steiner, and M. Ingram, J. Chem. Phys. 36, 3292 (1962).
- 96. F. W. McLafferty, <u>Interpretation of Mass Spectra</u> (W. A. Benjamin, Reading Mass., 1973).
- 97. J. March, Advanced Organic Chemistry: Reaction, Mechanisms, and Structure (McGraw-Hill, New York, 1977).
- 98. M. E. Jacox, Chem. Phys. 43, 157 (1979).
- 99. A. C. Hopkenson, M. H. Lien, K. Yates, P. C. Mazey, and I. C. Csizmadea, J. Chem. Phys. 67, 517 (1977).
- 100. J. F. Wolf, R. H. Stanley, I. Koppel, M. Taagepera, R. T. McIver, J. L. Beauchamp, and R. W. Taft, J. Amer. Chem. Soc. 99, 5417 (1977).
- 101. D. H. Aue, H. M. Webb, and M. T. Bowers, J. Amer. Chem. Soc. 98, 311 (1976).
- 102. L. Anderws, Appl. Spectrosc. 33, 199 (1979).
- 103. T. Baer, G. D. Willett, D. Smith, and J. S. Phillips, J. Chem. Phys. <u>70</u>, 4076 (1979).

